Diagnostics of Flux Emergence on the Sun

Mark Cheung
Staff Physicist @ Lockheed Martin Solar & Astrophysics Laboratory
Visiting Associate Professor @ National Astronomical Observatory of Japan

Observation
+ Experiment

Theory

Scientific
Computation

Outline

(1) Magnetic Field Diagnostics

(2) Thermal Diagnostics

(3) Data-driven Modeling (Again)

Magnetic Field Diagnostics of Emerging Flux

Extremely large volume of papers studying photospheric magnetic observations of flux emergence.

Ground-based instruments: Leka et al. (1996); Strous et al. (1996); Lites, Skumanich & Martinez Pillet (1998); Strous & Zwaan (1999); De Pontieu (2002); **Kubo, Shimizu & Lites (2003)**; Watanabe et al. (2008, 2011); Guglielmino et al (2010); Yurchyshyn et al. (2010), Rutten et al. (2013)

Balloons: Flare Genesis Experiment Bernasconi et al. (2002); **Pariat et al (2004)**

SUNRISE Guglielmino et al. (2012)

MDI Many many papers

Hinode **Centeno et al. (2007)**; Cheung et al. (2008); Okamoto et al. (2008); Magara (2008); Gonzalez & Bello Rubio (2009); Otsuji et al. (2009, 2011); Ishikawa, Tsuneta & Jurčák (2010), Shimizu, Ichimoto & Suematsu (2012)

SDO/HMI Centeno et al (2012): Liu & Schuck (2012); Toriumi, Hayashi & Yokoyama (2012, 2014); Tarr & Longcope (2012); Cheung & DeRosa (2012), Cheung et al. (2015)

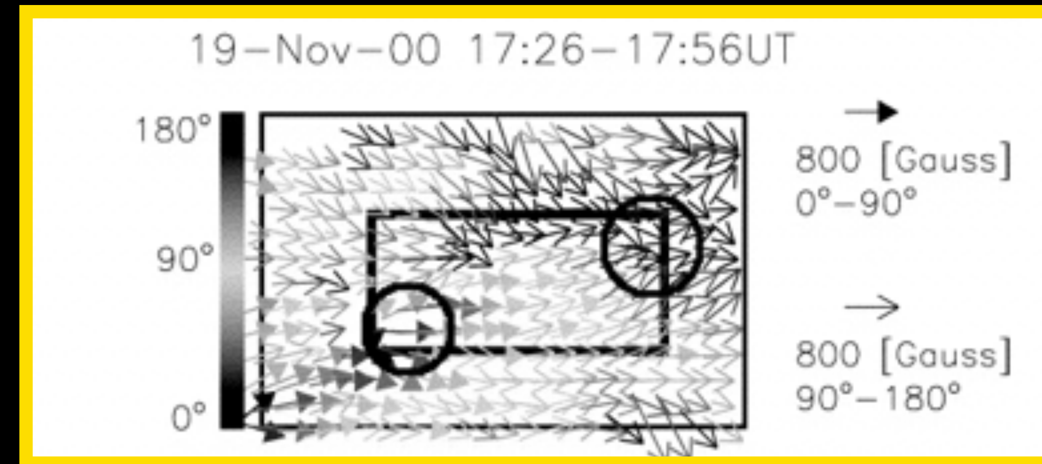

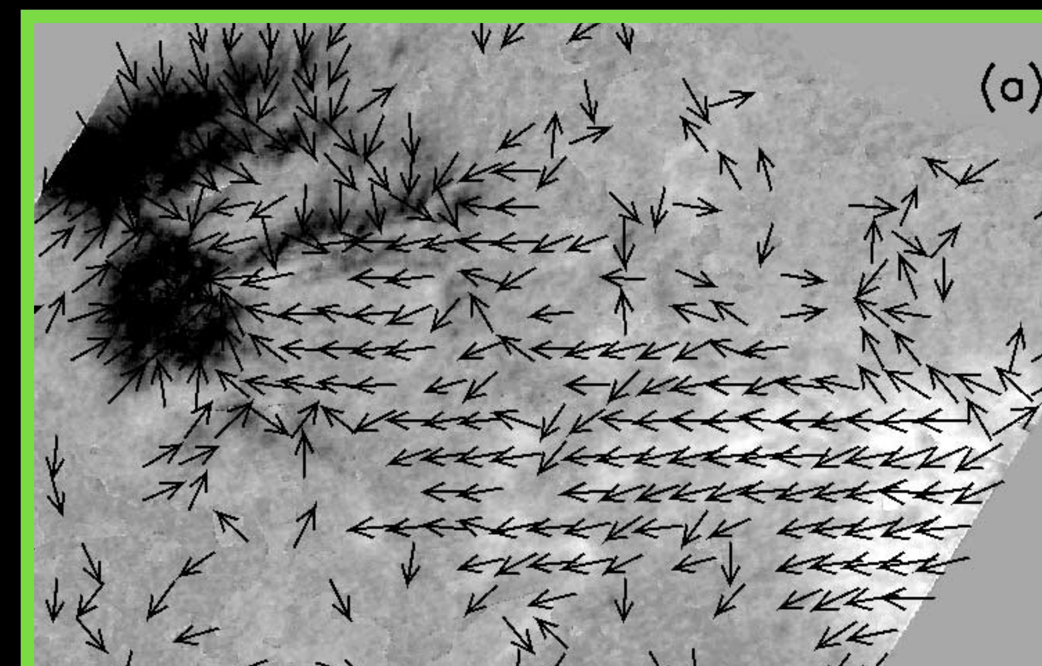

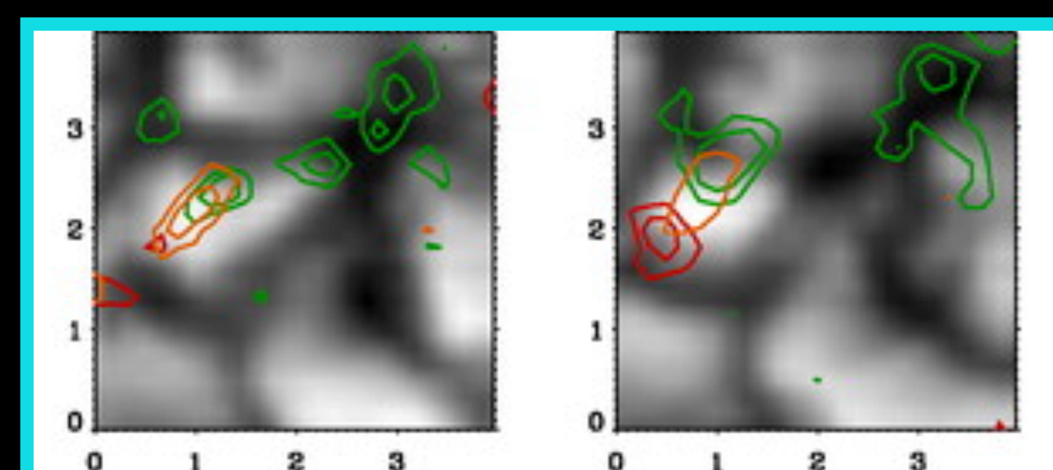

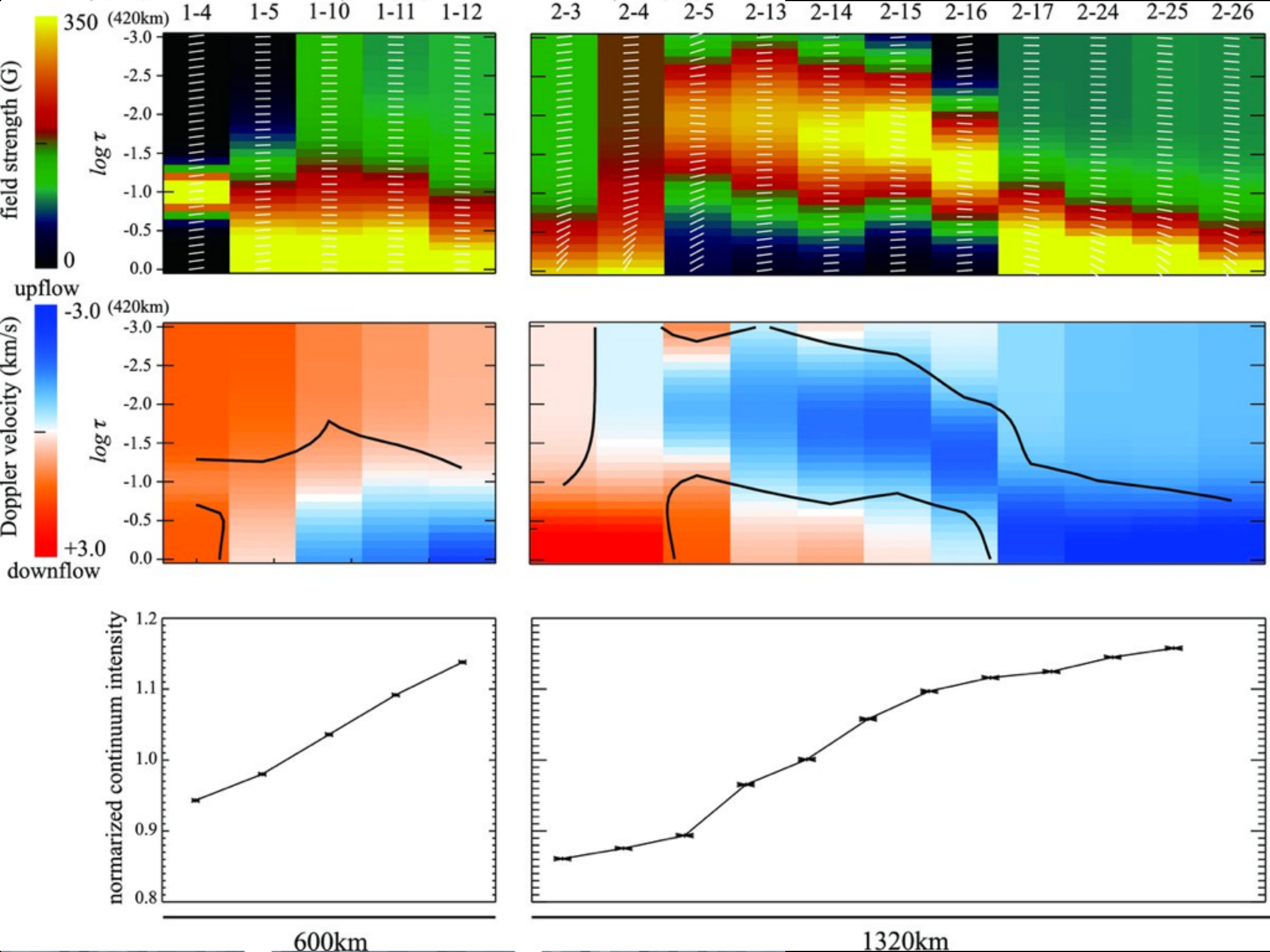

field strength (G)
350
0
(420km)
1-4
1-5
1-10
1-11
1-12
2-3
2-4
2-5
2-13
2-14
2-15
2-16
2-17
2-24
2-25
2-26
log τ
-3.0
-2.5
-2.0
-1.5
-1.0
-0.5
0.0
upflow
Doppler velocity (km/s)
-3.0
+3.0
downflow
normarized continuum intensity
1.2
1.1
1.0
0.9
0.8
600km
1320km

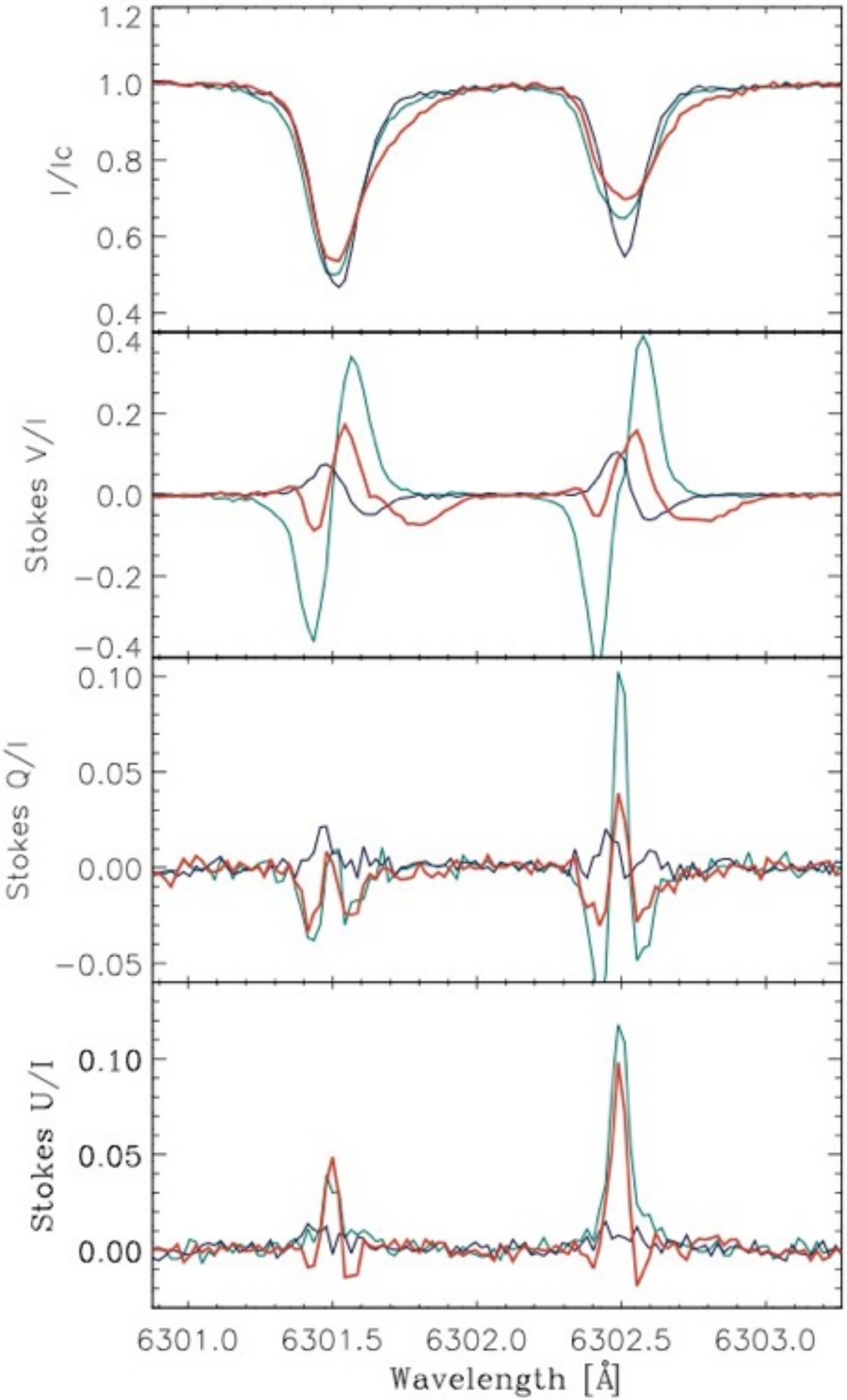

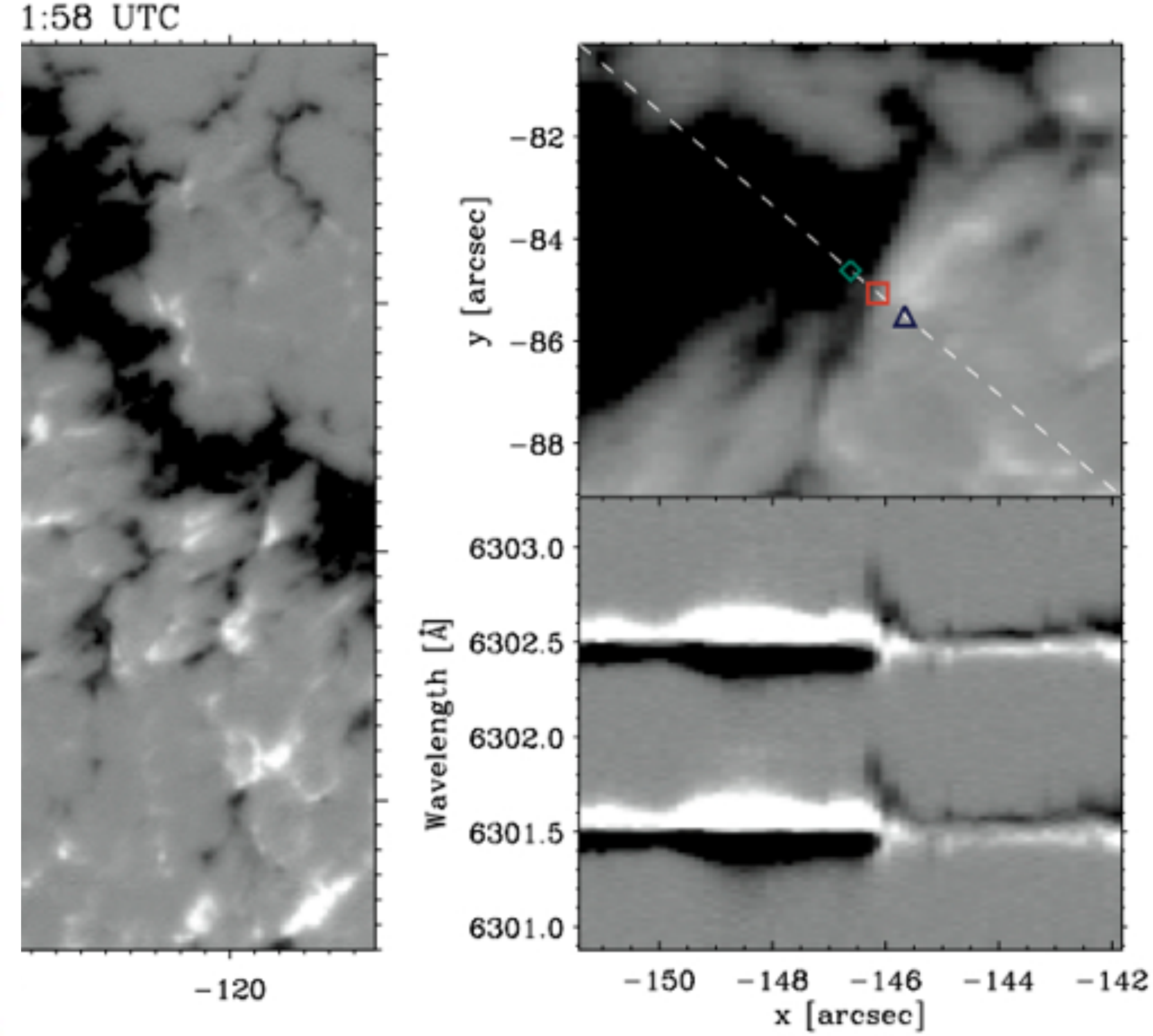

Supersonic downflows in a flux cancellation site (Cheung et al. 2008) from Hinode/SP. Perhaps a signature of reconnection down flows.

Flux emergence in the photosphere

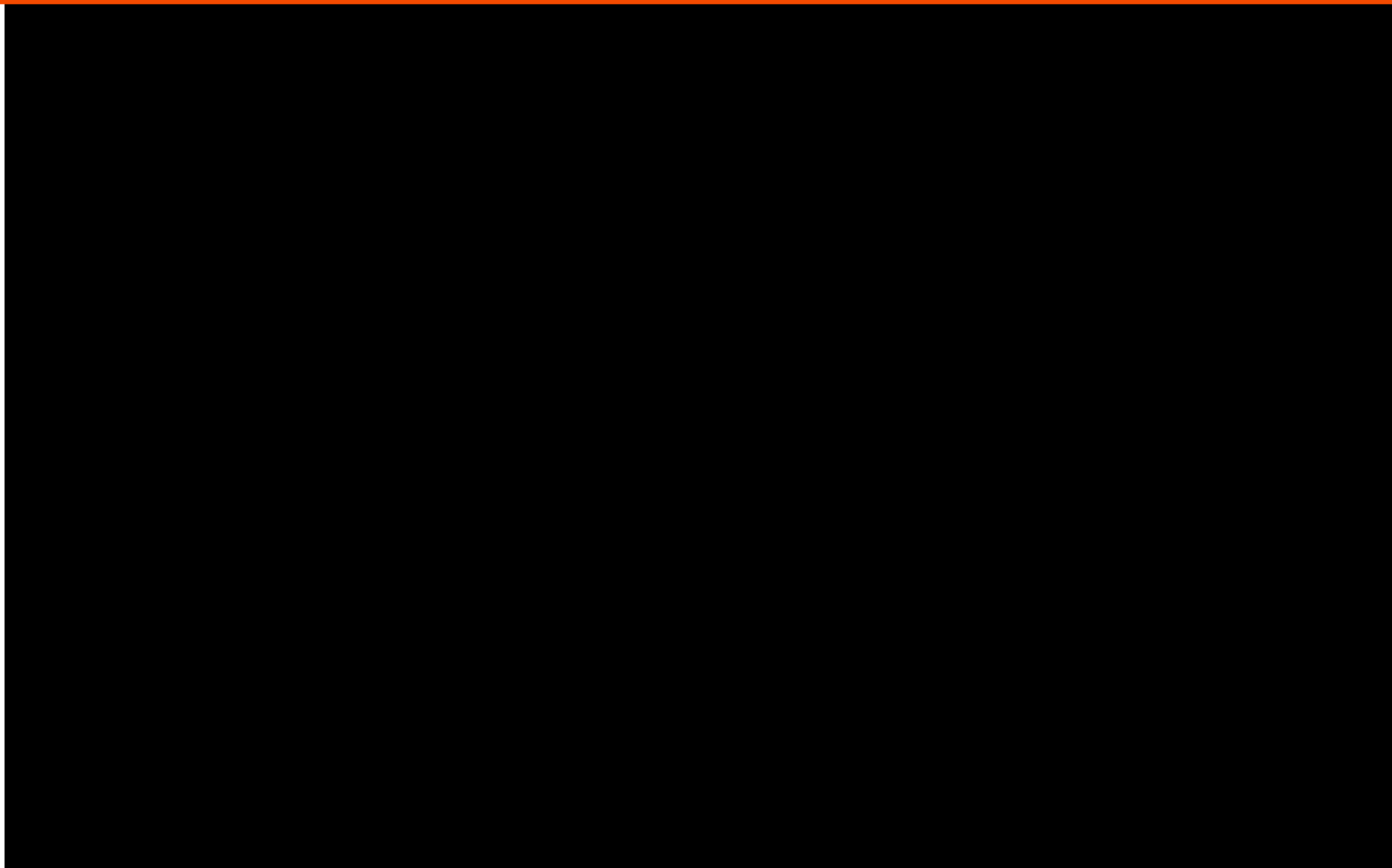

- Stokes I: dark Doppler signatures of small-scale magnetic loops.
- Stokes Q & U: elongated features in the body of the loop.
- Stokes V: most of the signal is concentrated at the footprints of the loops.

Slide credit: J. De La Cruz Rodriguez

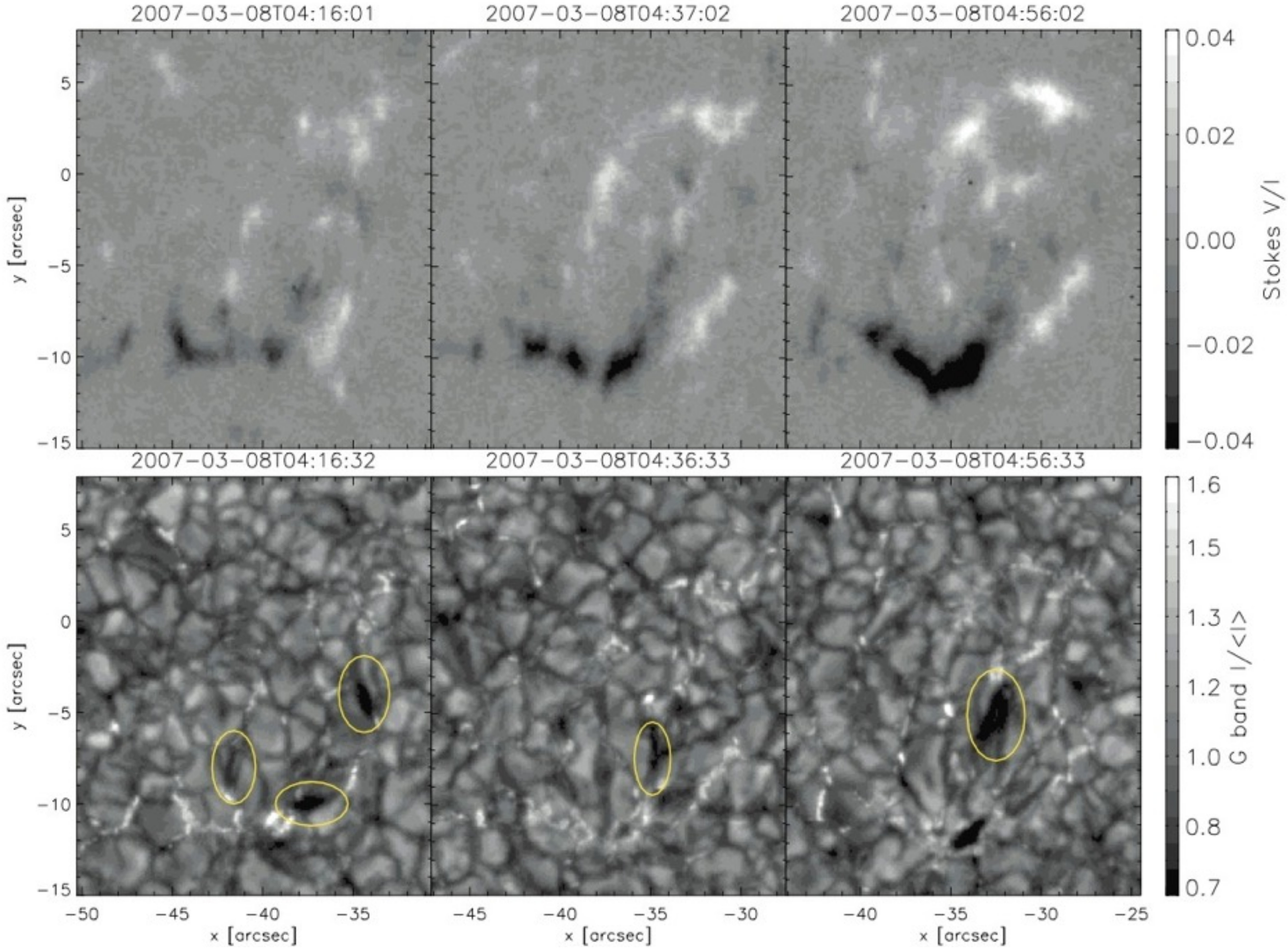

From Cheung et al. (2008): SOT/NFI observations of dark lanes in emerging flux regions. See also Strous & Zwaan (1999).

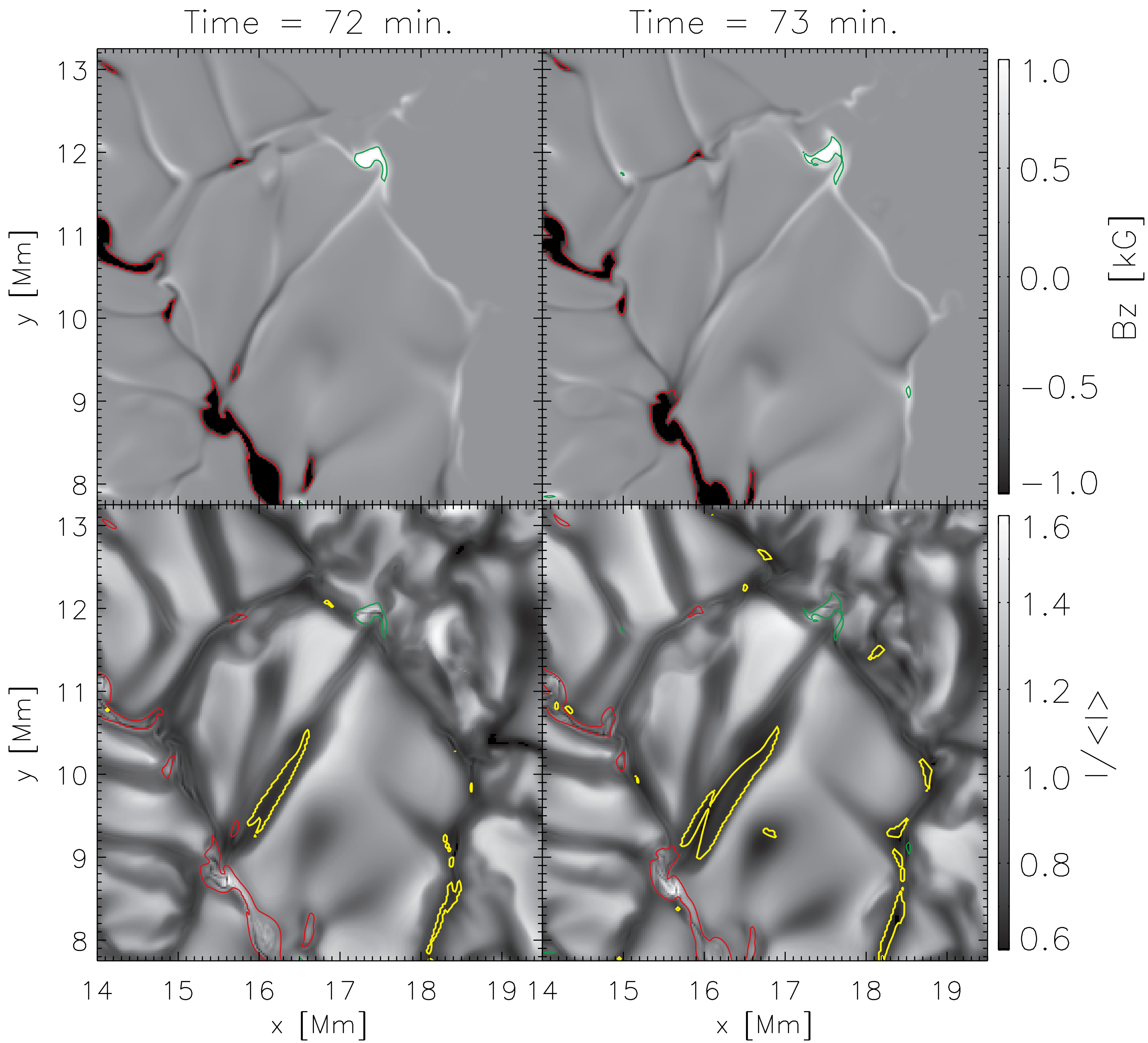

From Cheung et al. (2008): Radiative MHD simulation of emerging flux reproduces dark lanes. Basically, upflow regions with low entropy.

Magnetic bubbles in the photosphere

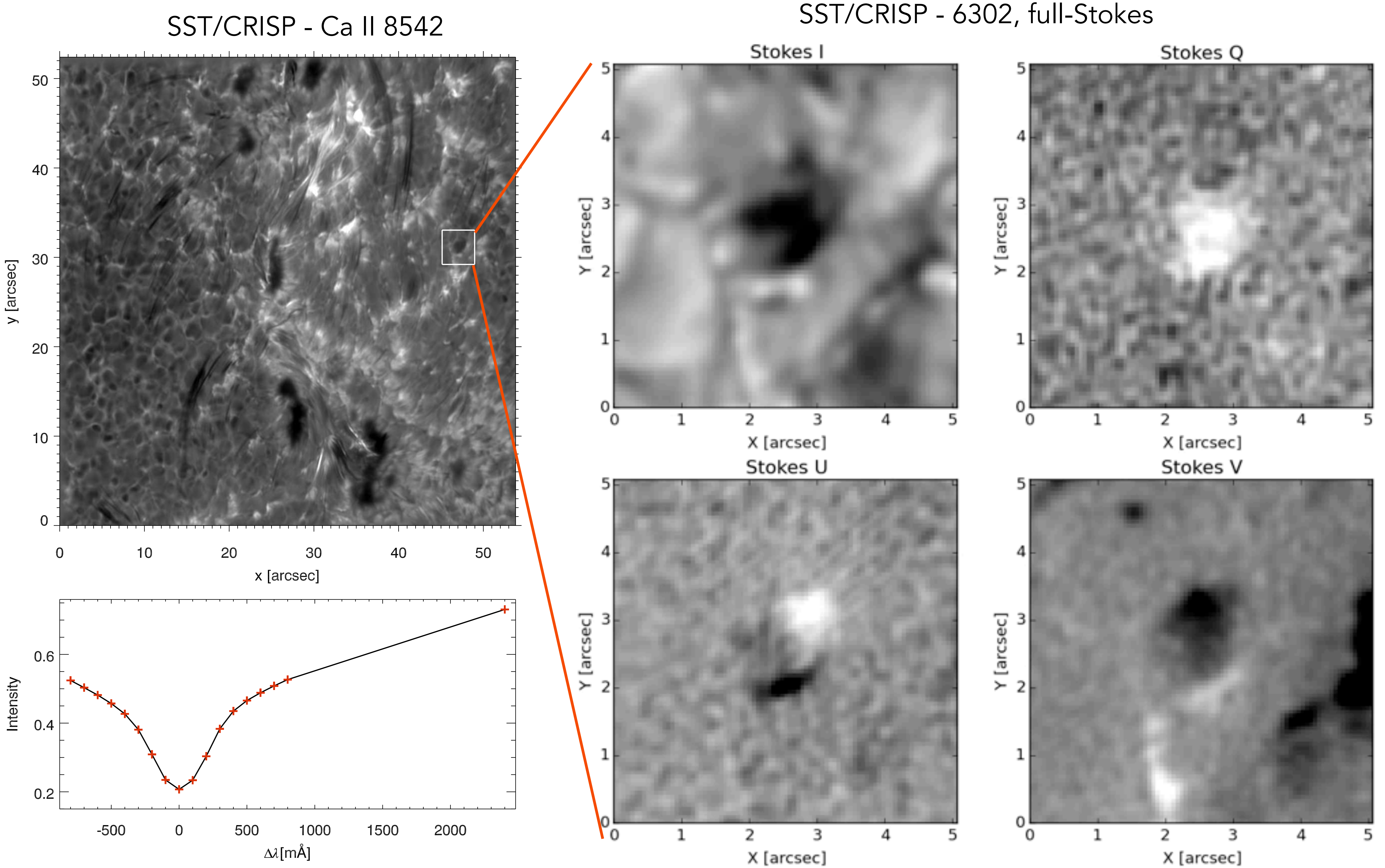

Slide credit: J. De La Cruz Rodriguez

Ortiz et al. (2014)

Magnetic bubbles in the chromosphere

SST/CRISP - 8542

Ortiz et al. (2014); de la Cruz Rodríguez et al. (2015)

From Ortiz et al. (2014):

- The emergence is not visible at line center in Ca II 8542, during our series.
- Canopy of fibrils above the emerging flux in the chromosphere.
- Line positions along the wing show similar dark features as in the Fe I lines.
- Observed delay in 8542 relative to Fe I 6302.
- No signal in Stokes Q & U, very weak Stokes V signal.

Slide credit: J. De La Cruz Rodriguez

De la Cruz Rodriguez et al. (2015): non-LTE Stokes inversion of SST Ca II 8542 Å observations of an emerging magnetic bubble.

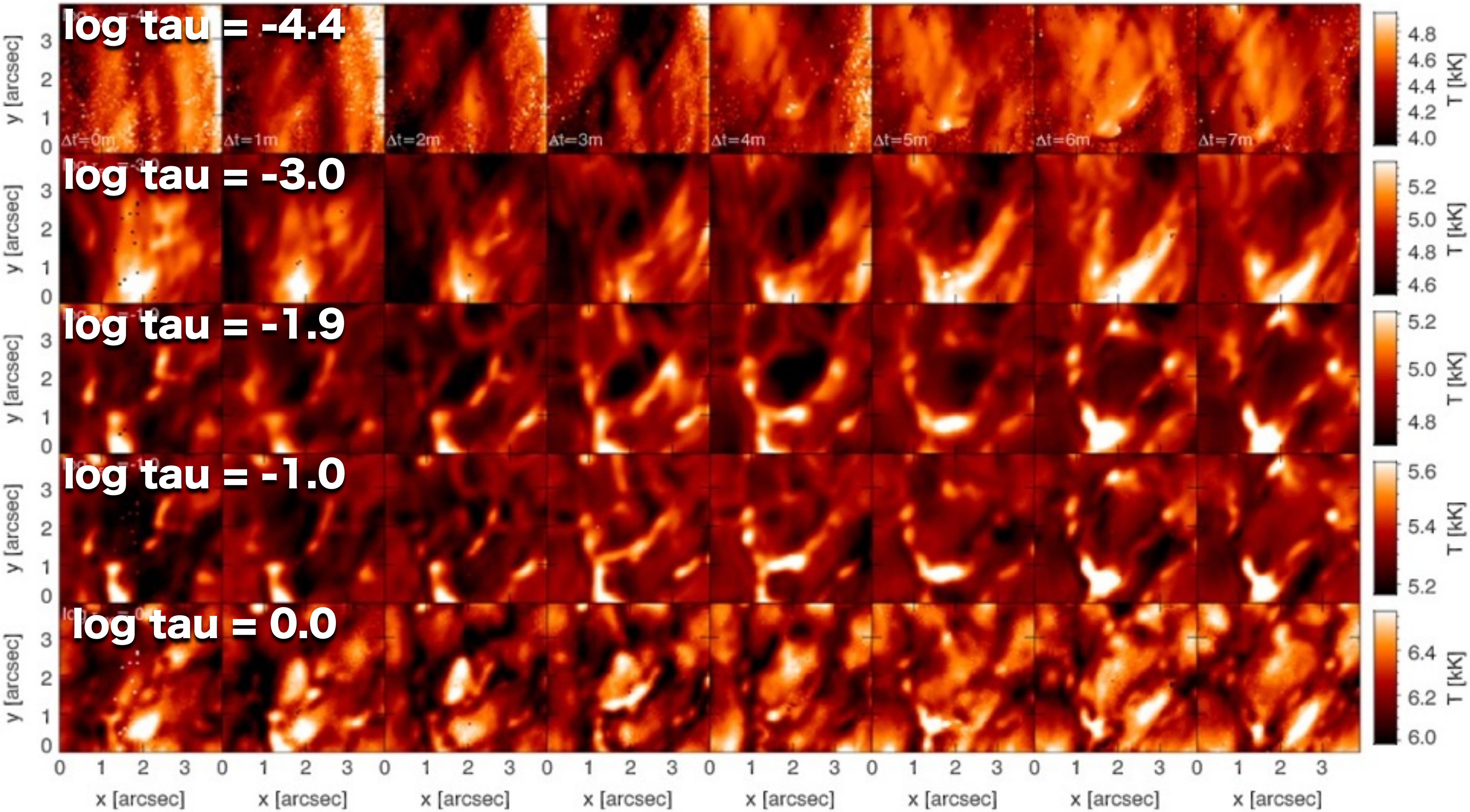

Figure 2. Temporal evolution of the temperature inferred with a non-LTE inversion. From left to right, the panels show consecutive time steps from our time series. From bottom to top, the panels illustrate the inferred temperature at iso-log τ_{500} surfaces in the model. $\Delta t = 0$ corresponds to 10:07:16 UT.

Above: Sequence of temperature maps at 1 min cadence

Below: Sequence of Doppler velocity maps at 1 min cadence

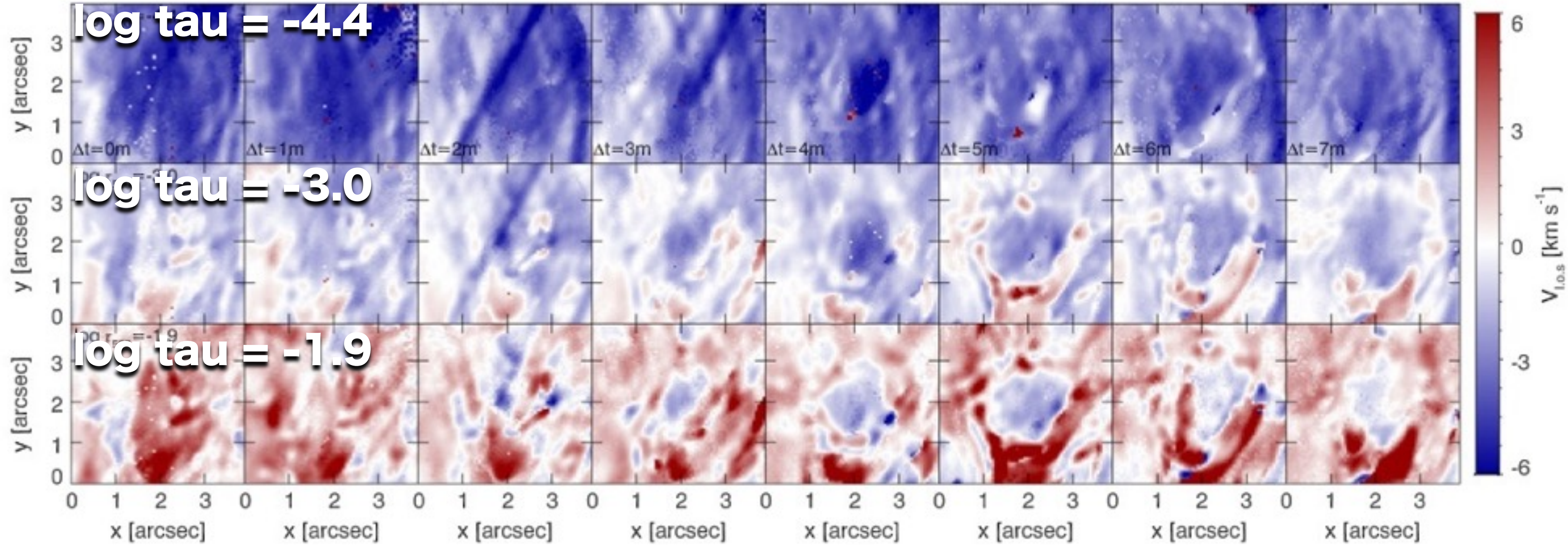

Figure 3. Temporal evolution of the line-of-sight velocity inferred with a non-LTE inversion. From left to right, the panels show consecutive time steps from our time series. From bottom to top, the panels illustrate the inferred temperature at iso-log τ_{500} surfaces in the model. $\Delta t = 0$ corresponds to 10:07:16 UT.

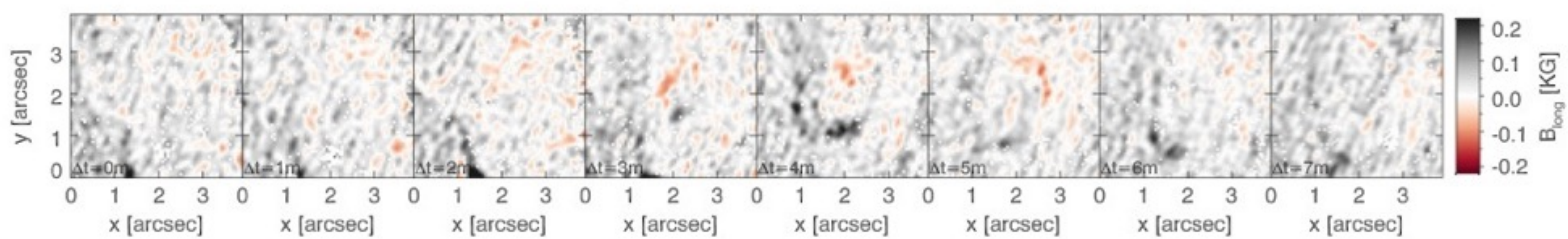

Figure 4. Temporal evolution of the longitudinal component of the magnetic field inferred with a non-LTE inversion. From left to right, the panels show consecutive time steps from our time series. $\Delta t = 0$ corresponds to 10:07:16 UT.

Above: Sequence of Bz maps at 1 min cadence

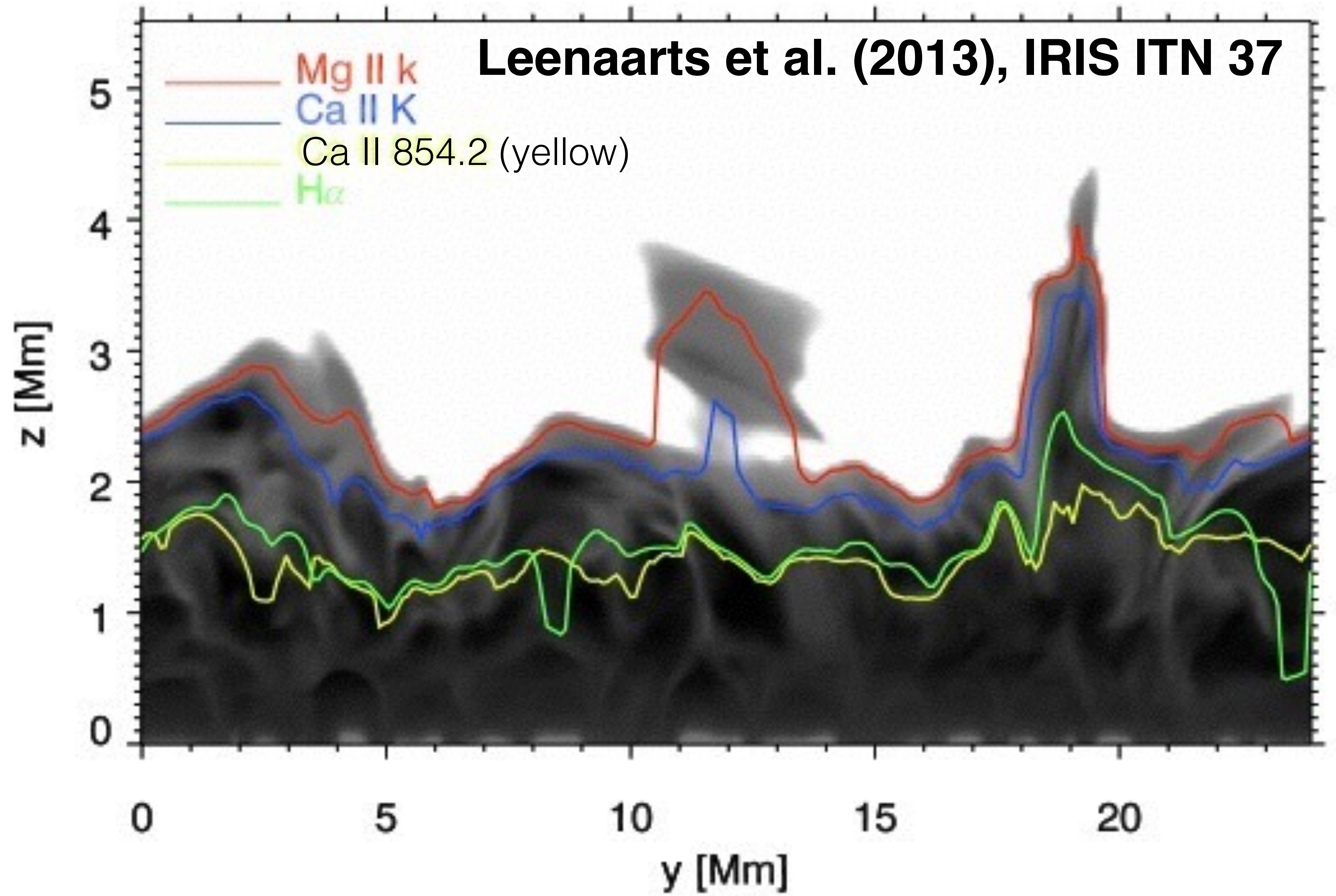

Figure 1. Differences between $\tau = 1$ heights of Mg II k, Ca II K, Ca II 854.2 nm, and Hα in an yz-slice of the 3D model atmosphere. The image displays the temperature, clipped at 20 kK, with curves of the maximum $\tau = 1$ height of the various lines overplotted.

Radiative MHD simulation of AR formation* (M. Rempel)

*work done for NASA's Heliophysics Grand Challenges Research project (LMSAL/NCAR/SAO/BAERI/U Oslo)

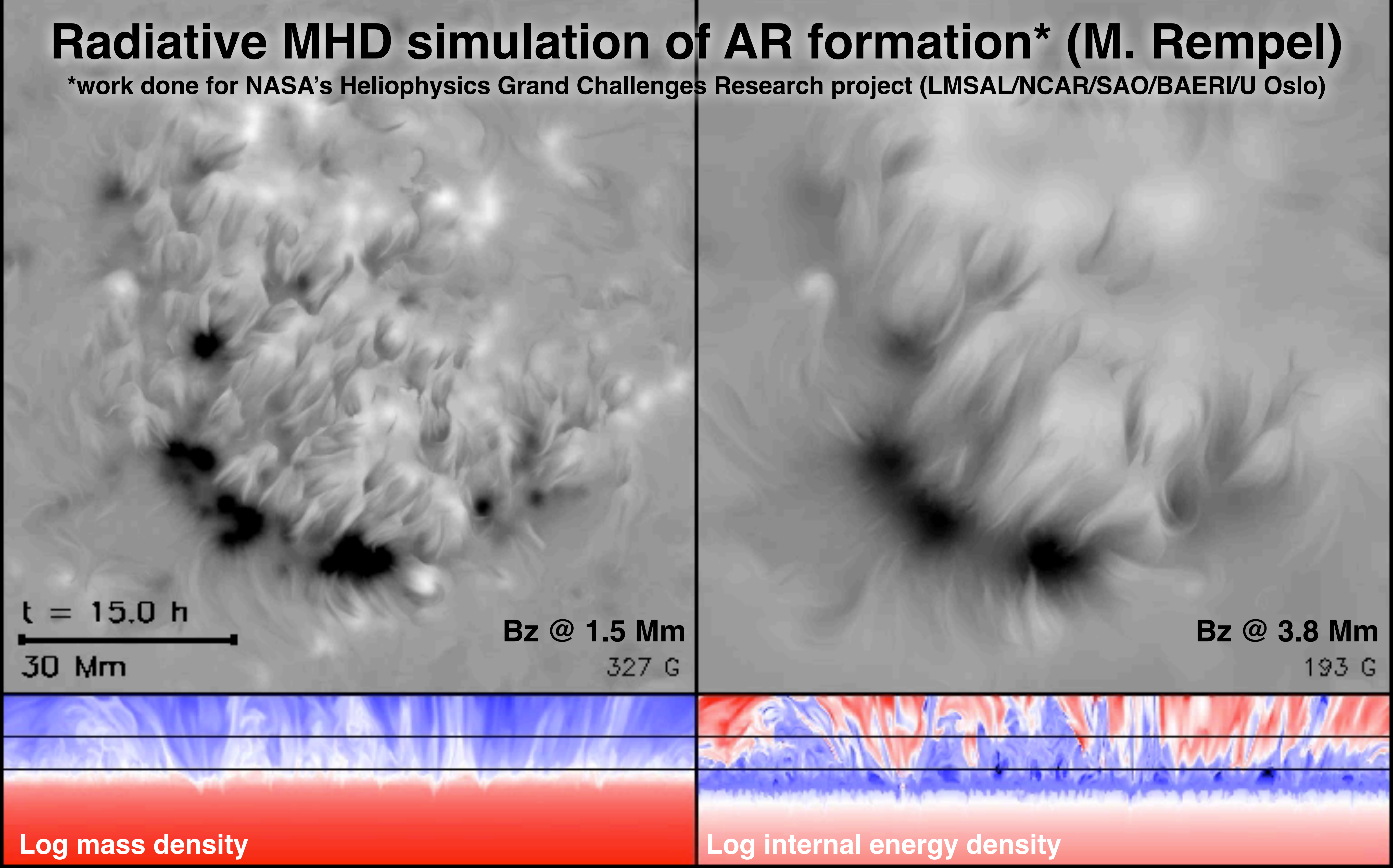

Integral Field Spectropolarimetry (e.g. Solar-C, DKIST)

It would be an amazing achievement to map the chromospheric field to see reconnection in action.

IRIS raster scan of an EFR: Mg II k and Mg II triplet

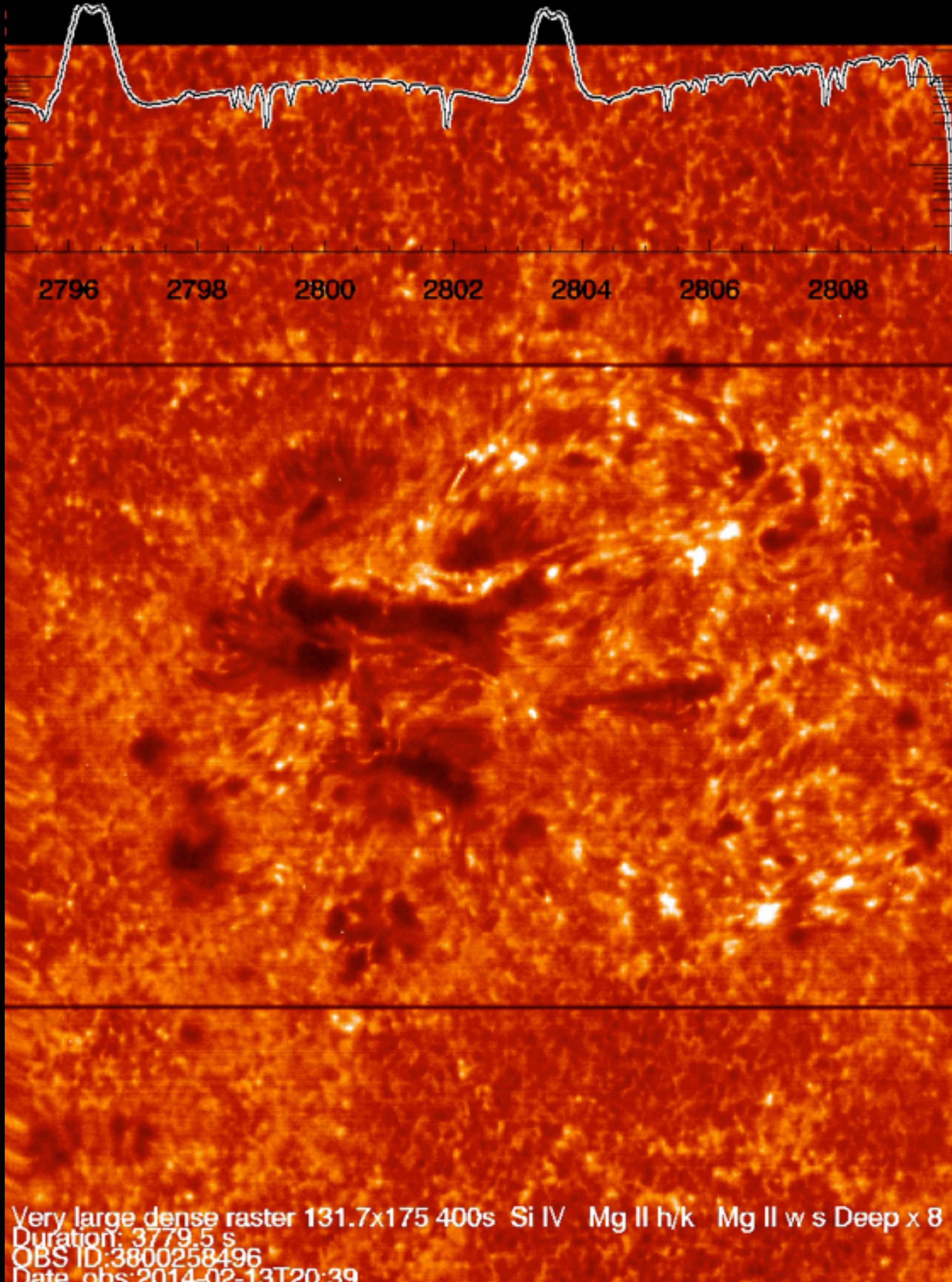

Scanning from the wing to the k3 (core), one sees the transition from reversed granulation to arch filaments / fibrils.

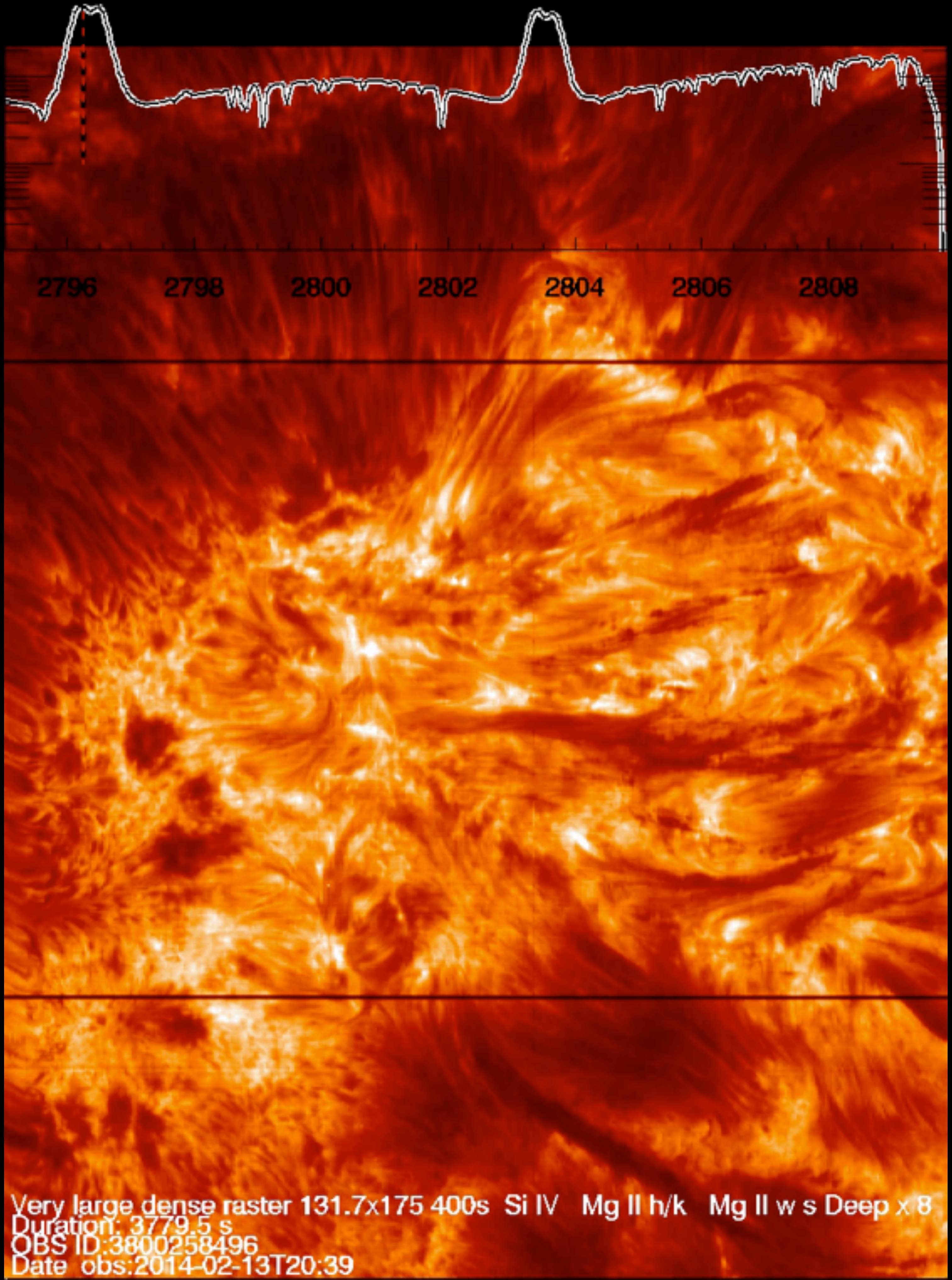

IRIS raster scan of an EFR: Mg II k and Mg II triplet

Scanning from the wing to the k3 (core), one sees the transition from reversed granulation to arch filaments / fibrils.

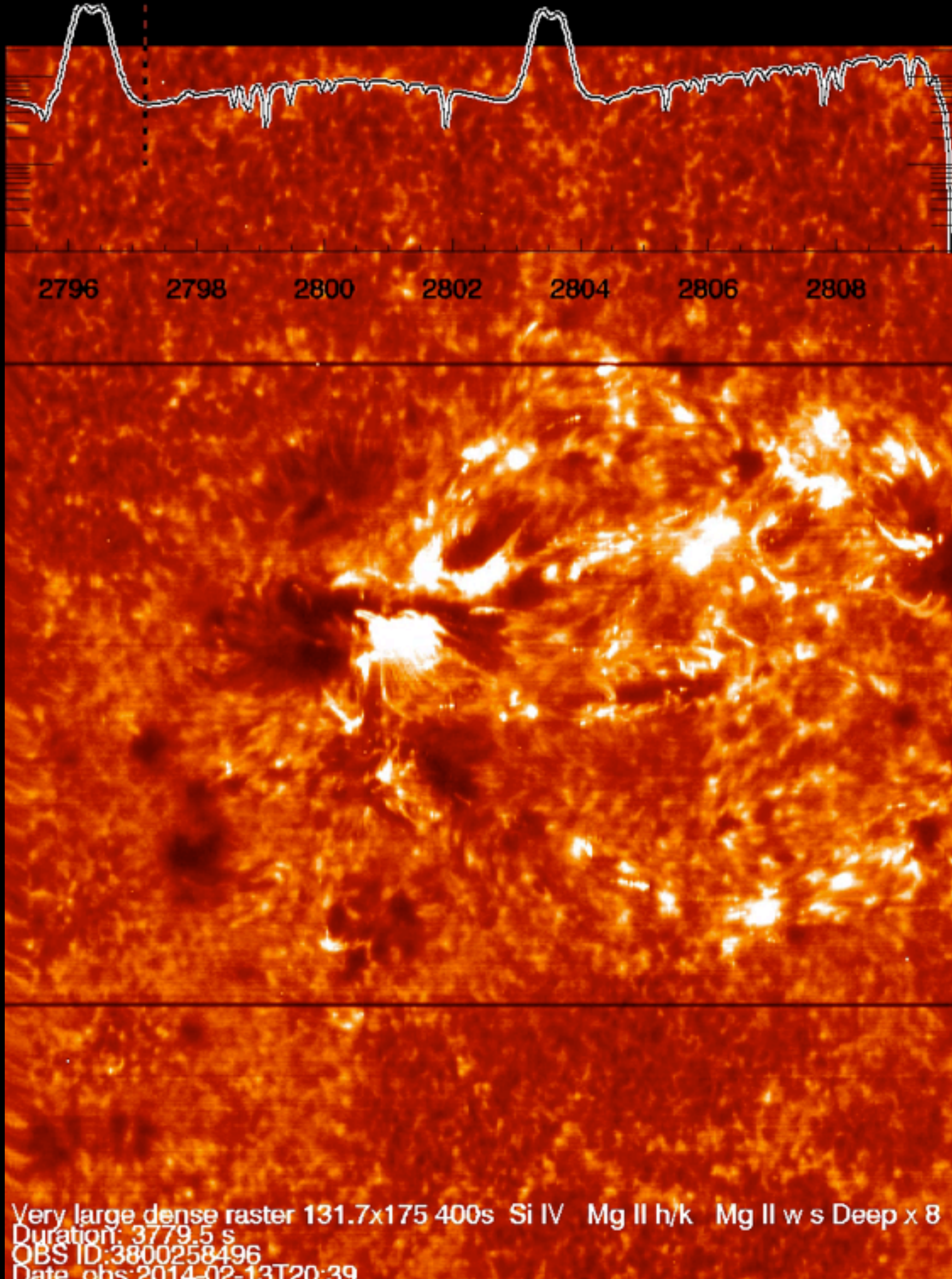

IRIS raster scan of an EFR: Mg II k and Mg II triplet

Scanning from the wing to the k3 (core), one sees the transition from reversed granulation to arch filaments / fibrils.

Scanning to the Mg II triplet, one sees different structure in the chromosphere (seemingly lower lying loops).

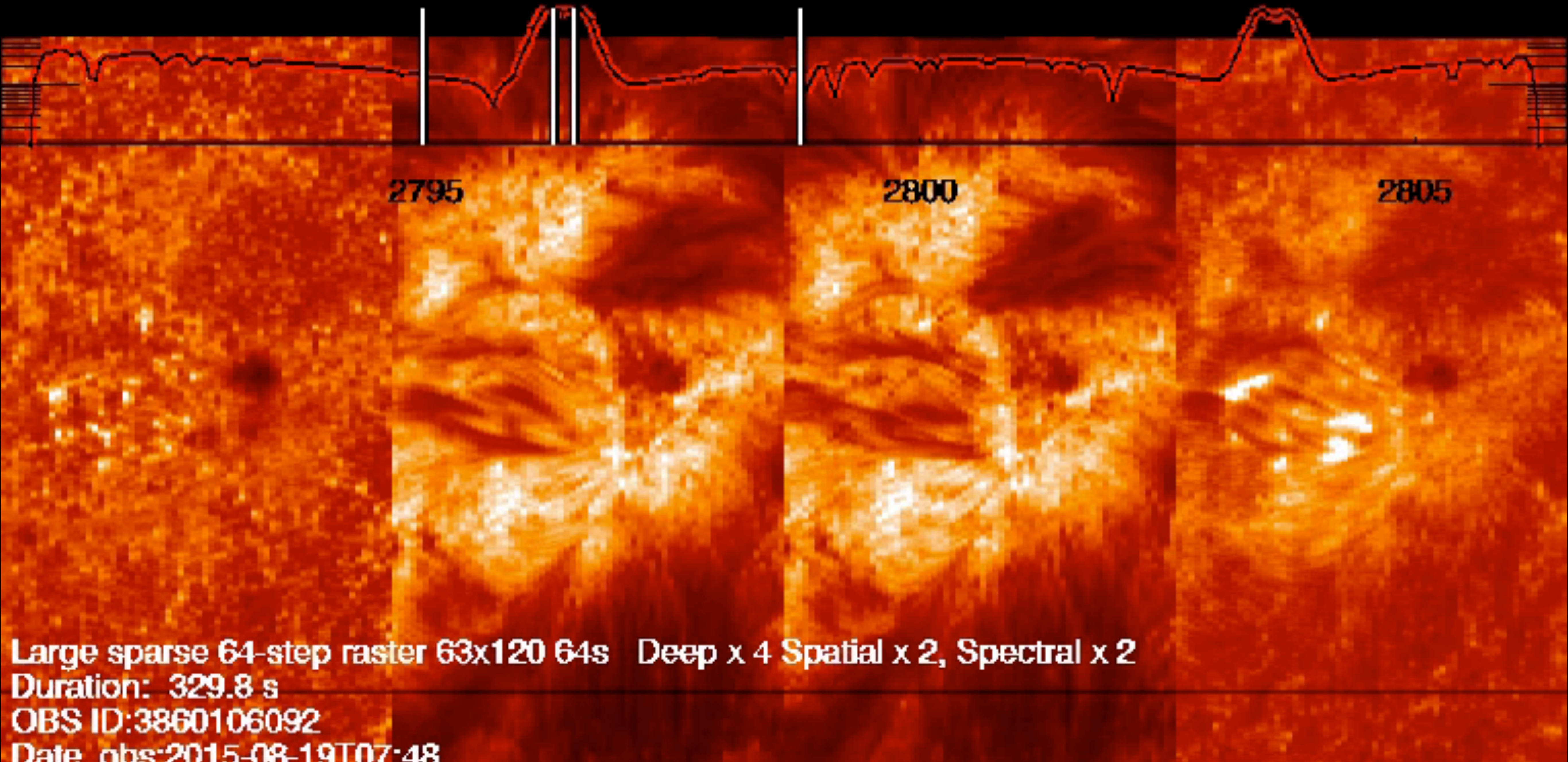

Blue wing Near k2v Near k2r Mg II triplet

IRIS Mg II rasters of an EFR @ 330s cadence
Mg II triplet lines are a diagnostics for low chromospheric heating
(Pereira et al. 2015)

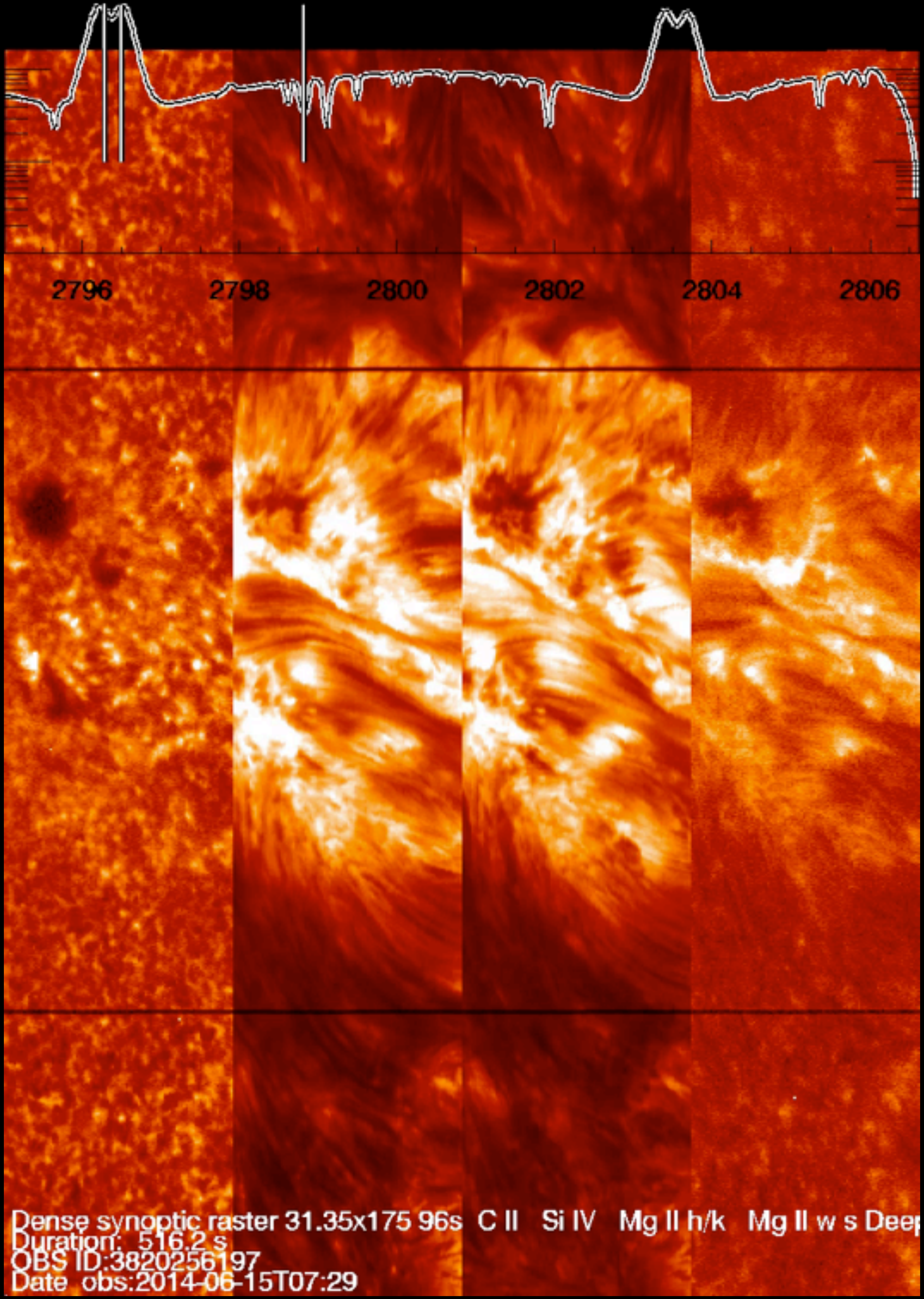

Wouldn't it be fantastic to put magnetic field vectors on these images?

Thermal Diagnostics

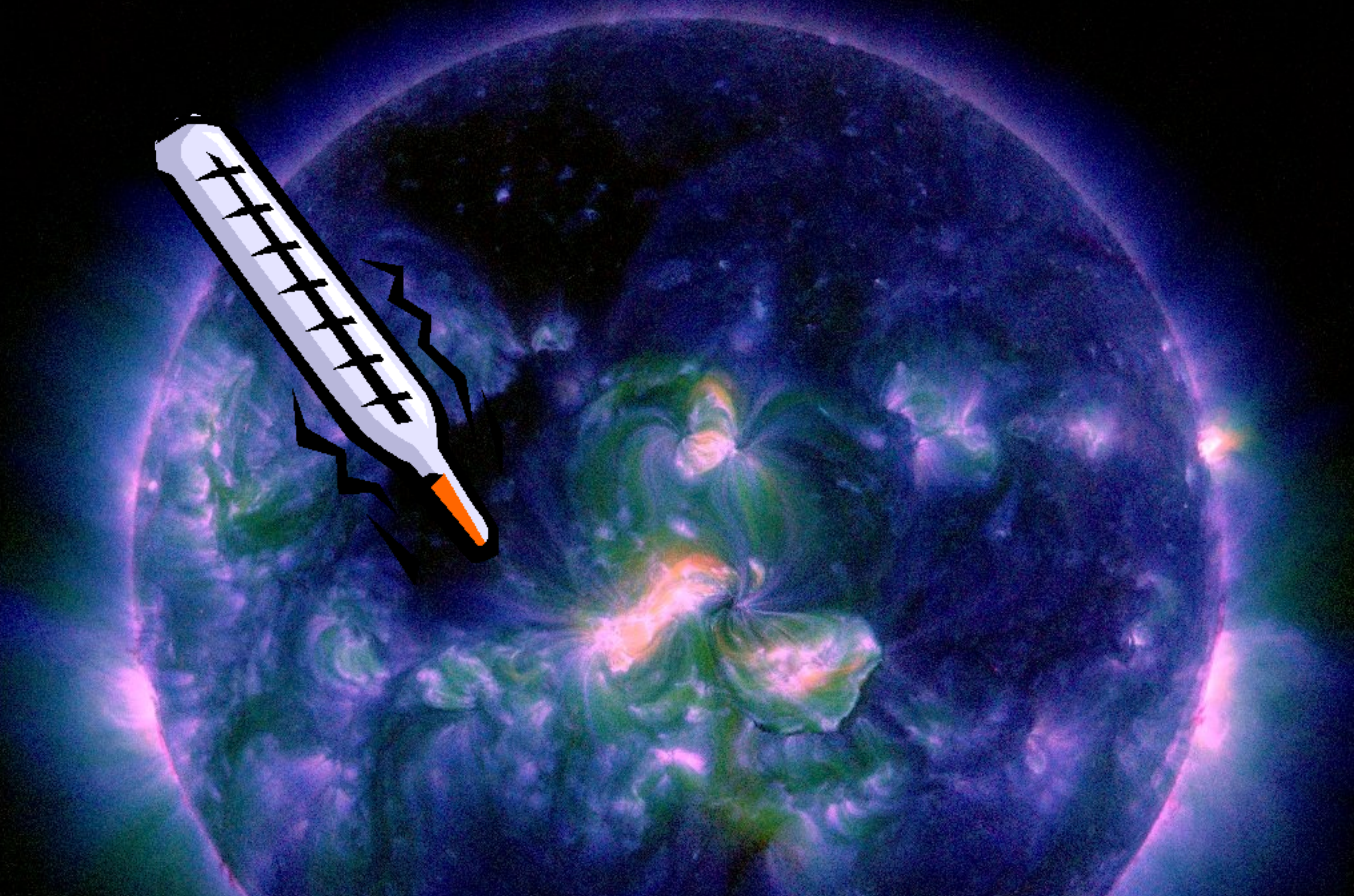

Statement of the Problem

The Atmospheric Imaging Assembly (AIA, Lemen et al. 2012; Boerner et al. 2012) instrument onboard NASA's Solar Dynamics Observatory (SDO, Pesnell et al. 2012) is a suite of four normal-incidence reflecting telescopes that image the Sun in seven EUV channels, two UV channels and one visible wavelength channel.

The aim of this and many other studies is to extract thermal information about the Sun's optically thin corona using the EUV observations. The calibrated (i.e. dark-subtracted, flat-fielded and exposure time normalized) count rate y_i in the i-th EUV channel is related to the thermal distribution of coronal plasma by:

$$y_i = \int_0^\infty K_i(T)\,\mathrm{DEM}(T) dT,$$

where $K_i(T)$ is the temperature response function (see next slide):

AIA Temperature Response Functions

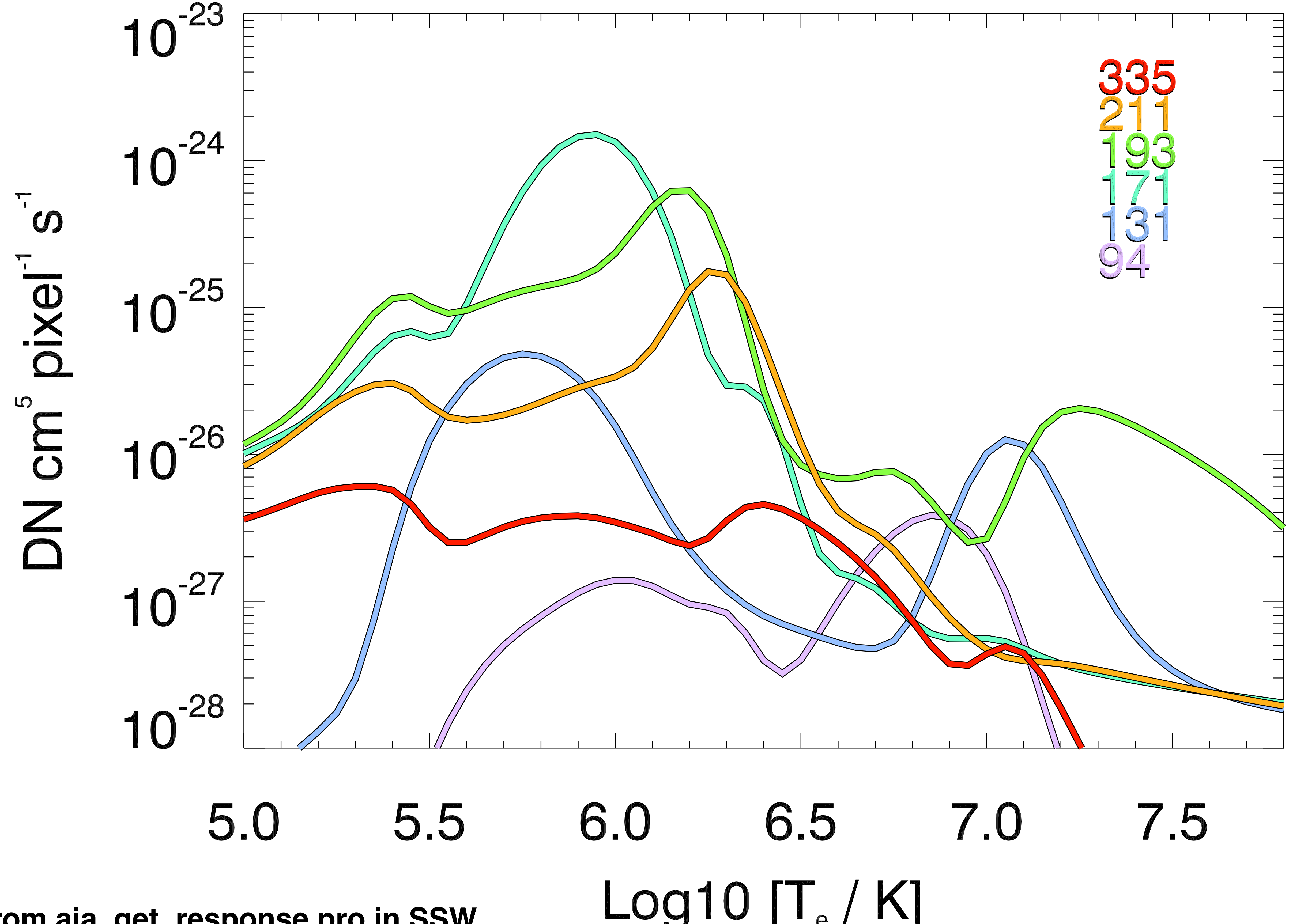

From aia_get_response.pro in SSW

Table 1. Predicted AIA count rates.

	Ion	λ	$T_{\mathrm{p}}^{\mathrm{a}}$	Fraction of total emission			
		Å	K	CH	QS	AR	FL
94 Å	Mg VIII	94.07	5.9	0.03	-	-	-
	Fe XX	93.78	7.0	-	-	-	0.10
	Fe XVIII	93.93	6.85	-	-	0.74	0.85
	Fe X	94.01	6.05	0.63	0.72	0.05	-
	Fe VIII	93.47	5.6	0.04	-	-	-
	Fe VIII	93.62	5.6	0.05	-	-	-
	Cont.			0.11	0.12	0.17	-
131 Å	O VI	129.87	5.45	0.04	0.05	-	-
	Fe XXIII	132.91	7.15	-	-	-	0.07
	Fe XXI	128.75	7.05	-	-	-	0.83
	Fe VIII	130.94	5.6	0.30	0.25	0.09	-
	Fe VIII	131.24	5.6	0.39	0.33	0.13	-
	Cont.			0.11	0.20	0.54	0.04
171 Å	Ni XIV	171.37	6.35	-	-	0.04	-
	Fe X	174.53	6.05	-	0.03	-	-
	Fe IX	171.07	5.85	0.95	0.92	0.80	0.54
	Cont.			-	-	-	0.23
193 Å	O V	192.90	5.35	0.03	-	-	-
	Ca XVII	192.85	6.75	-	-	-	0.08
	Ca XIV	193.87	6.55	-	-	0.04	-
	Fe XXIV	192.03	7.25	-	-	-	0.81
	Fe XII	195.12	6.2	0.08	0.18	0.17	-
	Fe XII	193.51	6.2	0.09	0.19	0.17	-
	Fe XII	192.39	6.2	0.04	0.09	0.08	-
	Fe XI	188.23	6.15	0.09	0.10	0.04	-
	Fe XI	192.83	6.15	0.05	0.06	-	-
	Fe XI	188.30	6.15	0.04	0.04	-	-
	Fe X	190.04	6.05	0.06	0.04	-	-
	Fe IX	189.94	5.85	0.06	-	-	-
	Fe IX	188.50	5.85	0.07	-	-	-
	Cont.			-	-	0.05	0.04
211 Å	Cr IX	210.61	5.95	0.07	-	-	-
	Ca XVI	208.60	6.7	-	-	-	0.09
	Fe XVII	204.67	6.6	-	-	-	0.07
	Fe XIV	211.32	6.3	-	0.13	0.39	0.12
	Fe XIII	202.04	6.25	-	0.05	-	-
	Fe XIII	203.83	6.25	-	-	0.07	-
	Fe XIII	209.62	6.25	-	0.05	0.05	-
	Fe XI	209.78	6.15	0.11	0.12	-	-
	Fe X	207.45	6.05	0.05	0.03	-	-
	Ni XI	207.92	6.1	0.03	-	-	-
	Cont.			0.08	0.04	0.07	0.41
304 Å	He II	303.786	4.7	0.33	0.32	0.27	0.29
	He II	303.781	4.7	0.66	0.65	0.54	0.58
	Ca XVIII	302.19	6.85	-	-	-	0.05
	Si XI	303.33	6.2	-	-	0.11	-
	Cont.			-	-	-	-
335 Å	Al X	332.79	6.1	0.05	0.11	-	-
	Mg VIII	335.23	5.9	0.11	0.06	-	-
	Mg VIII	338.98	5.9	0.11	0.06	-	-
	Si IX	341.95	6.05	0.03	0.03	-	-
	Si VIII	319.84	5.95	0.04	-	-	-
	Fe XVI	335.41	6.45	-	-	0.86	0.81
	Fe XIV	334.18	6.3	-	0.04	0.04	-
	Fe X	184.54	6.05	0.13	0.15	-	-
	Cont.			0.08	0.05	-	0.06

From O’Dwyer et al. 2010

Statement of the Problem

and $$\mathrm{DEM}(T)dT = \int_0^\infty n_e^2(T)dz,$$

where DEM(T) is the differential emission measure (in units of $\mathrm{cm}^{-5}\ \mathrm{K}^{-1}$) of plasma along the line-of-sight. $n_e(T)$ is the electron number density of plasma at temperature T. The challenge is to solve for DEM(T) given a set of EUV measurements **y**.

Let the temperature range be divided into n neighboring bins, so that:

$$y_i = \sum_{j=1}^{n} \int_{T_j}^{T_j+\Delta T_j} K_i(T)\mathrm{DEM}(T)dT,$$

where the j-th temperature bin has range $T \in [T_j, T_j+\Delta T_j)$. Assuming that $K_i(T)$ is piecewise constant in each temperature bin, we have:

$$y_i = \sum_{j=1}^{n} K_{ij}\mathrm{EM}_j, \text{where}\, \mathrm{EM}_j = \int_{T_j}^{T_j+\Delta T_j} \mathrm{DEM}(T)dT.$$

Statement of the Problem: y = Kx

$$y_i = \sum_{j=1}^{n} K_{ij} \mathrm{EM}_j, \text{ where } \mathrm{EM}_j = \int_{T_j}^{T_j + \Delta T_j} \mathrm{DEM}(T) dT.$$

The above is a matrix equation of the form **y** = K**x,** where

- K is an m x n response matrix*, with each row corresponding to the temperature response function of one AIA channel
- **y** is an m-tuple corresponding of AIA count (rates), and
- **x** is an n-tuple with components EM_j.

The He II line in the 304 Å channel is not well-modeled by CHIANTI (Warren, 2005, ApJ 157, 147) so it is usually not used for DEM analysis. So m = 6 for AIA. Usually we want more than 6 temperature bins. **For m < n, the matrix equation y = Kx represents an underdetermined system.**

*Matrix elements depends on basis functions used for computing the integral

Usual Approach: χ-squared Minimization

<u>**Function to minimize:**</u> **$| y - Kx |^2$ or $|(y - Kx)/\sigma|^2$**

Basically, minimize difference between observed and predicted counts. The benefits of a least-squares approach is that it leads to Euler-Lagrange equations that can be used to seek (global or local) minima.

For an overdetermined system, we know no single model will fit all the data. So χ-squared minimization is ideal. However, **for underdetermined systems such an approach can be subject to the perils of overfitting.**

Usual way to get around this:

Parameterization: e.g. Guennou et al (2012a,b), xrt_dem_iterative2.pro (M. Weber in SSW, see also Cheng et al 2012)

Regularization: e.g. Hannah & Kontar (2012), Plowman et al. (2013)

Cheung et al. 2015: The Sparse Solution

We address the inverse problem using an approach different than chi-squared minimization. The set of solutions satisfying the underdetermined matrix equation **y** = K**x** lies in an affine subspace of $\mathbf{R}^n$. We pick the solution $\mathbf{x}^{\#}$ within this subspace such that:

$$\text{minimize} \sum_{j}^{n} \mathrm{x}_j \text{ subject to } \mathcal{K}\vec{x} = \vec{y},\ \vec{x} \geq 0.$$

The linear program above finds a solution that minimizes the L1-norm of the solution vector (c.f. Candes 2006). This is not chi-squared minimization.

If K is the response function sampled by Dirac Delta functions at specific temperatures, this is equivalent to minimizing the total EM. If other basis functions are used, there is no simple corresponding physical interpretation.

The Sparse Solution

We are unaware of physical principles pertaining to coronal plasma that motivate the optimization problem posed above. However, this choice has some important benefits:

1) It does not overfit (consistent with the principle of parsimony, i.e. Ockham's Razor).
2) It ensures positivity of the solution (if solutions exist).
3) It is an L1-norm minimization problem, so we can use standard techniques from compressed sensing (c.f. Candes & Tao 2006).
   BTW the L1-norm of a vector $x = \mathbf{\Sigma}\, |x_i|$
4) Speed: $O(10^4)$ solutions / sec with single IDL thread.

See Asensio Ramos & De La Cruz Rodriguez (2015) for application of related techniques to 2D coupled Stokes inversion.

Handling noise

In practice, measurement uncertainties imply that the equality **y** = K**x** may not be satisfied. So our method solves the followed modified linear program:

$$\text{minimize } \sum_j^n \mathrm{x}_j \text{ subject to } \mathcal{K}\vec{x} \le \vec{y} + \vec{\eta},$$
$$\vec{x} \ge 0,\ \mathcal{K}\vec{x} \ge \max(\vec{y} - \vec{\eta}, 0).$$

The vector **η** is a measure of the uncertainty in the count rate and provides tolerance for the predicted counts (K**x)** to deviate from the observed values (**y**). To enforce positive counts the lower bound is set to max(**y**-**η**, 0).

χ-squared minimization vs. Sparse inversion

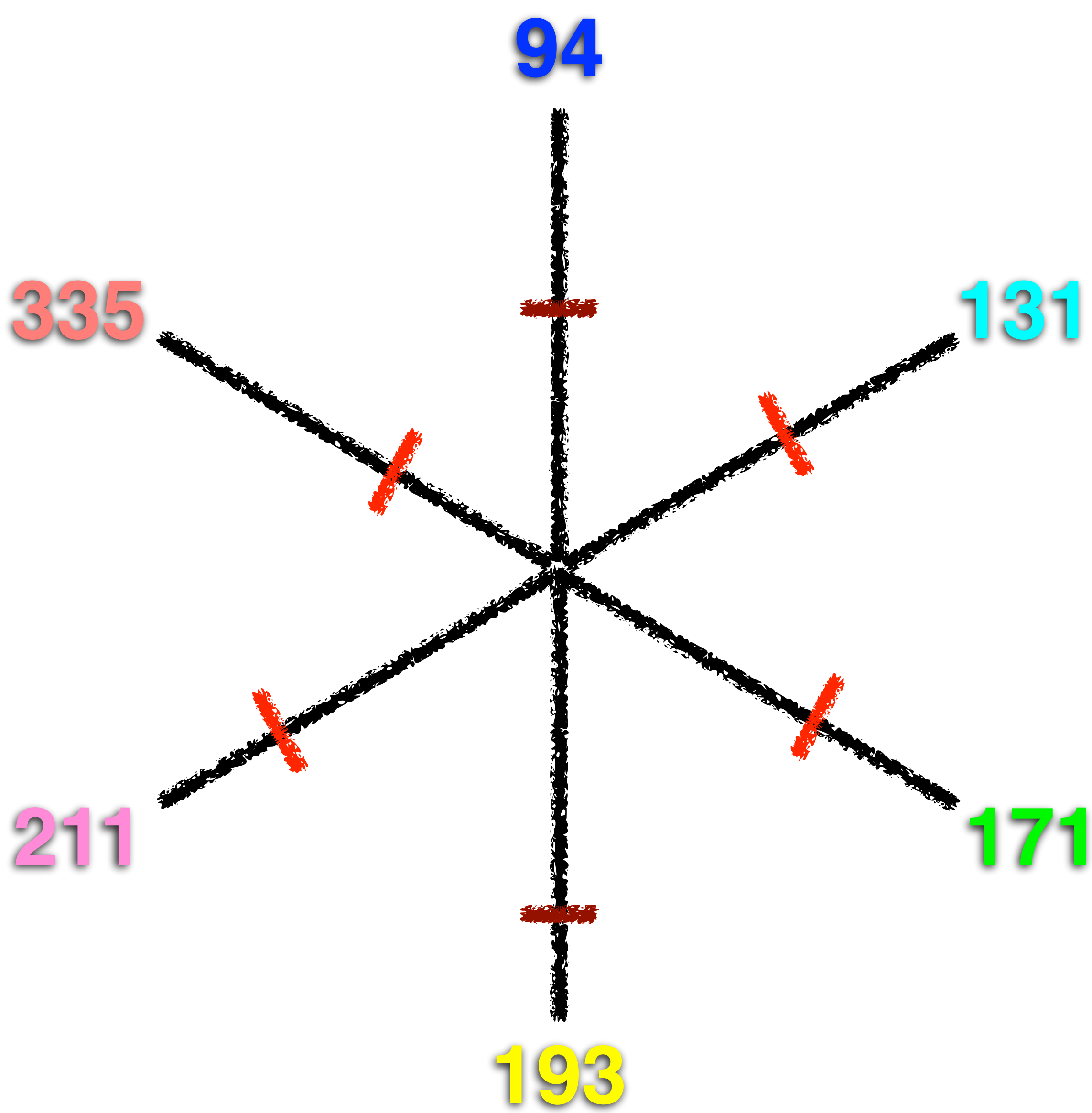

vs.

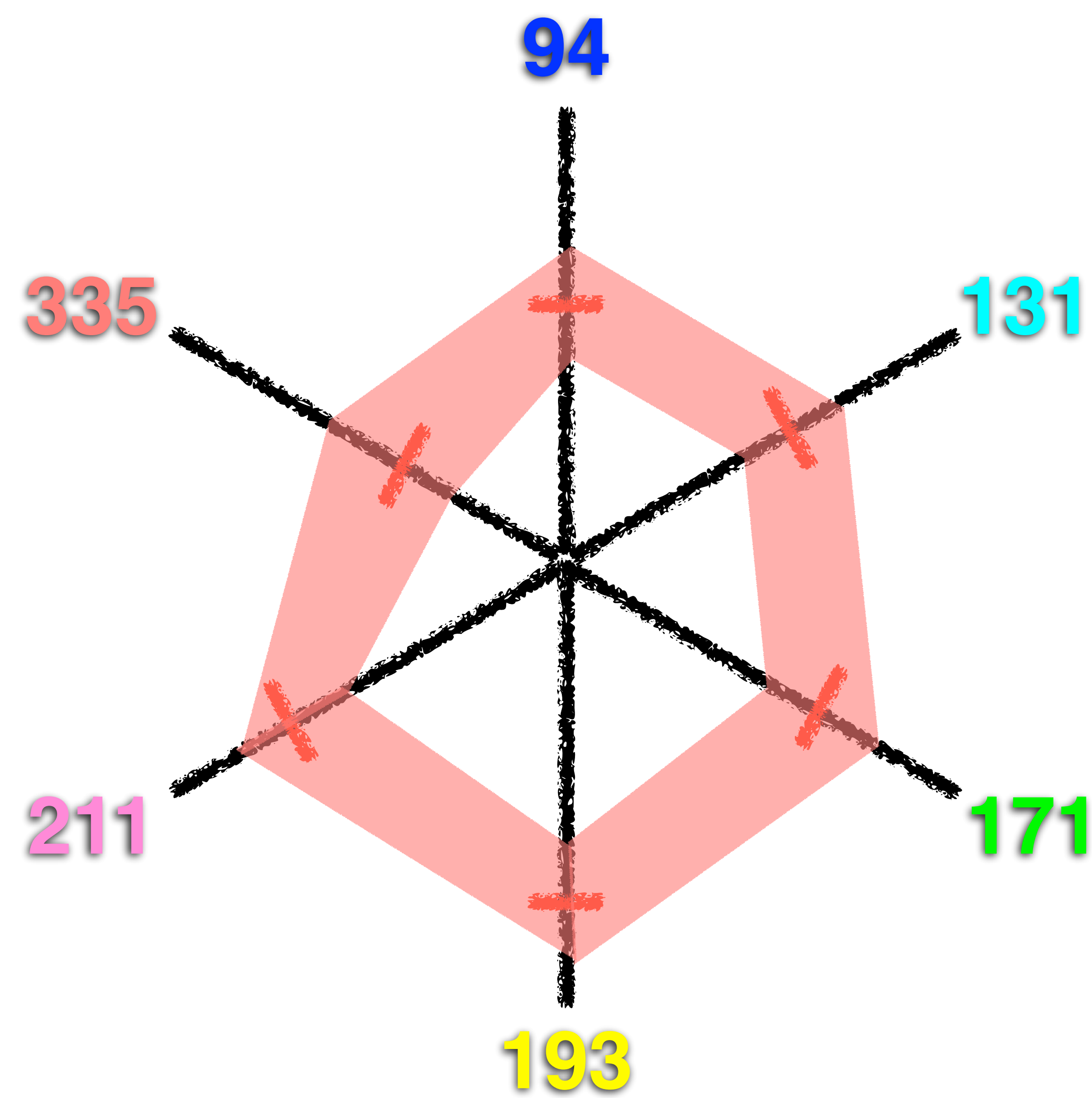

Crossmarks are observed counts

Subspace of allowed solutions in our method

Basis Functions for DEM

Let $i = 1, 2, ..., m$ denote the index over a set of wavelength band channels and/or line spectra. Let the DEM function be written in terms of a set of positive semidefinite basis functions $\{b_j(\log T) \geq 0 \mid k = 1, 2, ..., l\}$, viz.

$$\mathrm{DEM}(\log T) = \sum_{k=1}^{l} b_k(\log T) x_k, \tag{A1}$$

with quadrature coefficients $x_k \geq 0$. Approximating the integrals in equation (1) as sums in $\log T$ space, we have

$$y_i = \sum_{j=1}^{n} \sum_{k=1}^{l} K_{ij} B_{jk} x_k \Delta \log T, \tag{A2}$$

where $j = 1, 2, ..., n$ is the index over temperature bins, $K_{ij} = K_i(\log T_j)$ and $B_{jk} = b_k(\log T_j)$. The response matrix $\mathbf{K} = (K_{ij})$ has dimensions $m \times n$. The basis matrix $\mathbf{B} = (B_{jk})$ has dimensions $n \times l$, with the k-th column vector corresponding to the k-th basis function $b_k(\log T_j)$. Defining the *dictionary matrix* $\boxed{\mathbf{D} = \mathbf{KB}}$, the set of integral equations (1) can be written in matrix form:

In practice we solve this ➜

$$\boxed{\vec{y} = \mathbf{D}\vec{x},} \tag{A3}$$

where the sought-after solution vector $\vec{x}$ is an l-tuple with components $x_k \Delta \log T$ $(k = 1, 2, ..., l)$. When the number of basis functions exceeds the number of image channels (i.e. $l > m$), the linear system Eq. (A3) is underdetermined.

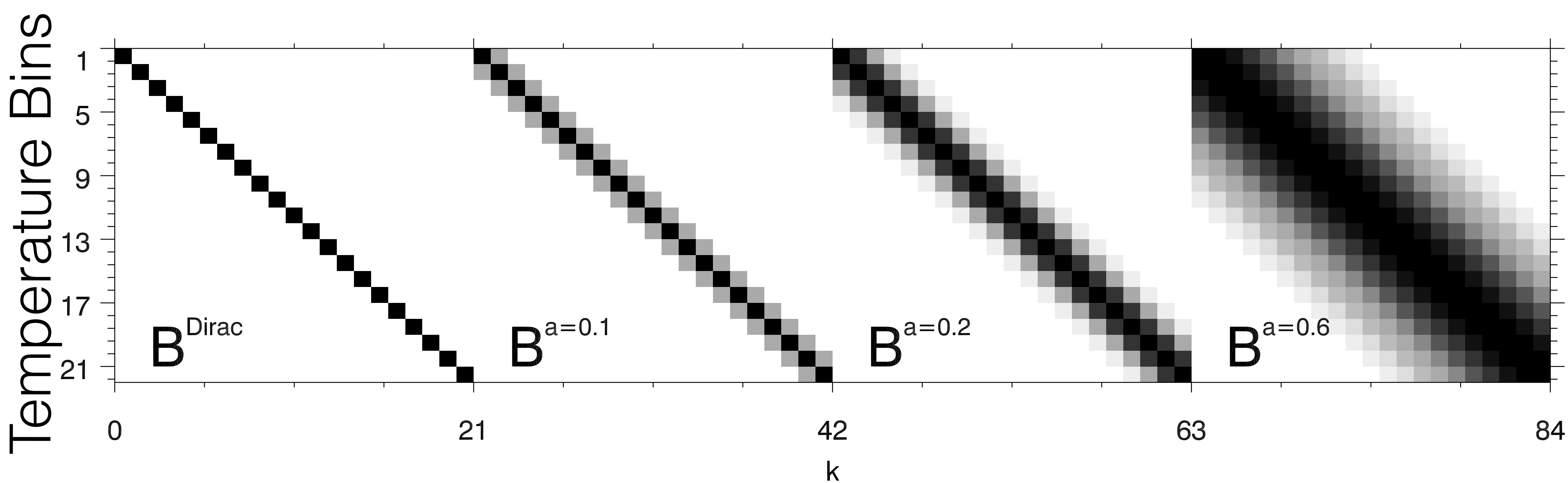

Validation Exercise 1: Gaussian DEMs

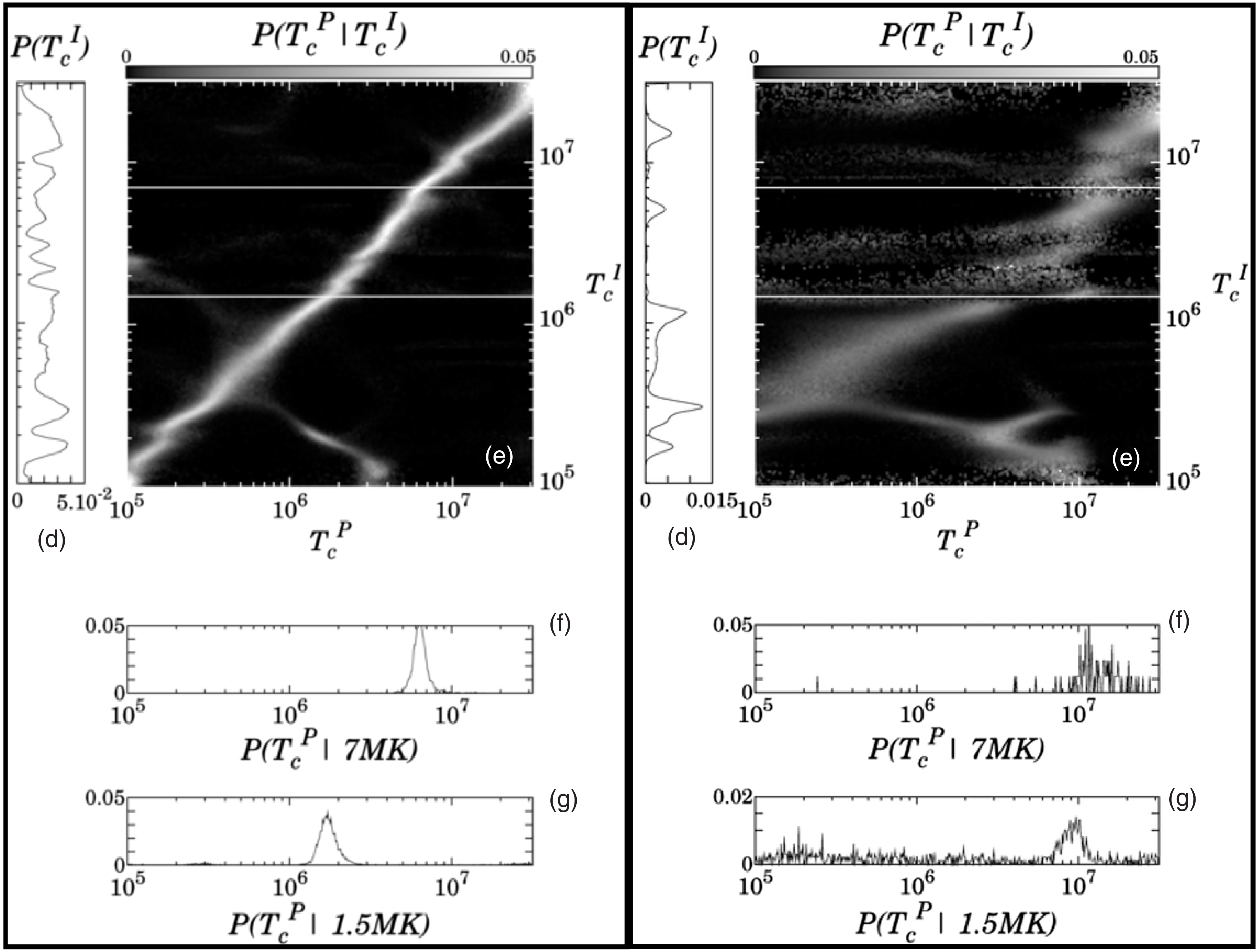

Guennou et al (2012) reported that when the input gaussian is moderately wide (0.3 log Te, right panel), AIA 6-channel inversions yield spurious temperatures.

Test DEMs: $\xi(T, T_c, \sigma) = \frac{\mathrm{EM}_0}{\sigma\sqrt{2\pi}} \exp\left[-\frac{(\log T - \log T_c)^2}{2\sigma^2}\right]$ $\mathrm{EM}_0 = 10^{29}\ \mathrm{cm}^2$

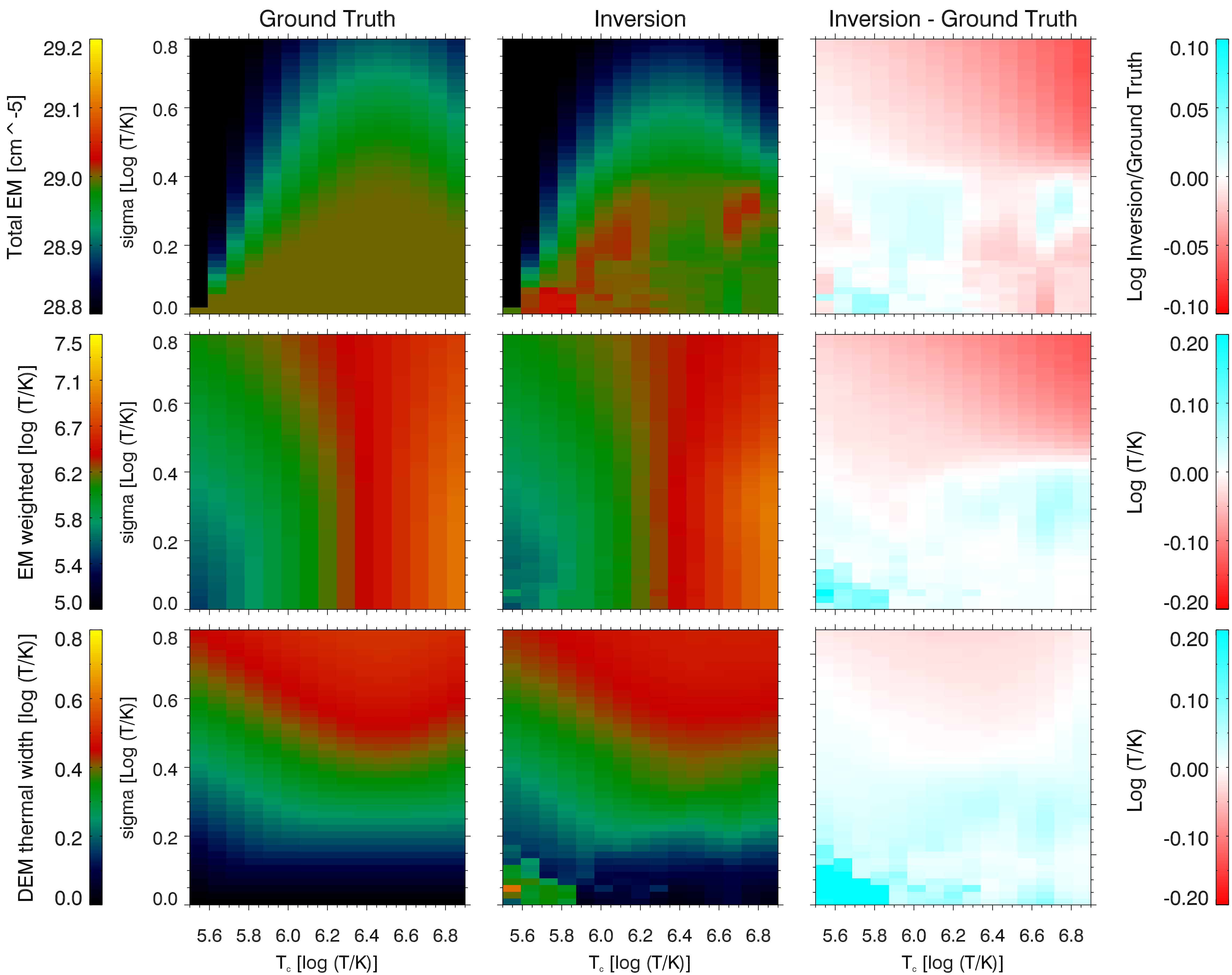

Validation Exercise 2: Quasi-steady loops in a NLFFF model of AR 11158

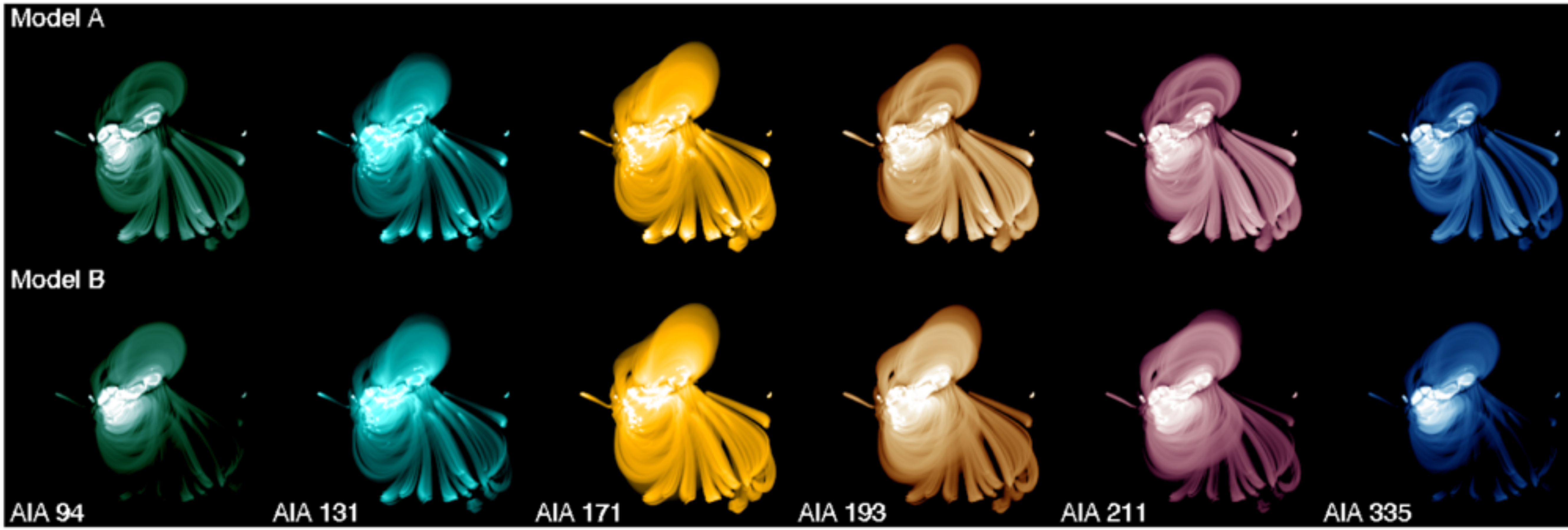

FIG. 5.— Synthetic AIA images (log-scaled) for the two thermal models (top and bottom rows) of NOAA AR 11158.

Magnetic Model: Quasi-Grad-Rubin Non-linear force-free Field reconstruction of AR 11158.

Thermal Model: Quasi-steady loops with different heating functions.

AR 11158 Model A

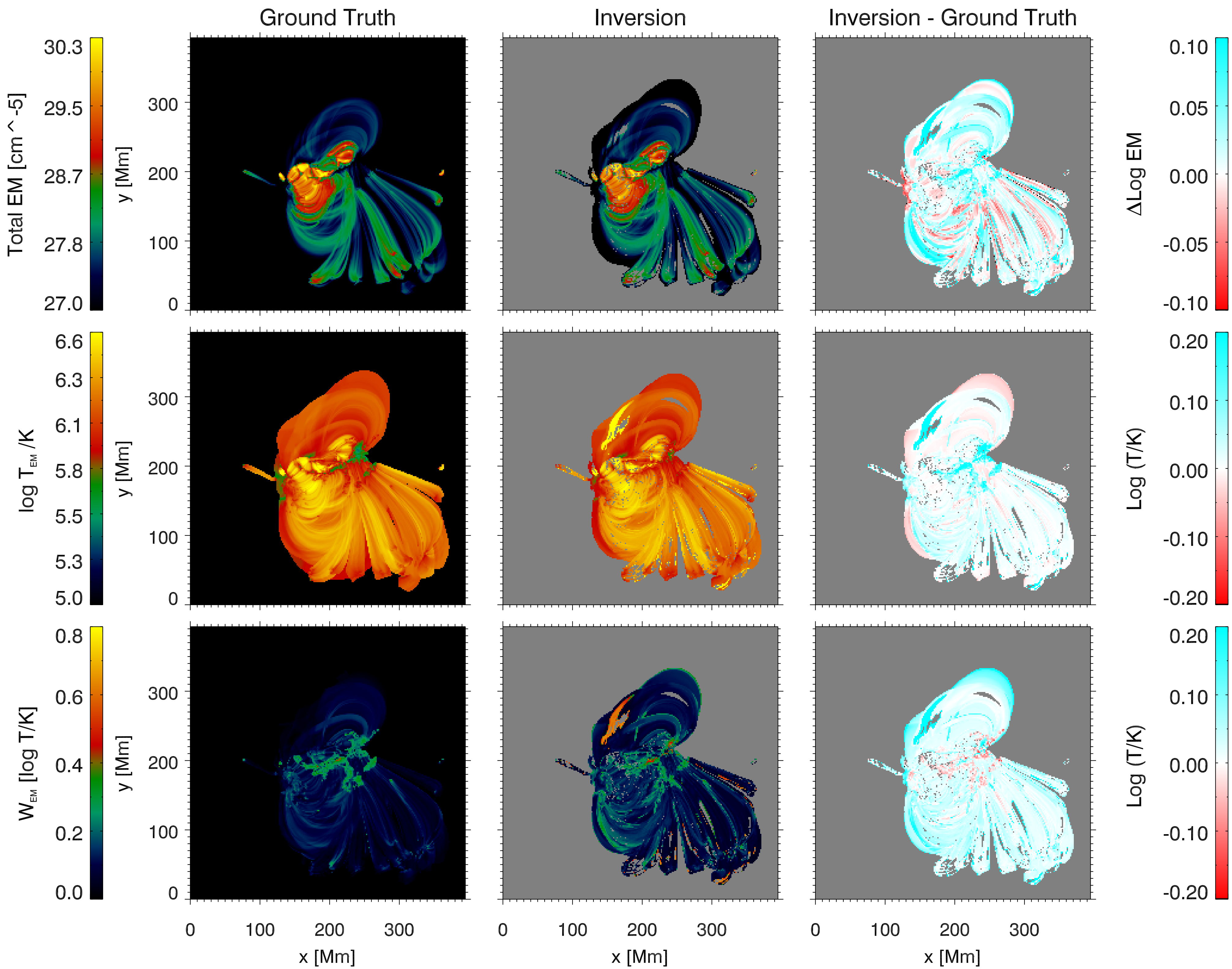

AR 11158 Model B

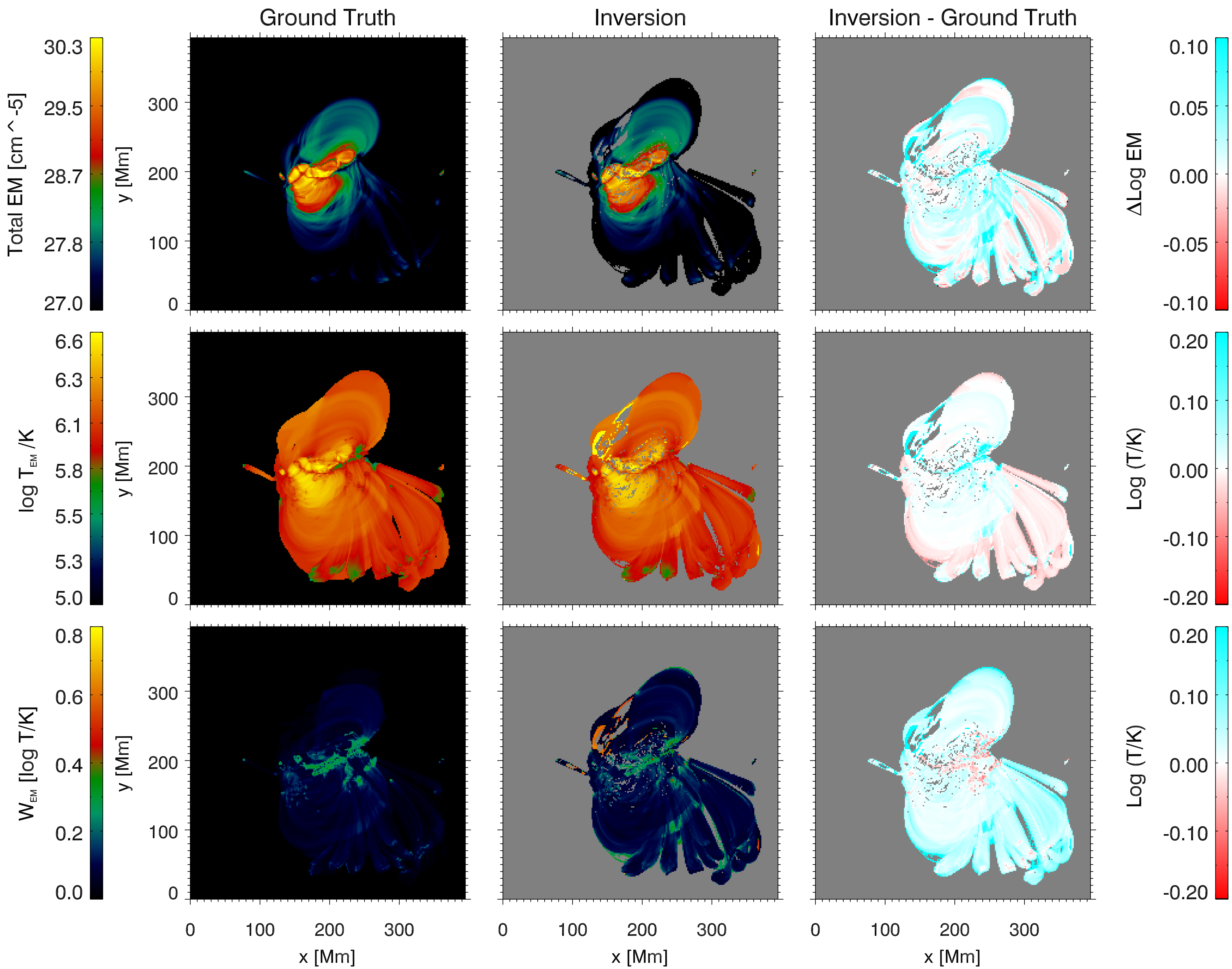

Validation Exercise 3: MHD Model

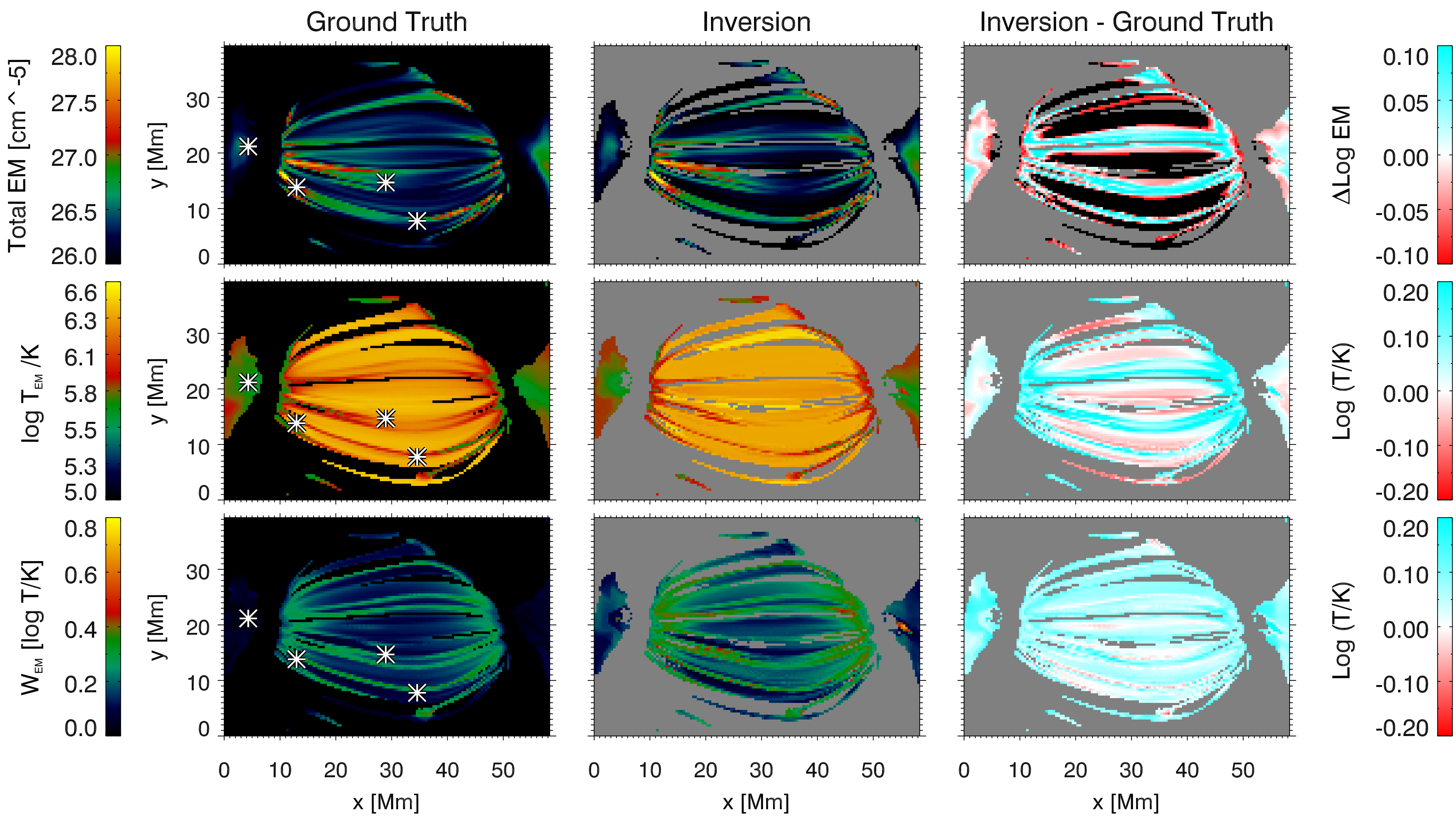

MHD model of AR formation (with thermal conduction) by Chen et al. (2014A&A…564A..12C, 2015NatPh..11..492C)

Validation Exercise 3: MHD Model

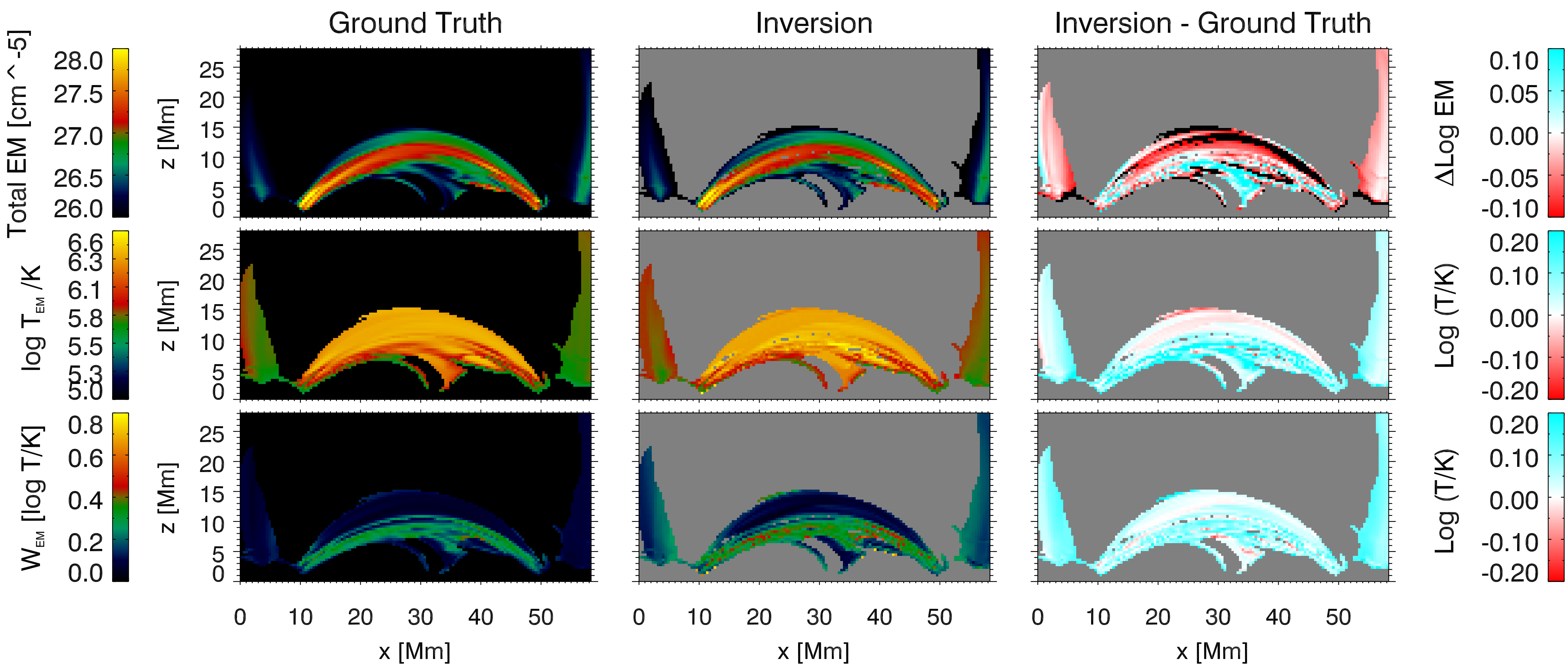

MHD model of AR formation (with thermal conduction) by Chen et al. (2014A&A…564A..12C, 2015NatPh..11..492C)

Validation Exercise 4*: AIA-XRT Cross-Comparison

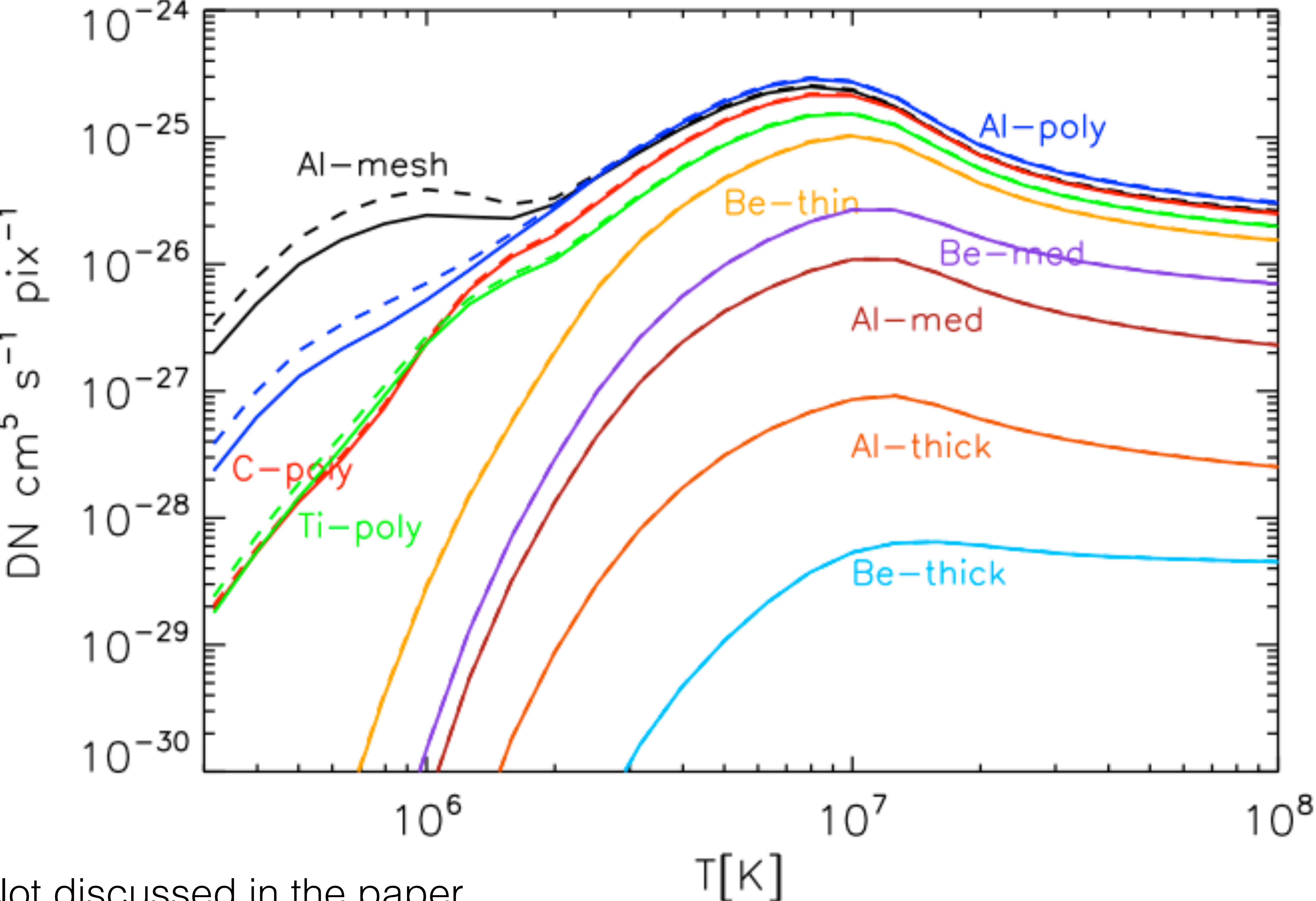

*Not discussed in the paper

AIA-XRT Cross-Comparison Analysis Procedure

1. Load and prep an XRT image.
2. Cutout AIA 94, 131, 171, 193, 211 & 335 level 1.5 data for XRT FOV as indicated by FITS keywords.
    1. DEM inversion (sun_coronal_ext.abund, chianti.ioneq).
    2. Sample DEMs onto XRT plate scale.
    3. Synthesize XRT image by folding response function against AIA DEM.
3. Use tr_get_disp to align actual and synthetic XRT images.
4. Compare (following slides).

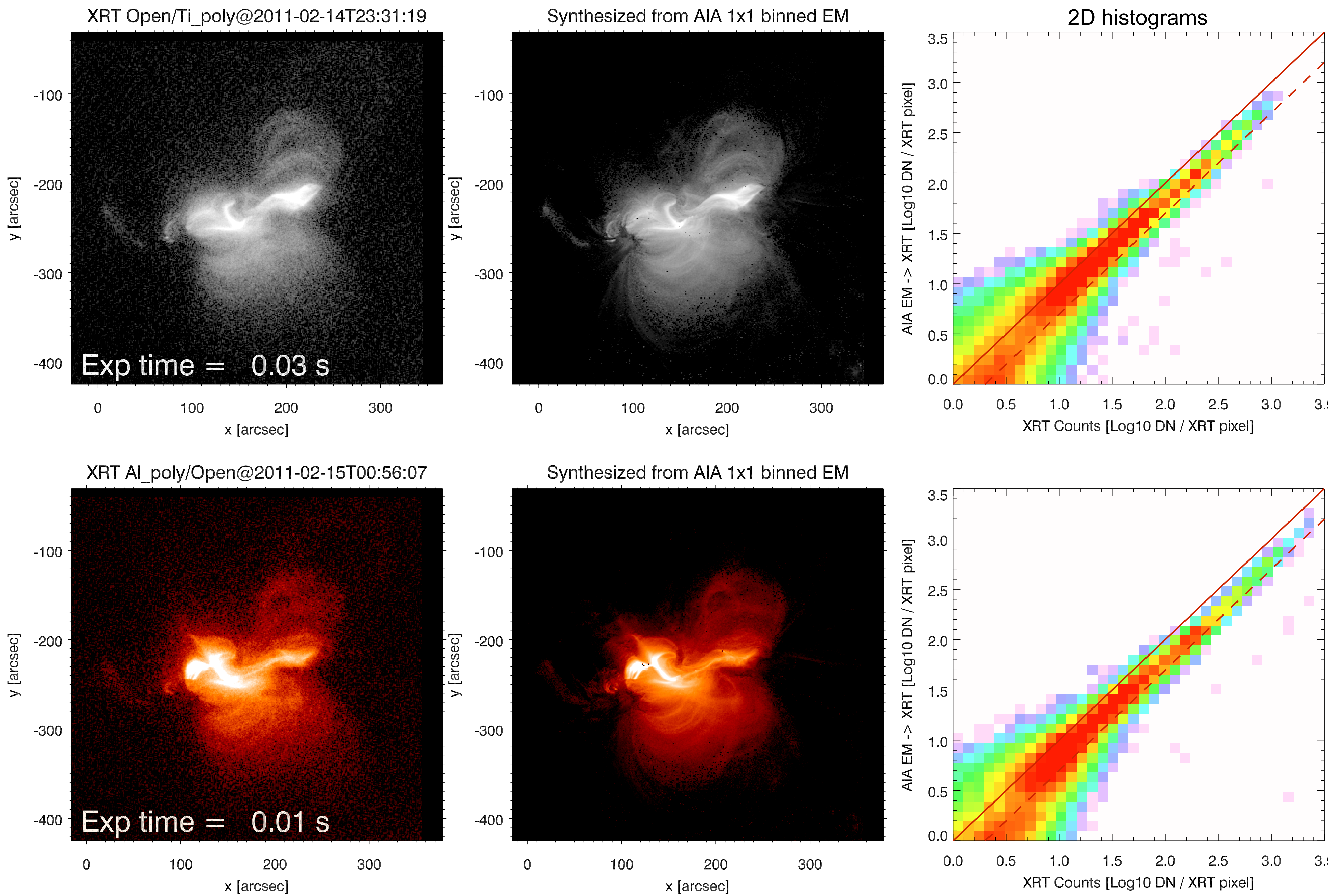
XRT Open/Ti_poly@2011-02-14T23:31:19
Exp time = 0.03 s
Synthesized from AIA 1x1 binned EM
2D histograms
AIA EM -> XRT [Log10 DN / XRT pixel]
XRT Counts [Log10 DN / XRT pixel]
XRT Al_poly/Open@2011-02-15T00:56:07
Exp time = 0.01 s
Synthesized from AIA 1x1 binned EM
y [arcsec]
x [arcsec]

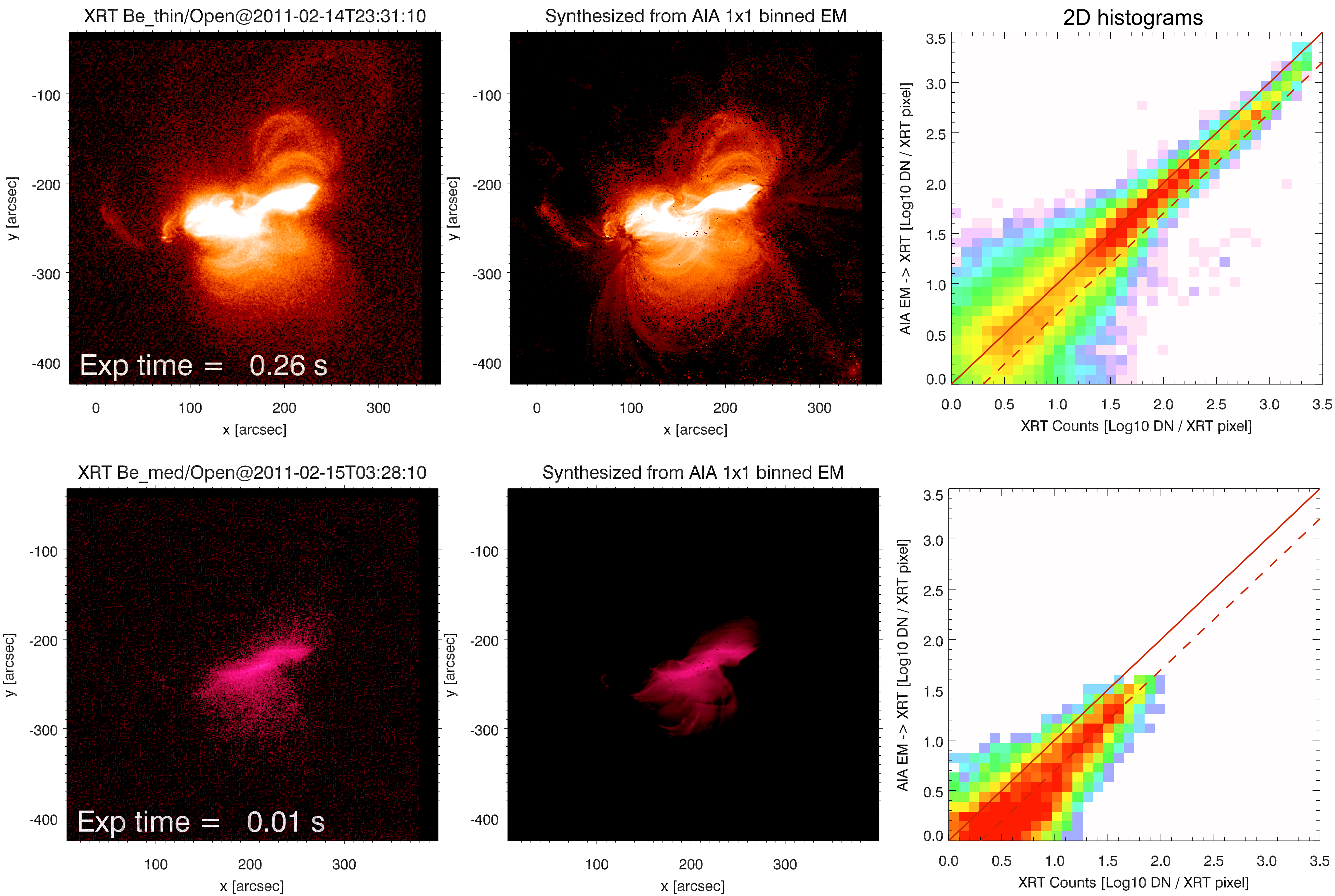

XRT Be_thin/Open@2011-02-14T23:31:10
Exp time = 0.26 s
Synthesized from AIA 1x1 binned EM
2D histograms
y [arcsec]
x [arcsec]
AIA EM -> XRT [Log10 DN / XRT pixel]
XRT Counts [Log10 DN / XRT pixel]
XRT Be_med/Open@2011-02-15T03:28:10
Exp time = 0.01 s
Synthesized from AIA 1x1 binned EM

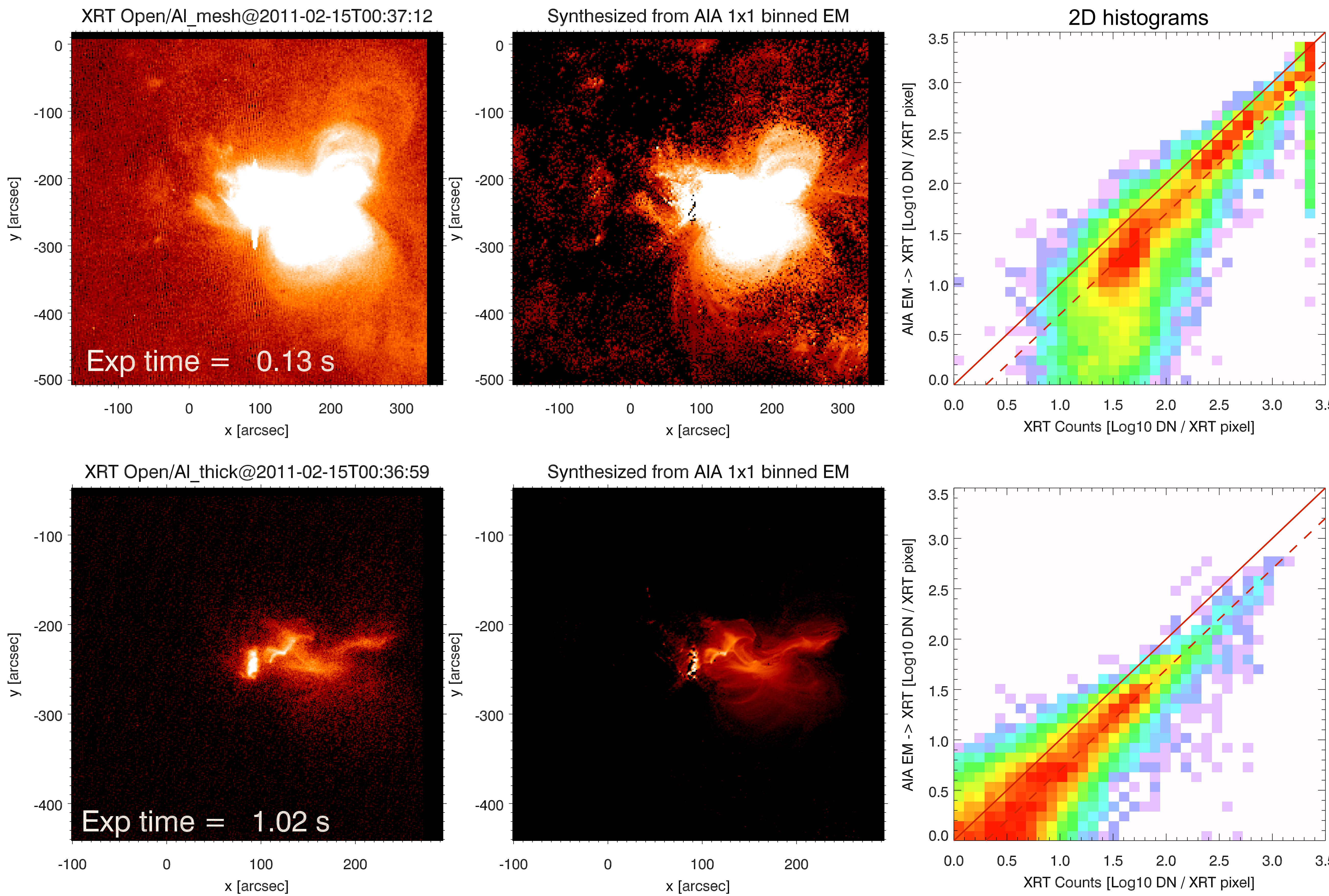

XRT Open/Al_mesh@2011-02-15T00:37:12
Synthesized from AIA 1x1 binned EM
2D histograms
Exp time = 0.13 s
y [arcsec]
x [arcsec]
AIA EM -> XRT [Log10 DN / XRT pixel]
XRT Counts [Log10 DN / XRT pixel]
XRT Open/Al_thick@2011-02-15T00:36:59
Synthesized from AIA 1x1 binned EM
Exp time = 1.02 s

Synthetic XRT Images

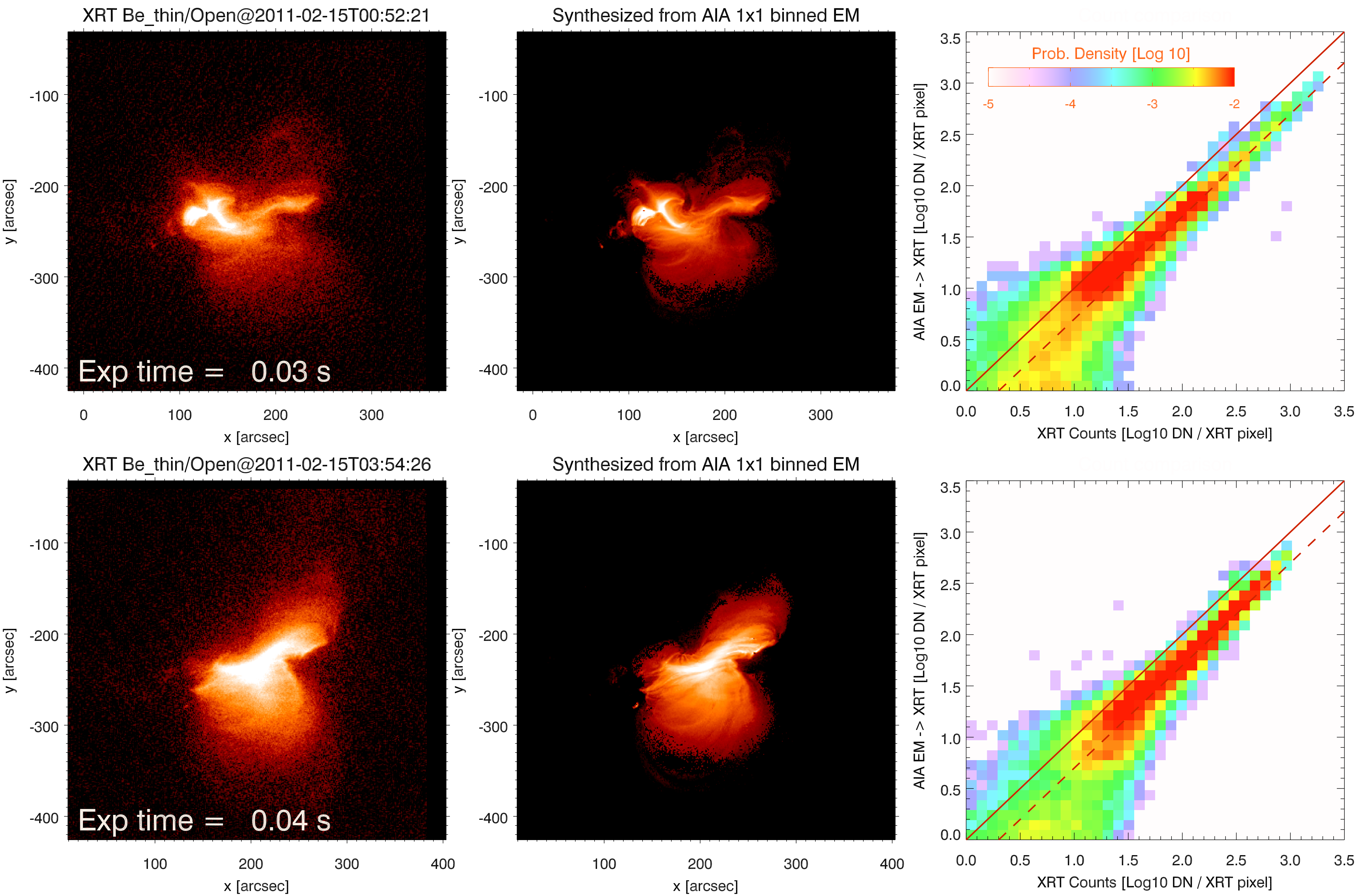

Validation Exercise 4: AIA-XRT Cross-Comparison

- Synthetic XRT images from DEMs derived using only AIA Reproduces morphology, but counts are too low compared to XRT by ~ 30 - 40%.

- Is this good enough?

- Is the discrepancy between synthetic and real XRT images due to limitations of the inversion, or due to uncertainties of the absolute calibration of both instruments?

Log-normal DEMs: AIA 6 channels only

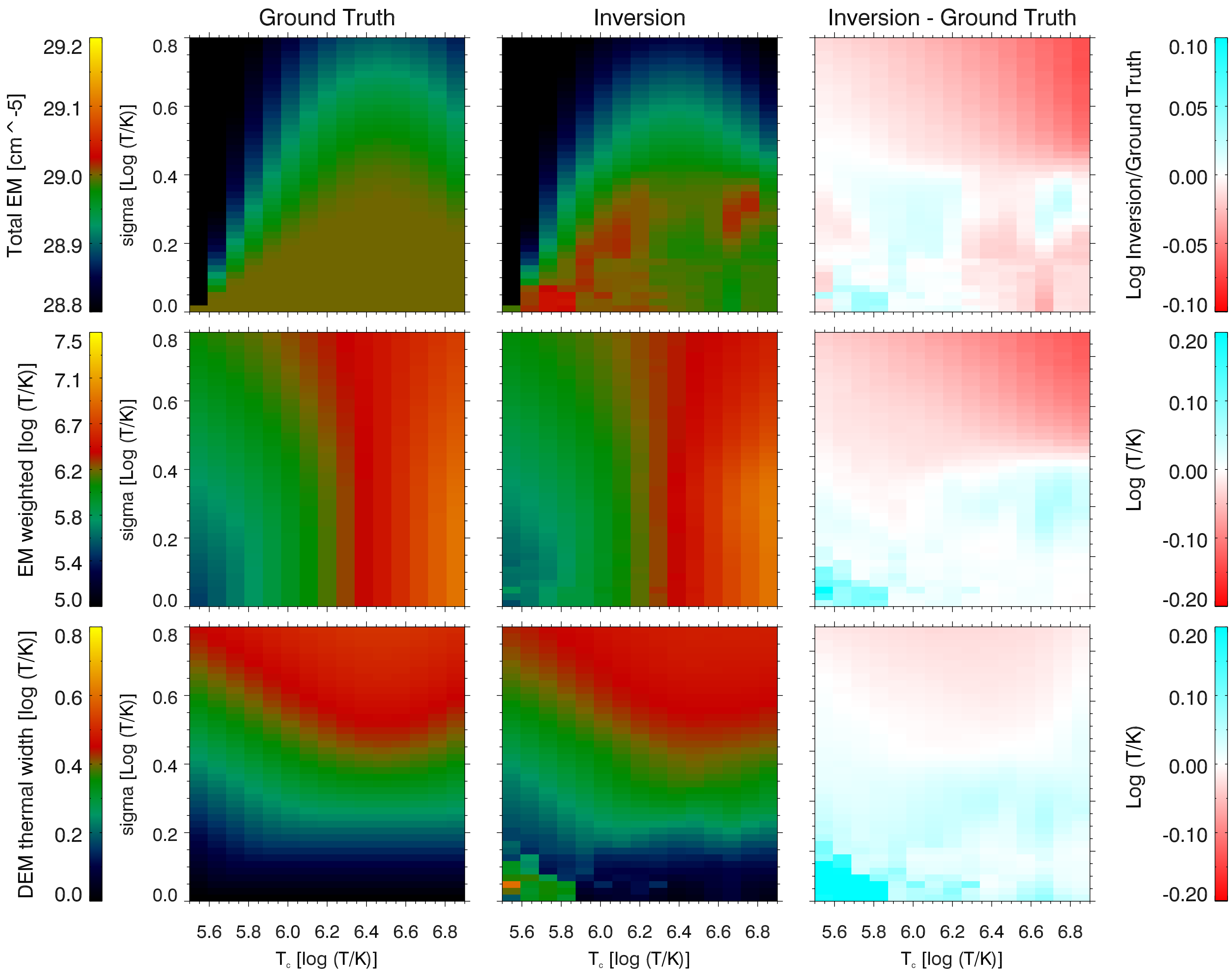

Log-normal DEMs: AIA 6 channels + XRT Be-thin

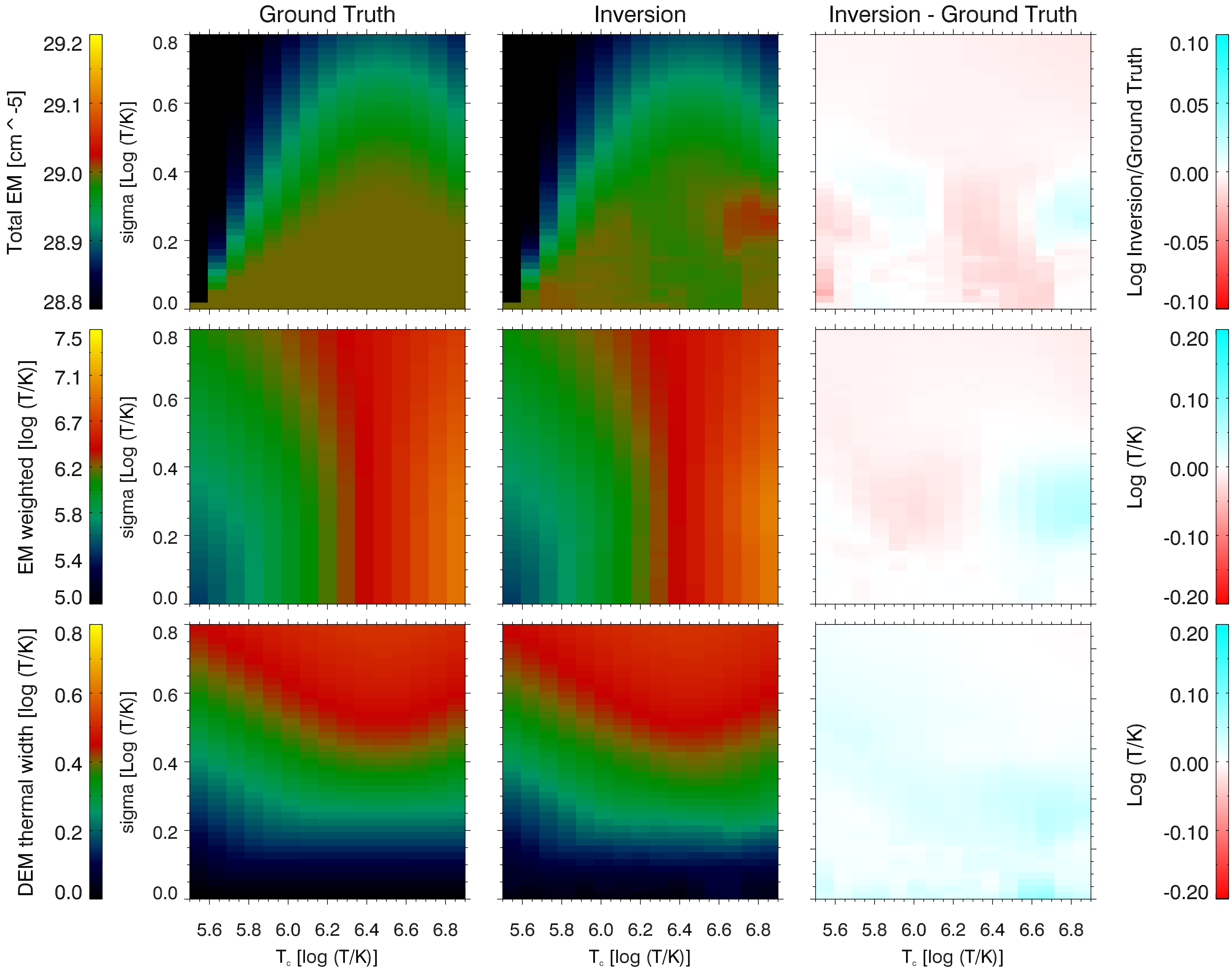

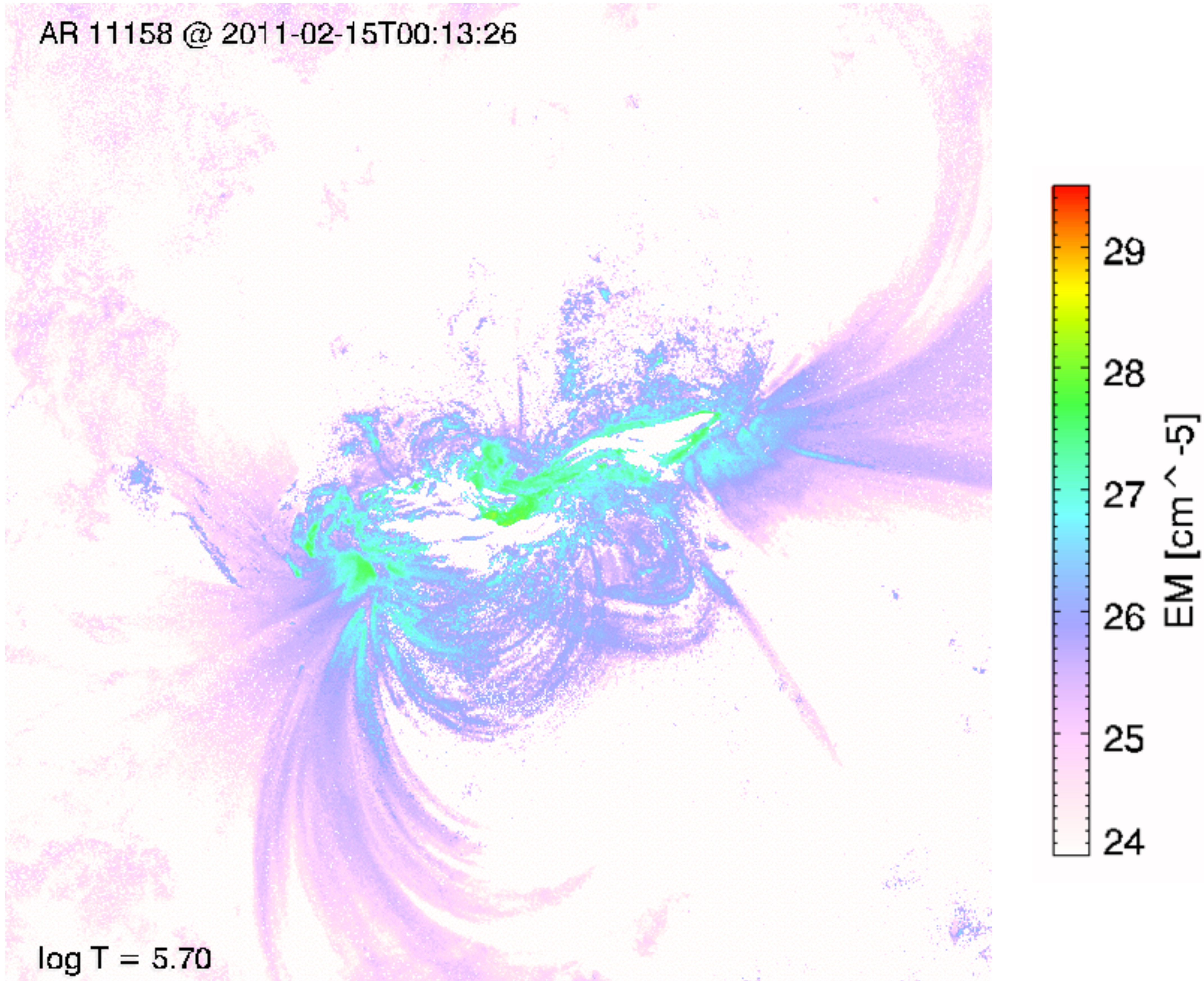

AR 11158 @ 2011-02-15T00:13:26
log T = 5.70
29
28
27
26
25
24
EM [cm^-5]

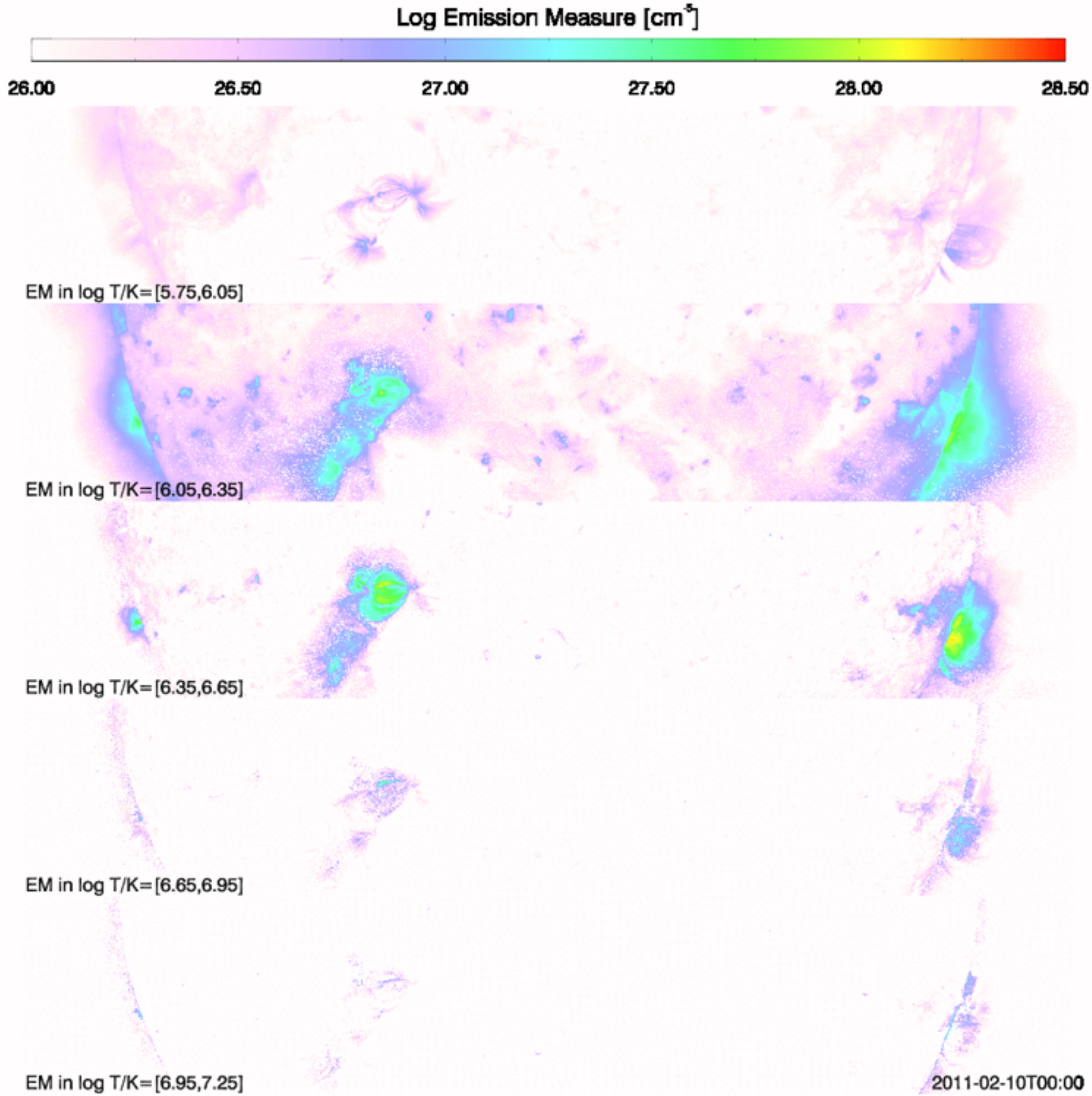

Log Emission Measure [cm^{-5}]
26.00
26.50
27.00
27.50
28.00
28.50
EM in log T/K=[5.75,6.05]
EM in log T/K=[6.05,6.35]
EM in log T/K=[6.35,6.65]
EM in log T/K=[6.65,6.95]
EM in log T/K=[6.95,7.25]
2011-02-10T00:00

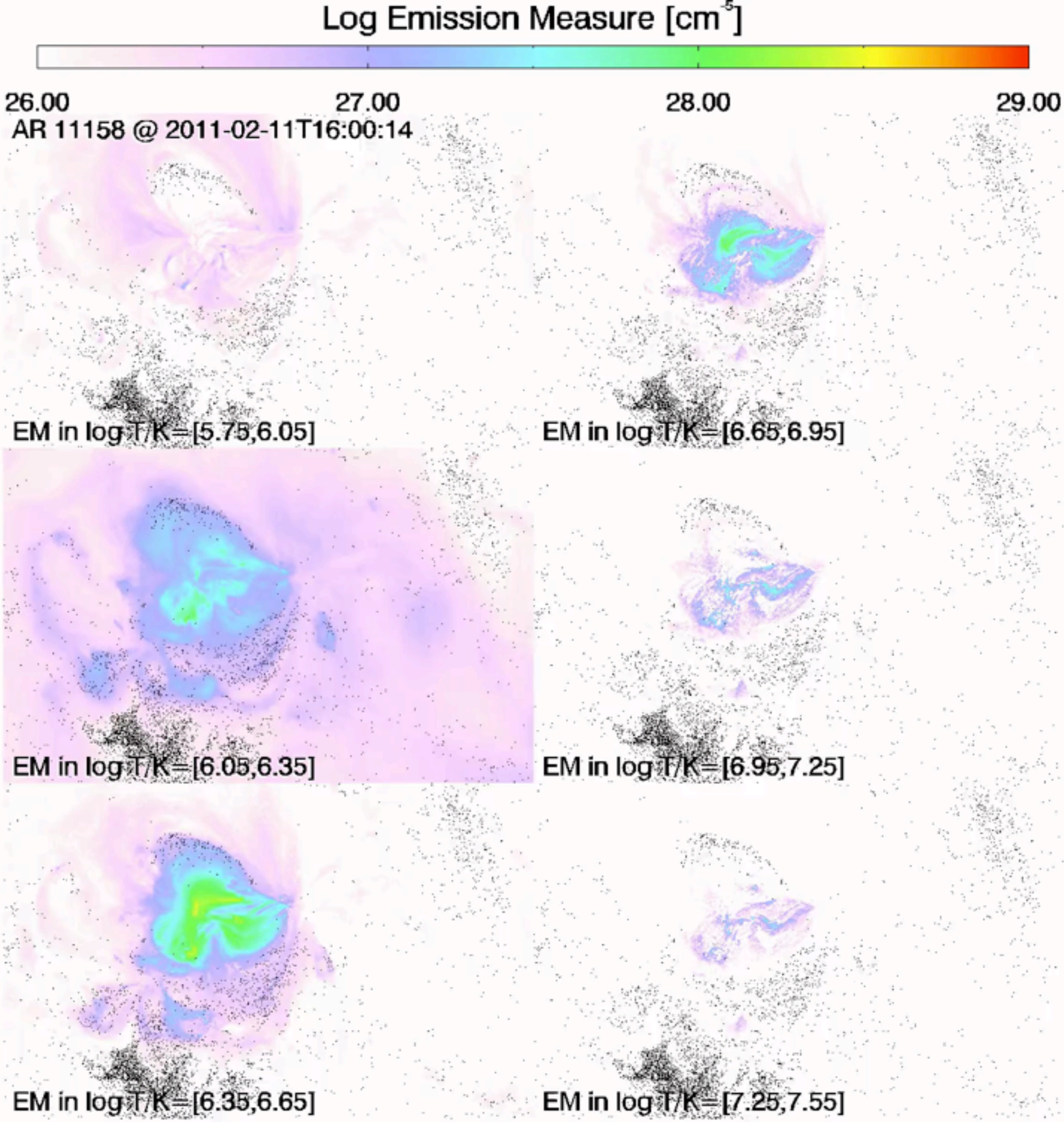

DEM movie of the emergence of AR 11158

Black pixels are where no solutions were found

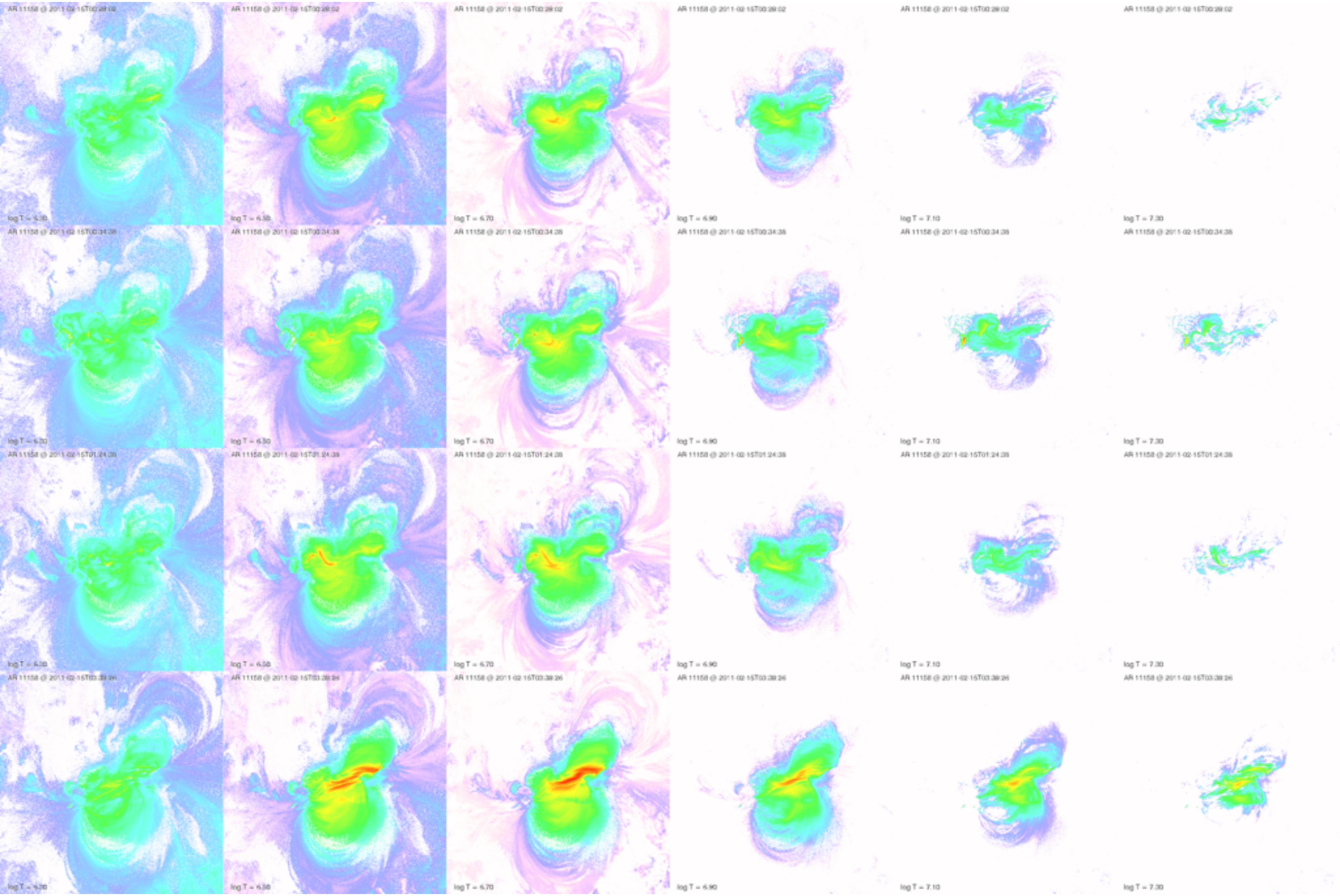

log T = 6.3 log T = 6.5 log T = 6.7 log T = 6.9 log T = 7.1 log T = 7.3

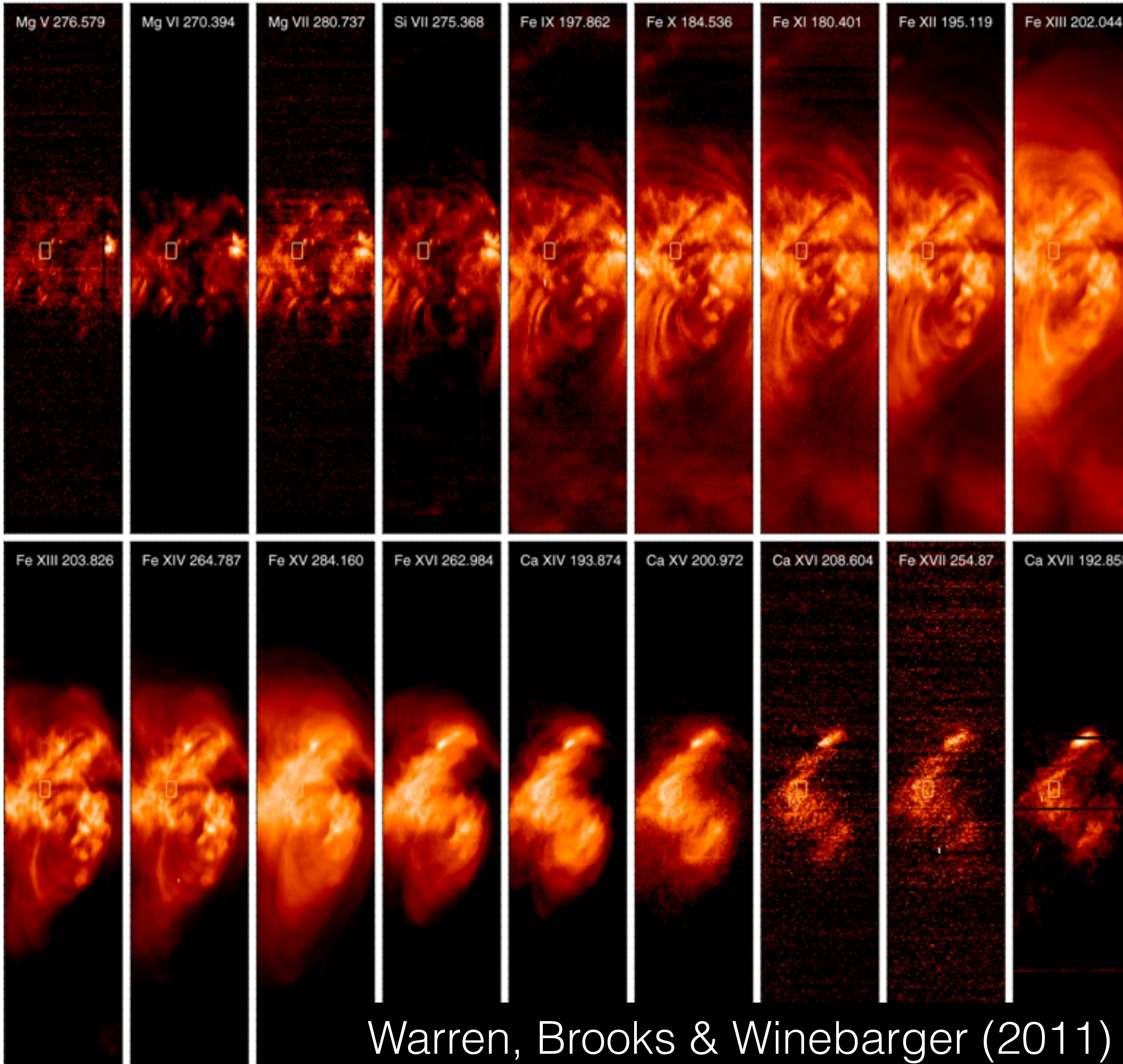

Warren, Brooks & Winebarger (2011)

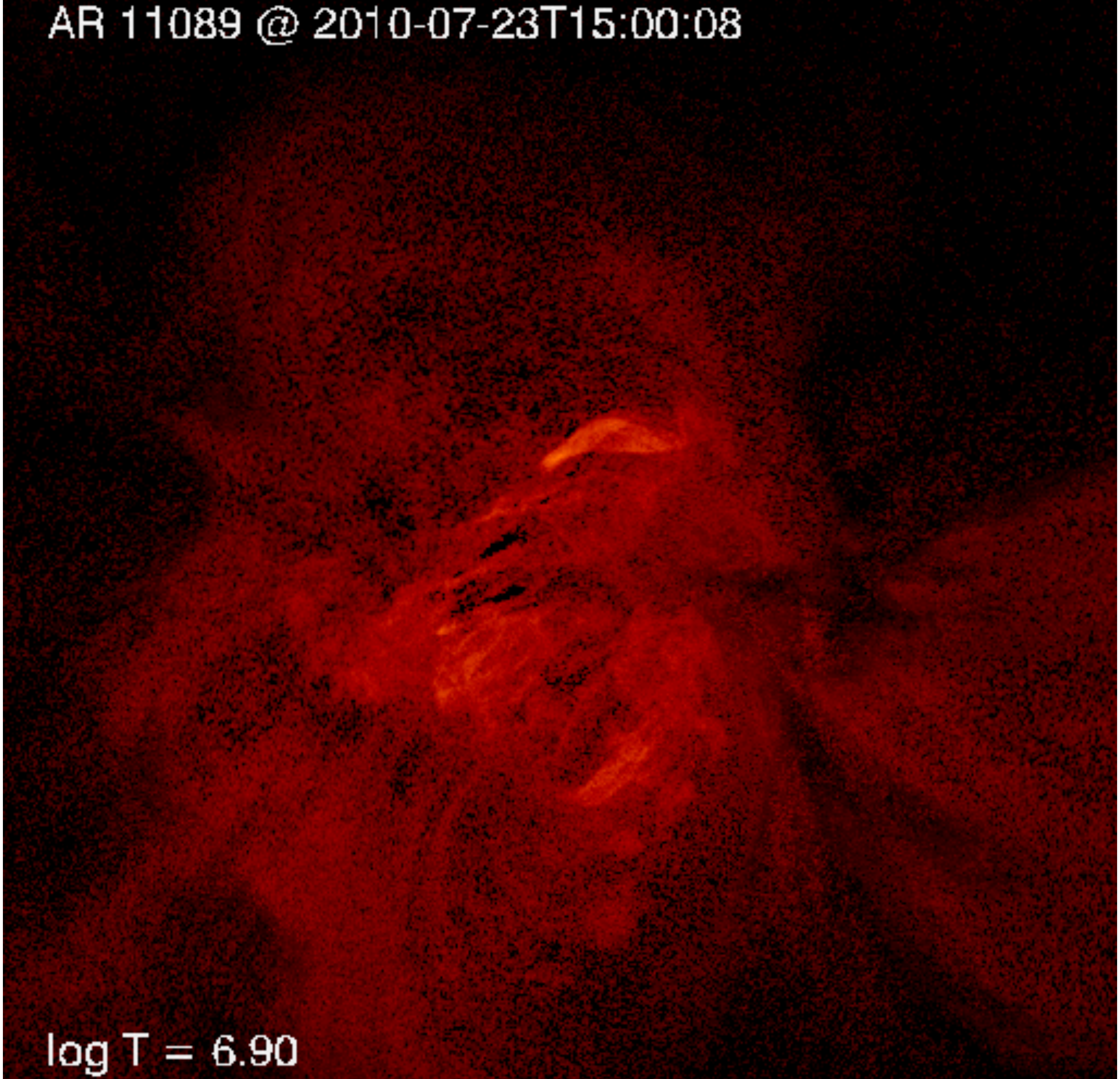
AR 11089 @ 2010-07-23T15:00:08
log T = 6.90

Side benefit: Image Denoising

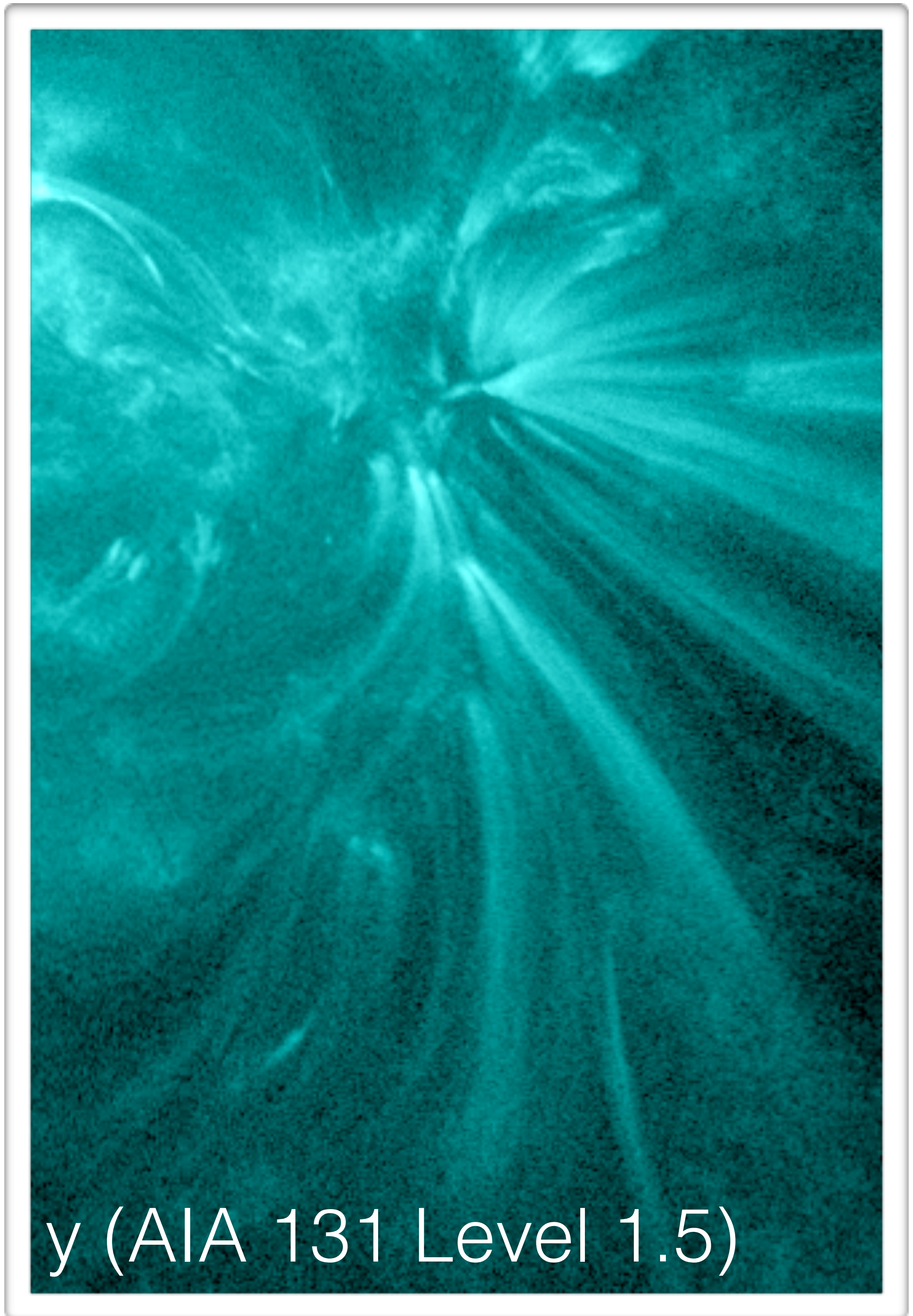

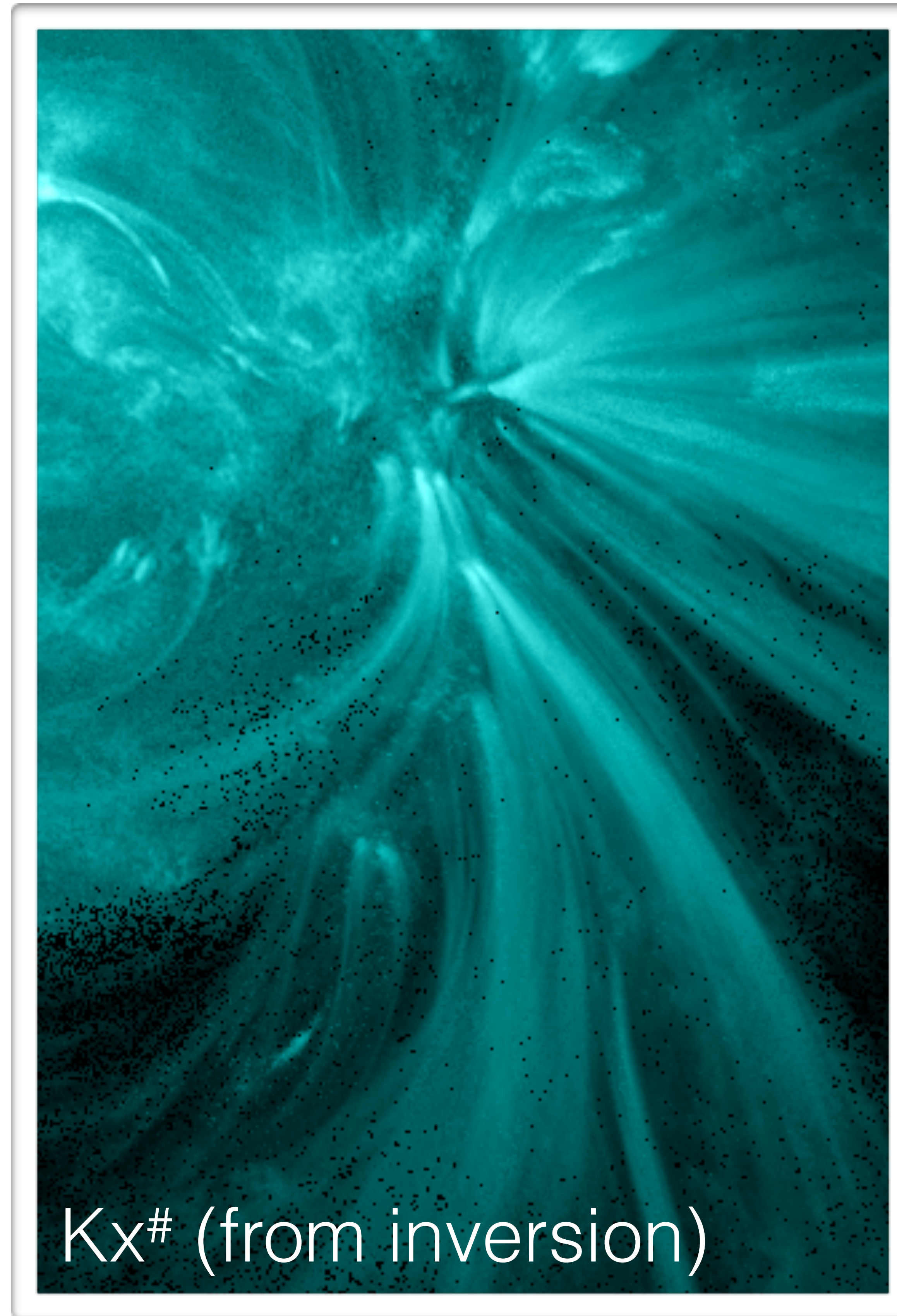


Data-Driven Modeling (Again)

Modeling of Homologous Jets

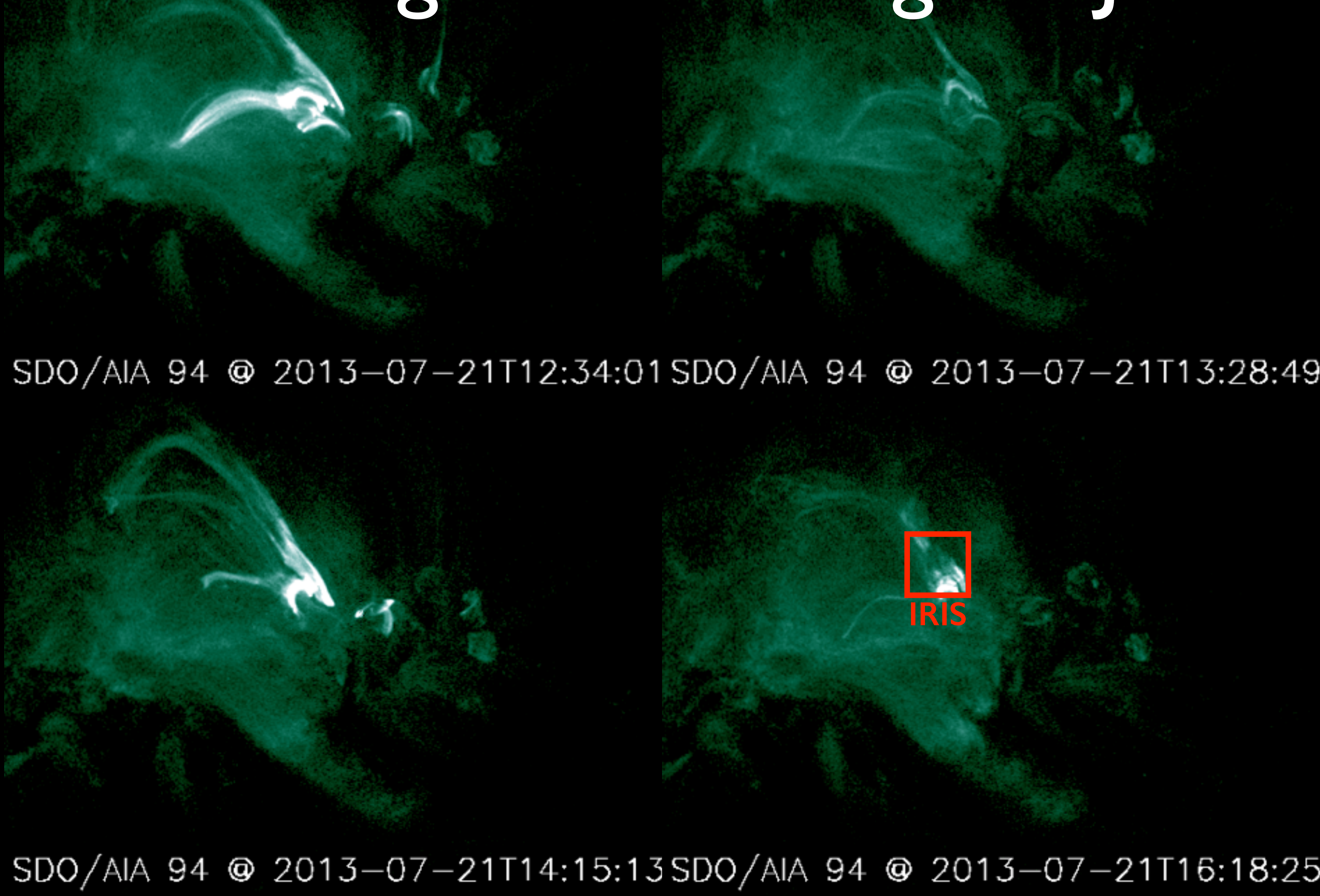

- SOT Ca II H images show jet structure similar to the jet studied by Wei Liu et al (2009).
- Lower-atmospheric contribution to Ca II H shows hints of a rotating pore and (perhaps) flux emergence.
- Indirect evidence of flux emergence from appearance of elongated darkenings followed by appearance of bright grains (e.g. Strous & Zwaan 1999, Guglielmino et al 2010).

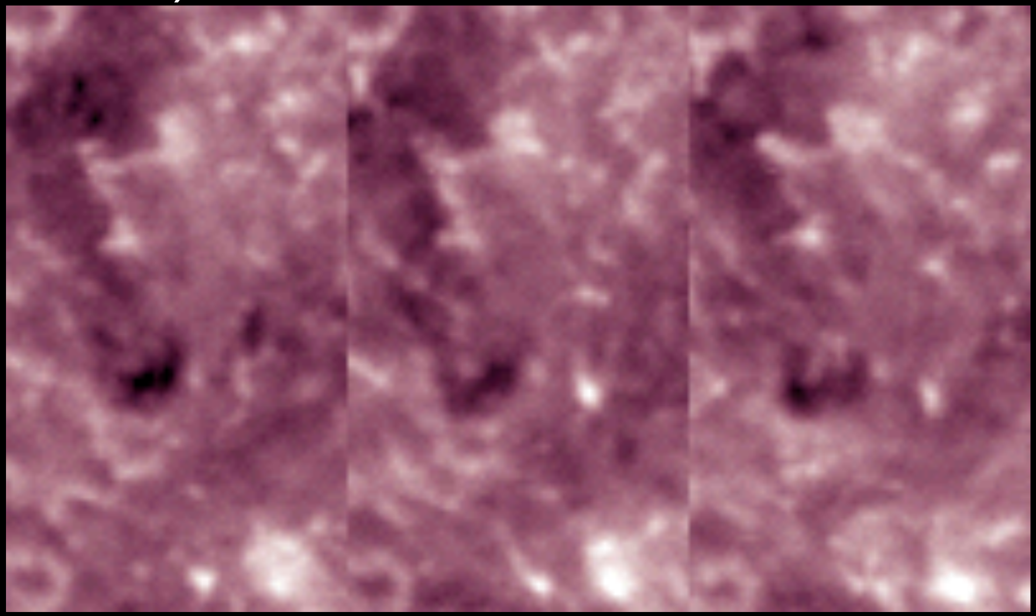

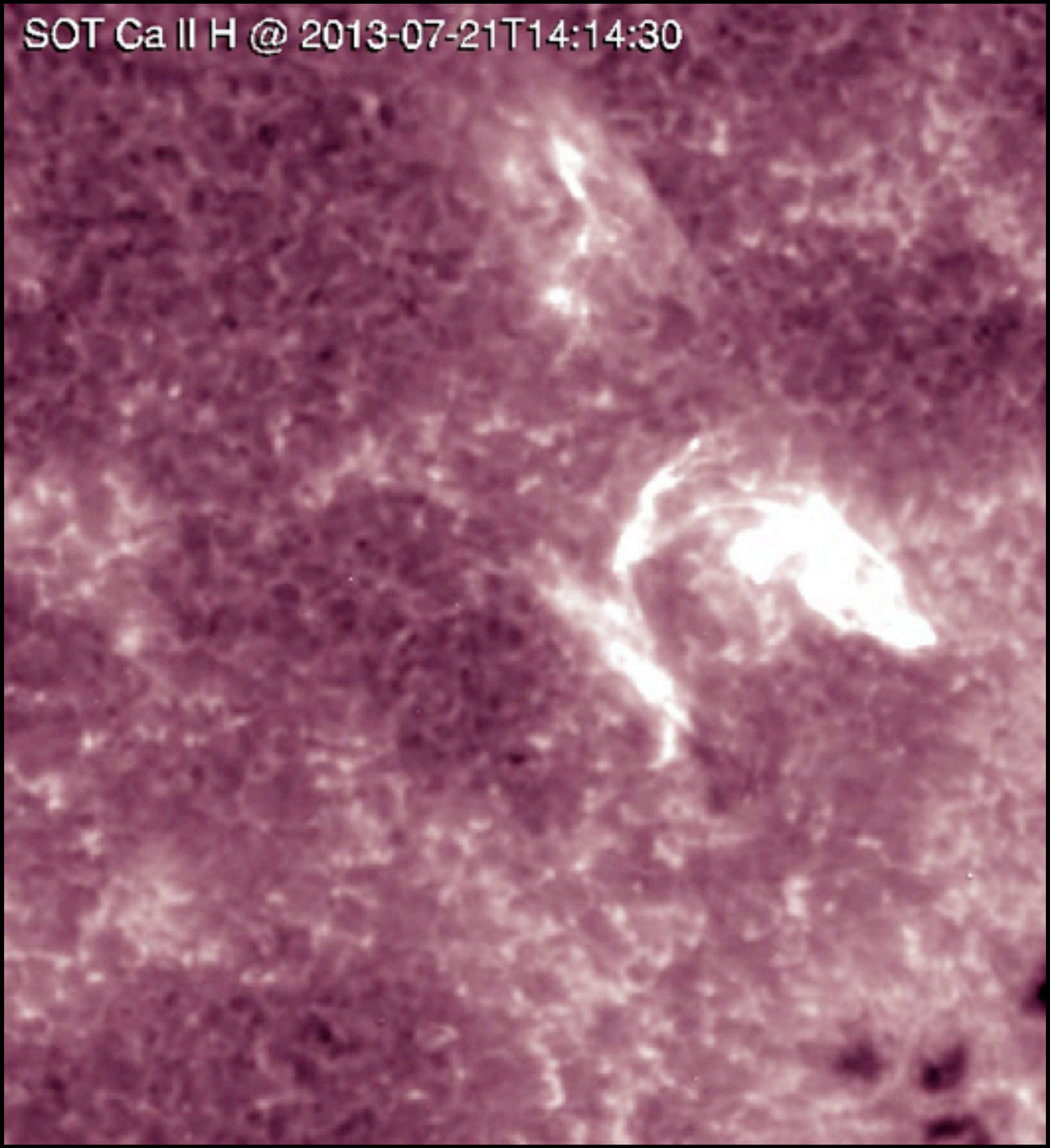

IRIS Observations

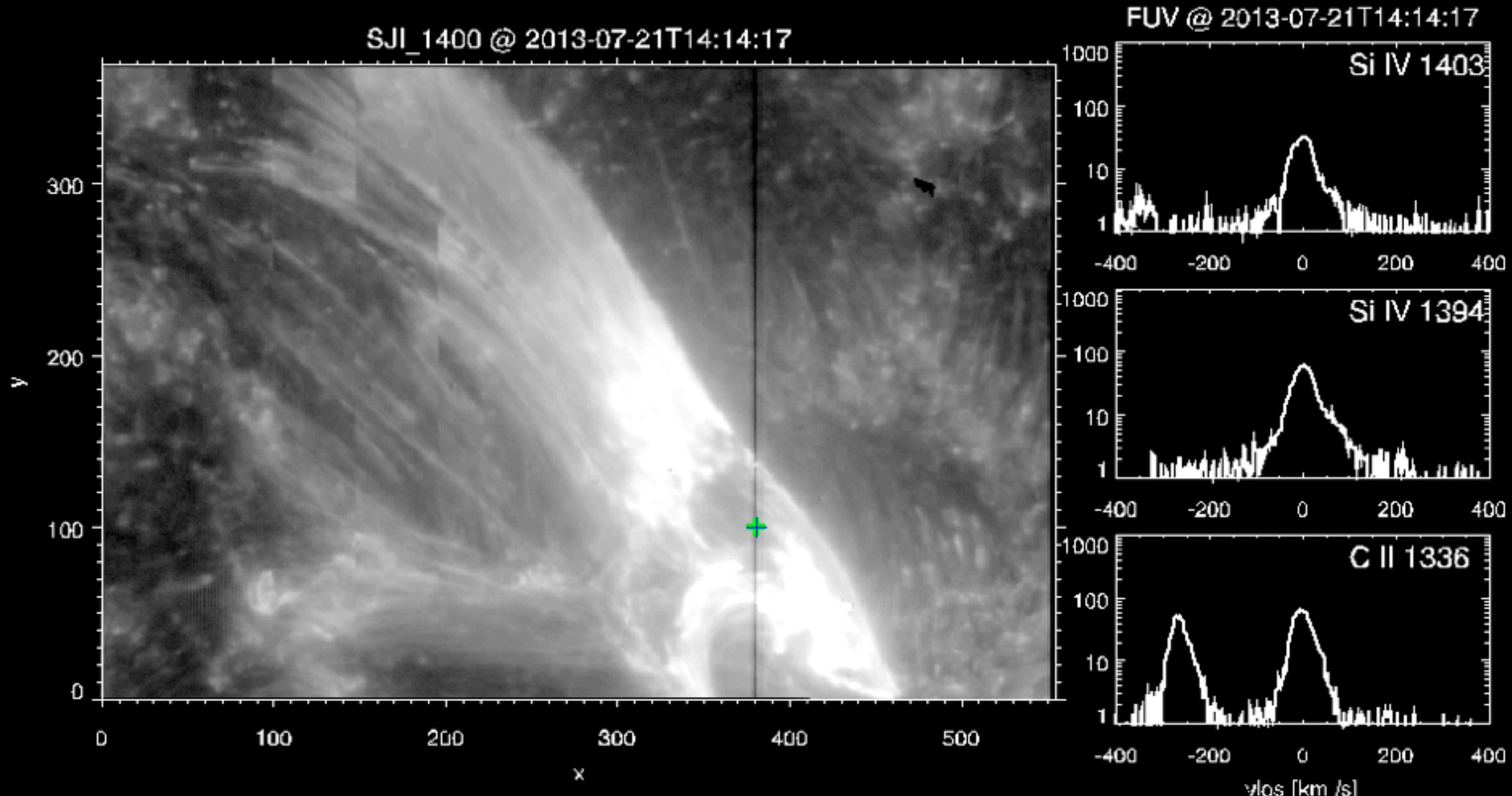

- SJI 1400, SJI 1330 and SJI 2796 @ 24s cadence, 60” x 60” FOV, 0.167” arcsec pixel size
- 20-step NUV and FUV spectral rasters with 2 arcsec steps, 2 min / raster, 38” x 60” FOV
- Focus on FUV spectra in this presentation.

Doppler shift maps using the Si IV 1394 transition region line (log T_{max} = 4.8) observed by IRIS shows helical motion in all four jets

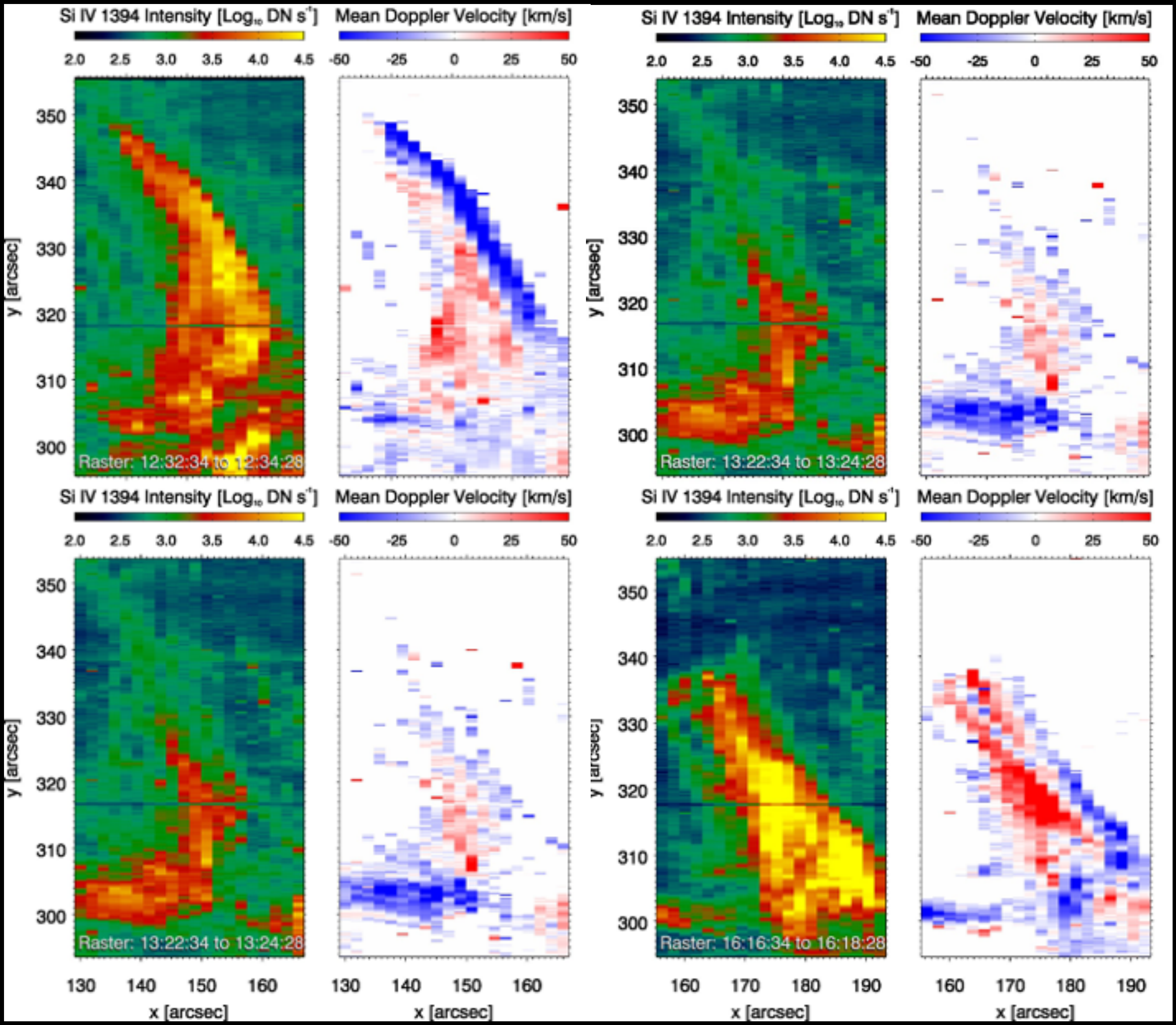

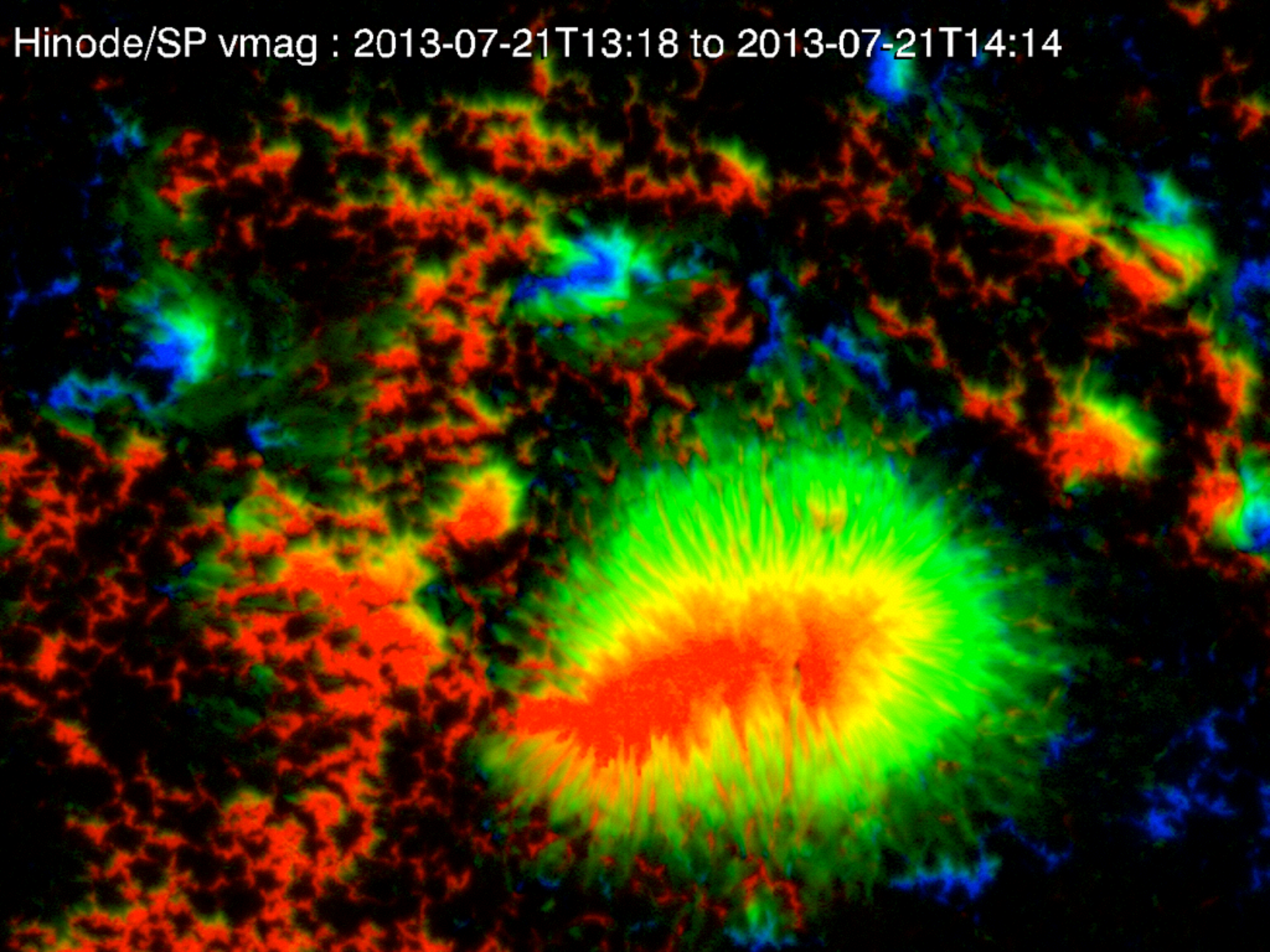
Hinode/SP vmag : 2013-07-21T13:18 to 2013-07-21T14:14

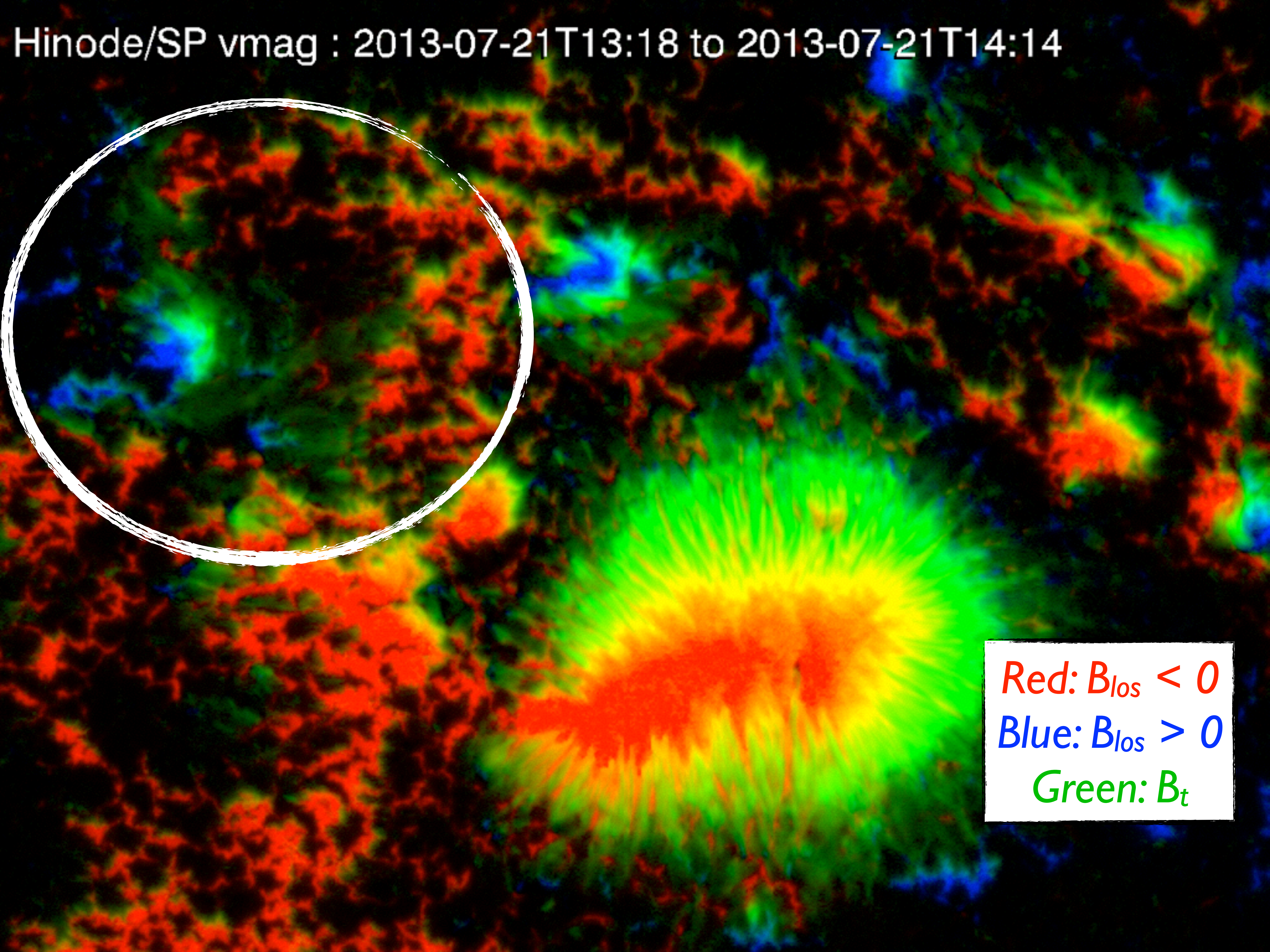
Hinode/SP vmag : 2013-07-21T13:18 to 2013-07-21T14:14
Red: $B_{los} < 0$
Blue: $B_{los} > 0$
Green: B_t

Origin of Homologous Helical Jets

- Heyvaerts & Priest (1977): Reconnection between emerging flux and ambient field for solar flares.
- Shibata et al (1992, 1994): Reconnection model for jets -> interpret post-jet loop as small flare.
- Pariat, Antiochos & DeVore (2010) showed that persistent twisting of a parasitic polarity embedded in opposite field region can lead to recurrent, homologous jets. N ~ 1 turn is needed twist up the field before a helical jet is emitted.

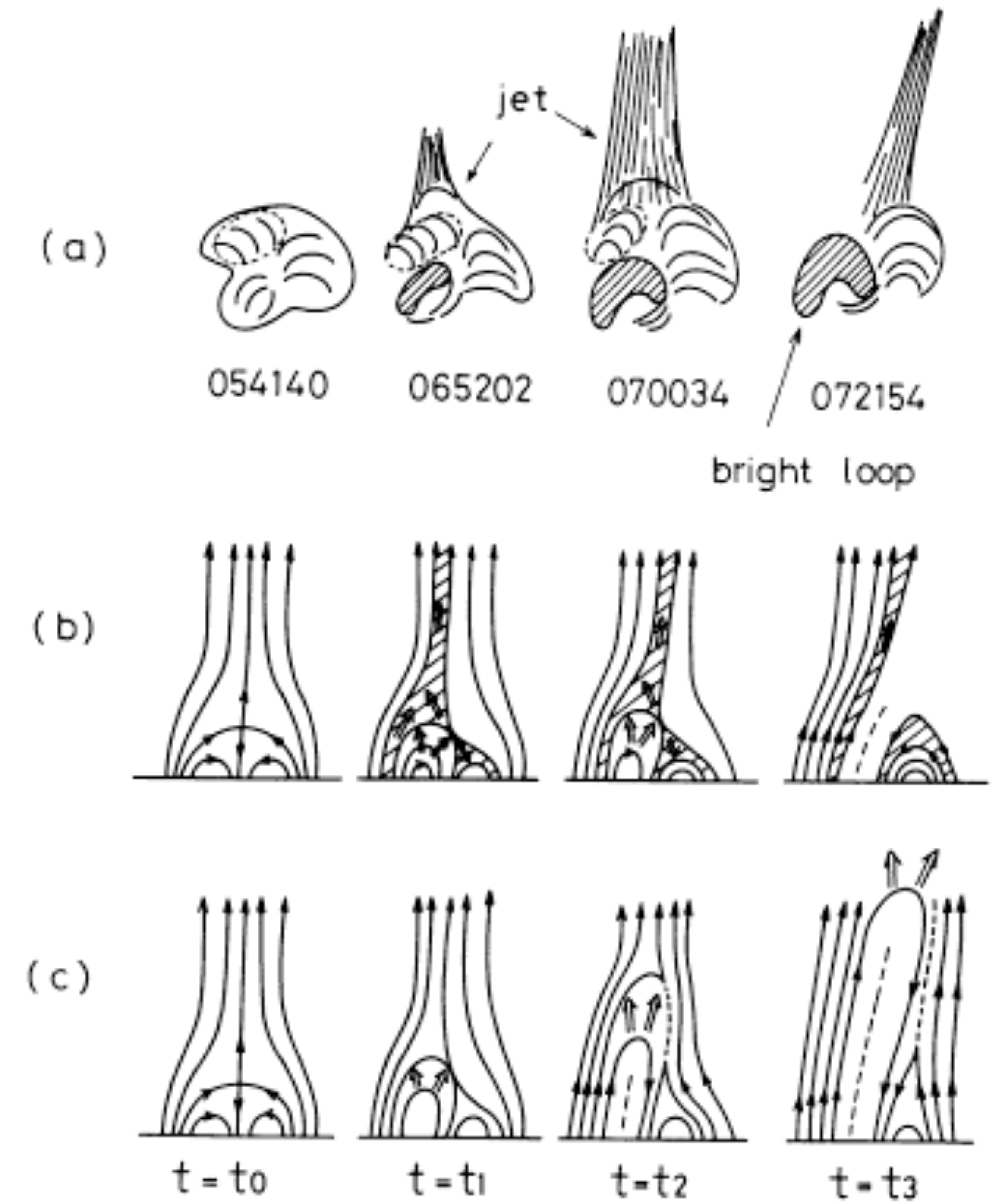

FIG. 2.—(a) Sketch of SXT images of the jet. Note that the loops just below the jet disappear after the jet ejection. (b) Hypothetical magnetic field configuration and a magnetic reconnection model explaining various observational aspects of the jet on 1992 January 11. (c) The expanding loop model for the gigantic jet on 1992 January 11. Note that this model eventually becomes similar to the reconnection model in (b) if reconnection occurs in the current sheet above the right-hand-side loop.

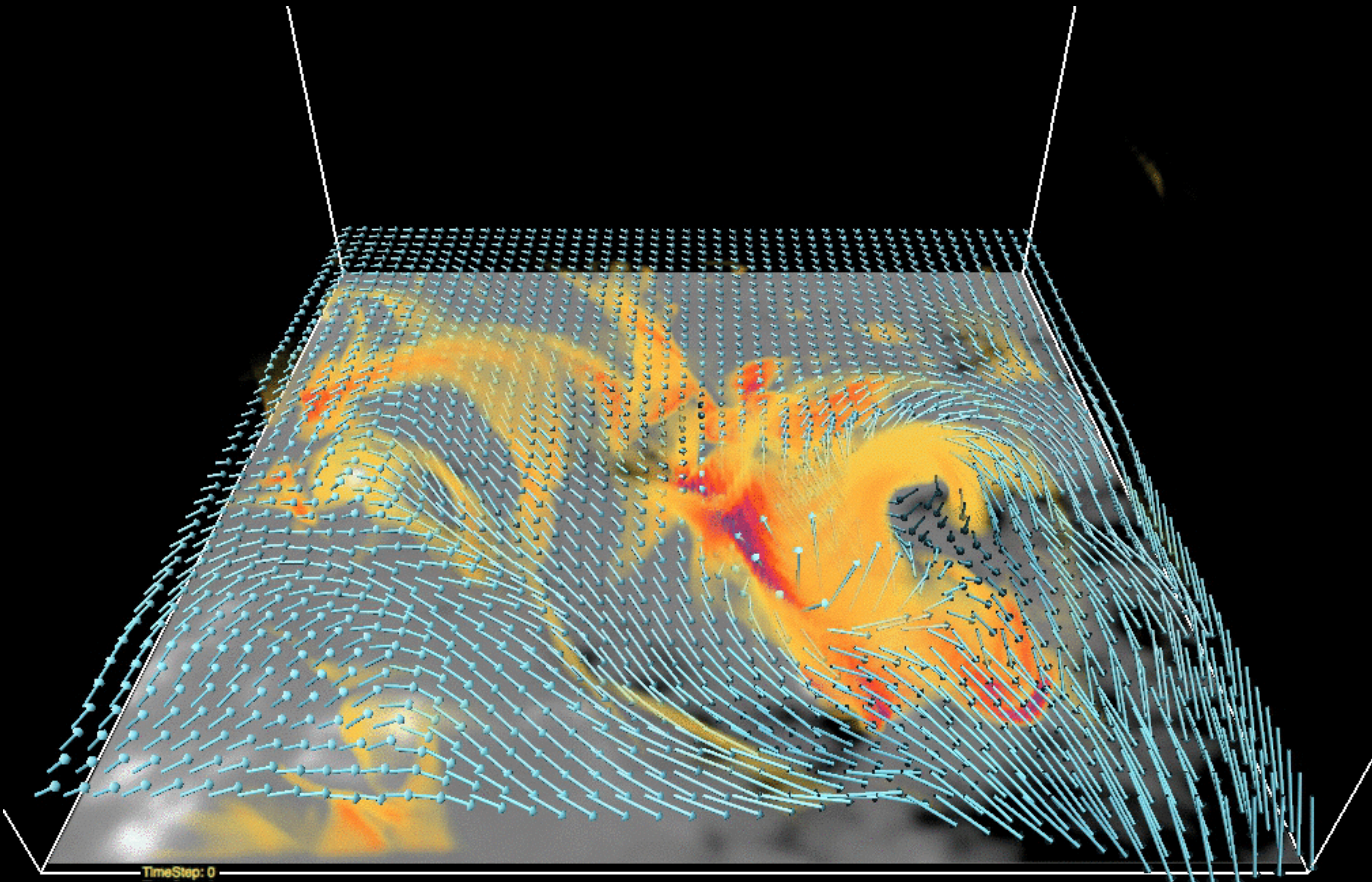

Magnetofriction model of homologous helical jets driven
by HMI vector magnetograms (Cheung et al. 2015).

In a nutshell, the data and model support the mechanism proposed by Pariat et al. (2009, 2010) for homologous jets. Helical jets emitted after about injection of one turn.

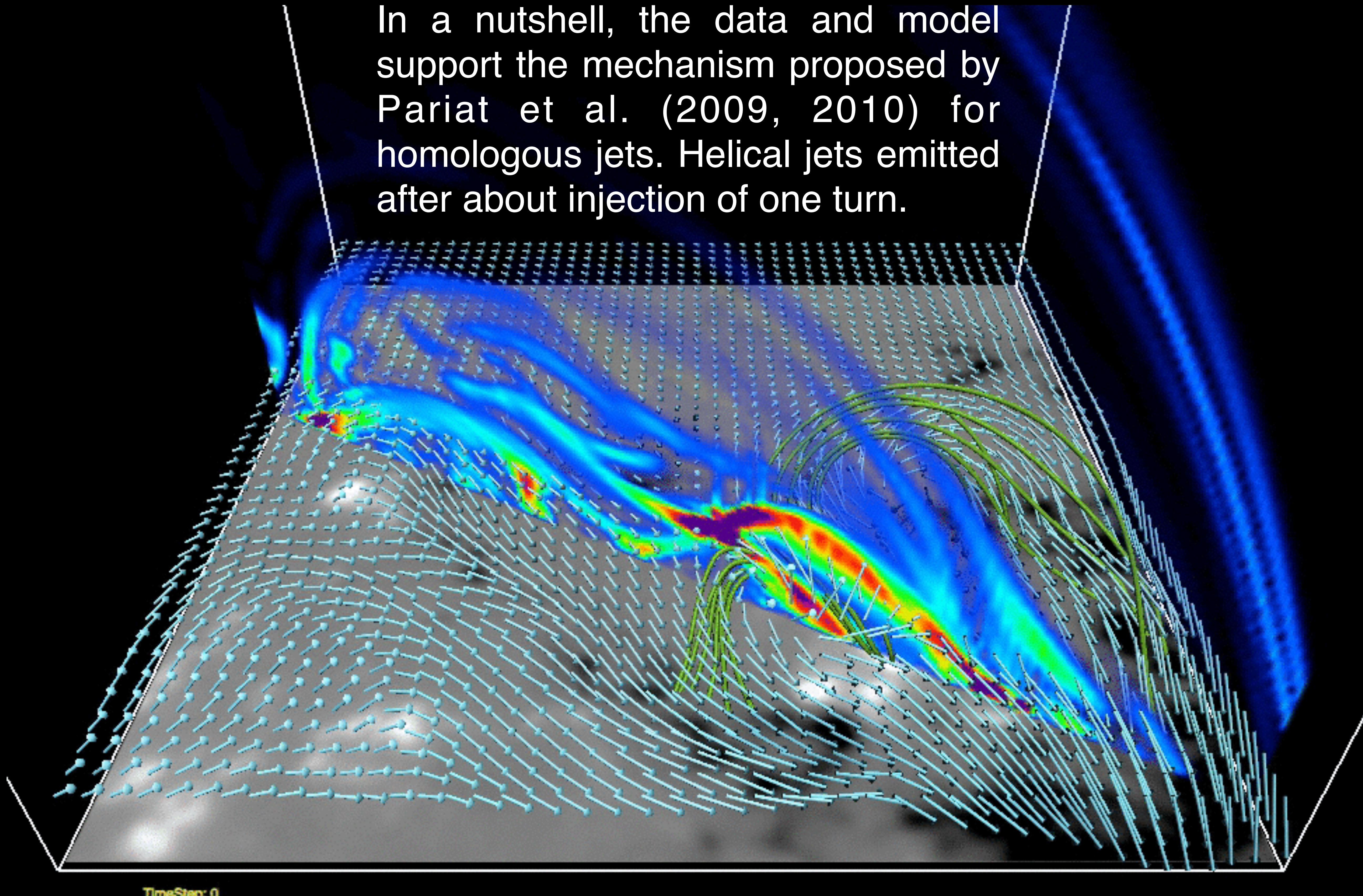

Magnetofriction model of homologous helical jets driven by HMI vector magnetograms (Cheung et al. 2015).

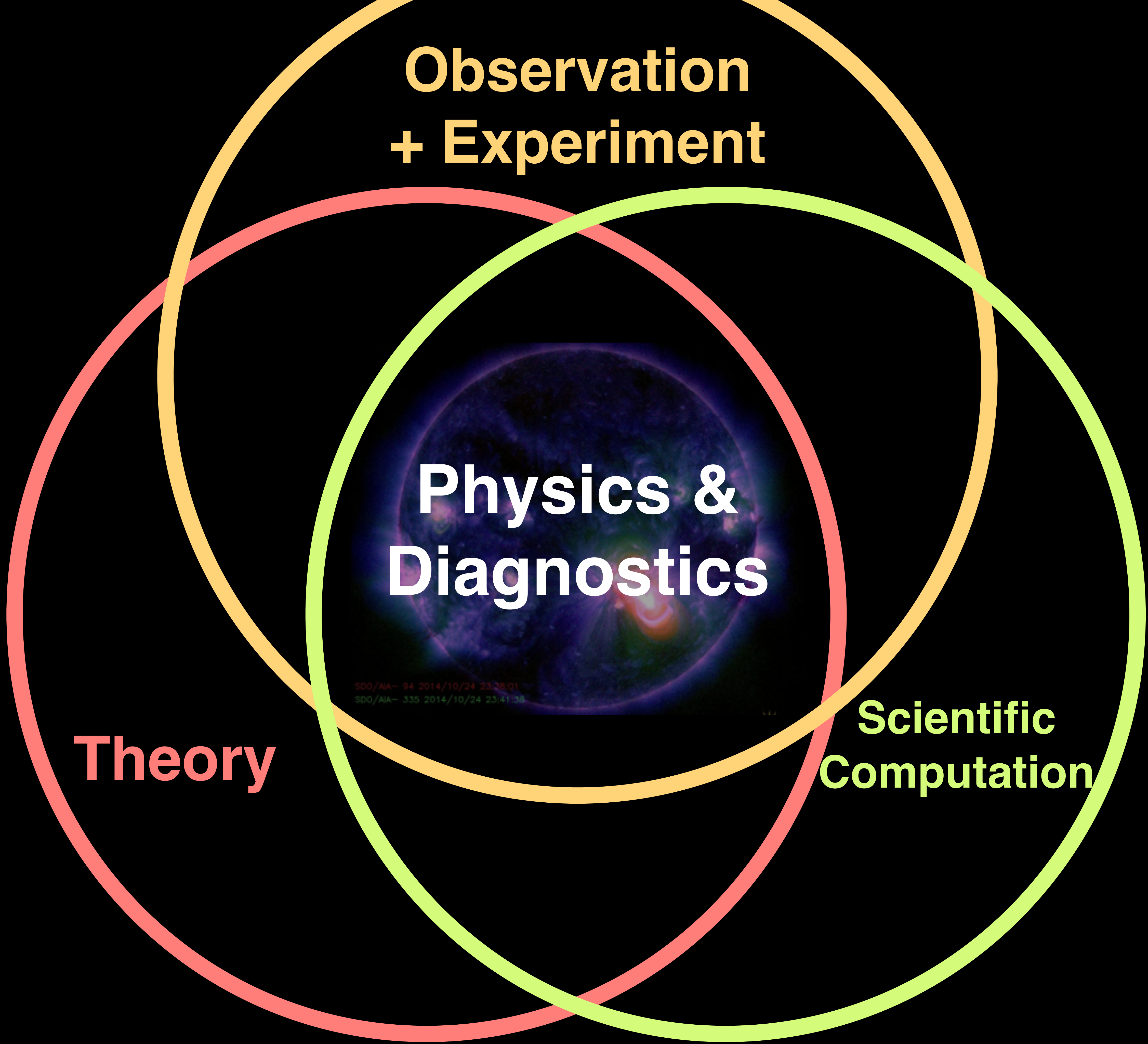
Observation
+ Experiment
Physics &
Diagnostics
Theory
Scientific
Computation

NASA Heliophysics Grand Challenges Research:
Physics and Diagnostics of the Drivers of Solar Eruptions

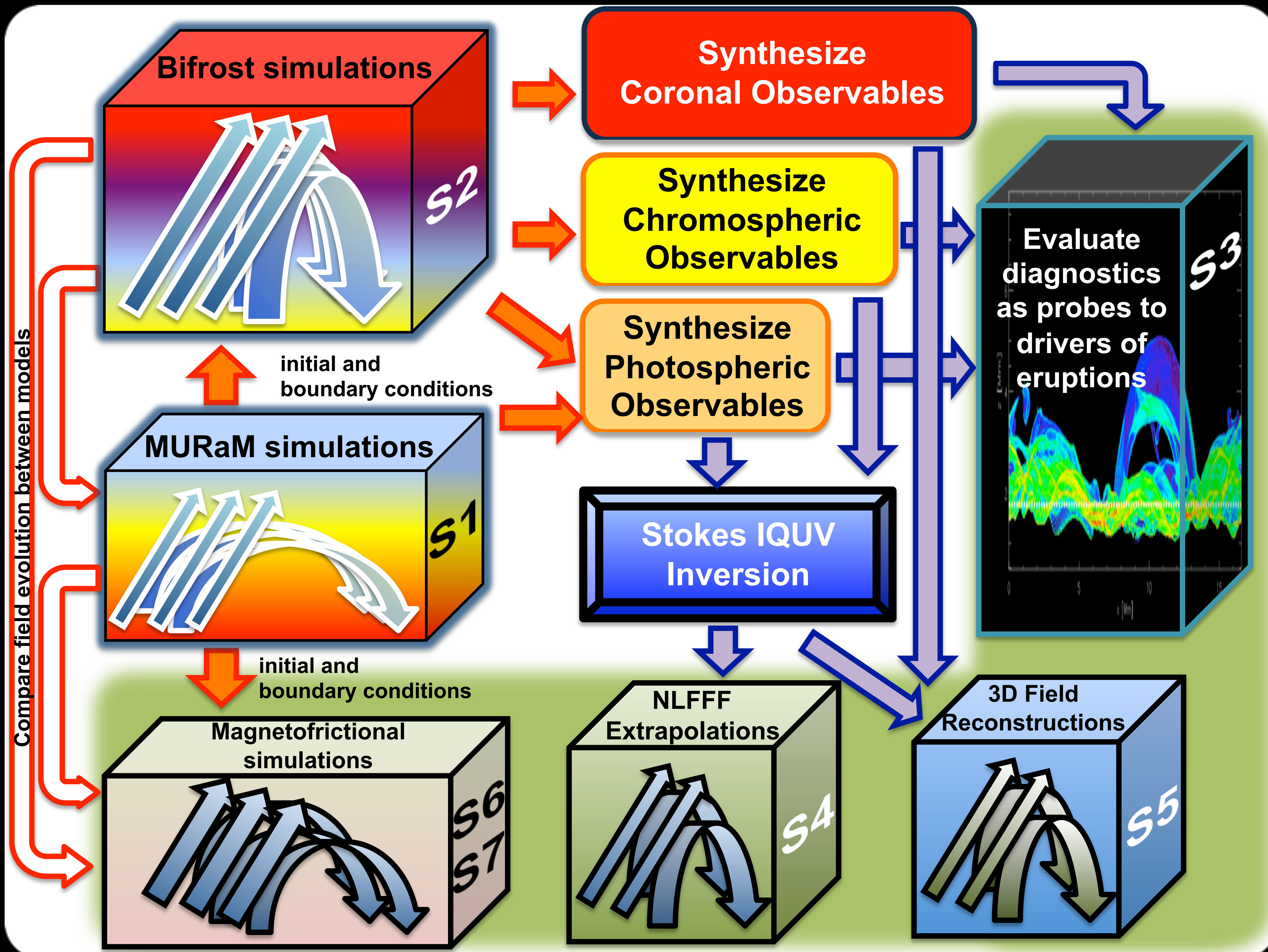

HGCR TEAM


Rempel


McIntosh


Testa


Malanushenko


Sainz Dalda


De Pontieu


Martinez-Sykora


DeRosa

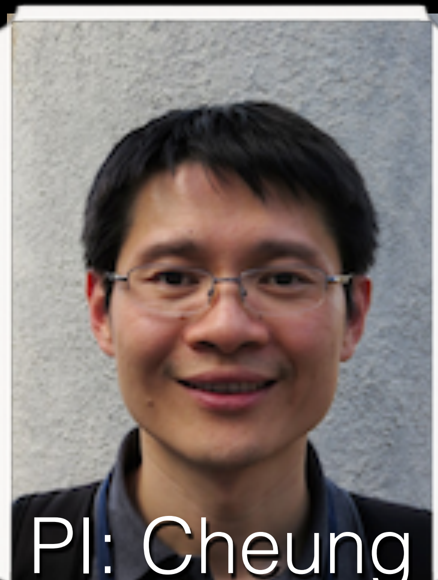
PI: Cheung


Carlsson


Hansteen


Gudiksen


Chen

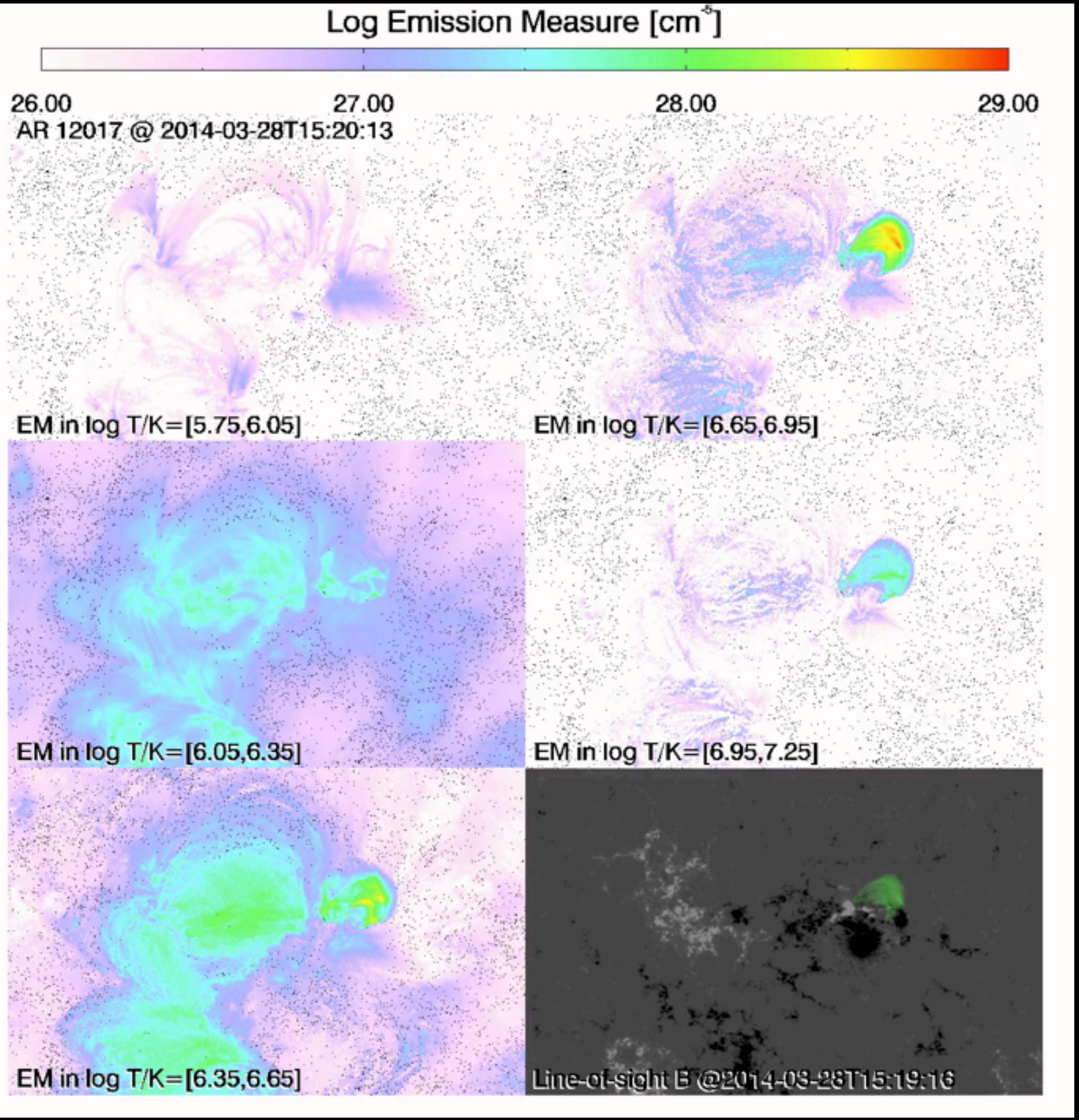

"Best Observed X-Flare"

Sunquake: Judge et al. (2014)

Filament Eruption before X-flare: Kleint et al. (2015)

IRIS Fe XXI spectra: Young et al. (2015)

Chromospheric Evaporation: Li et al. (2015)

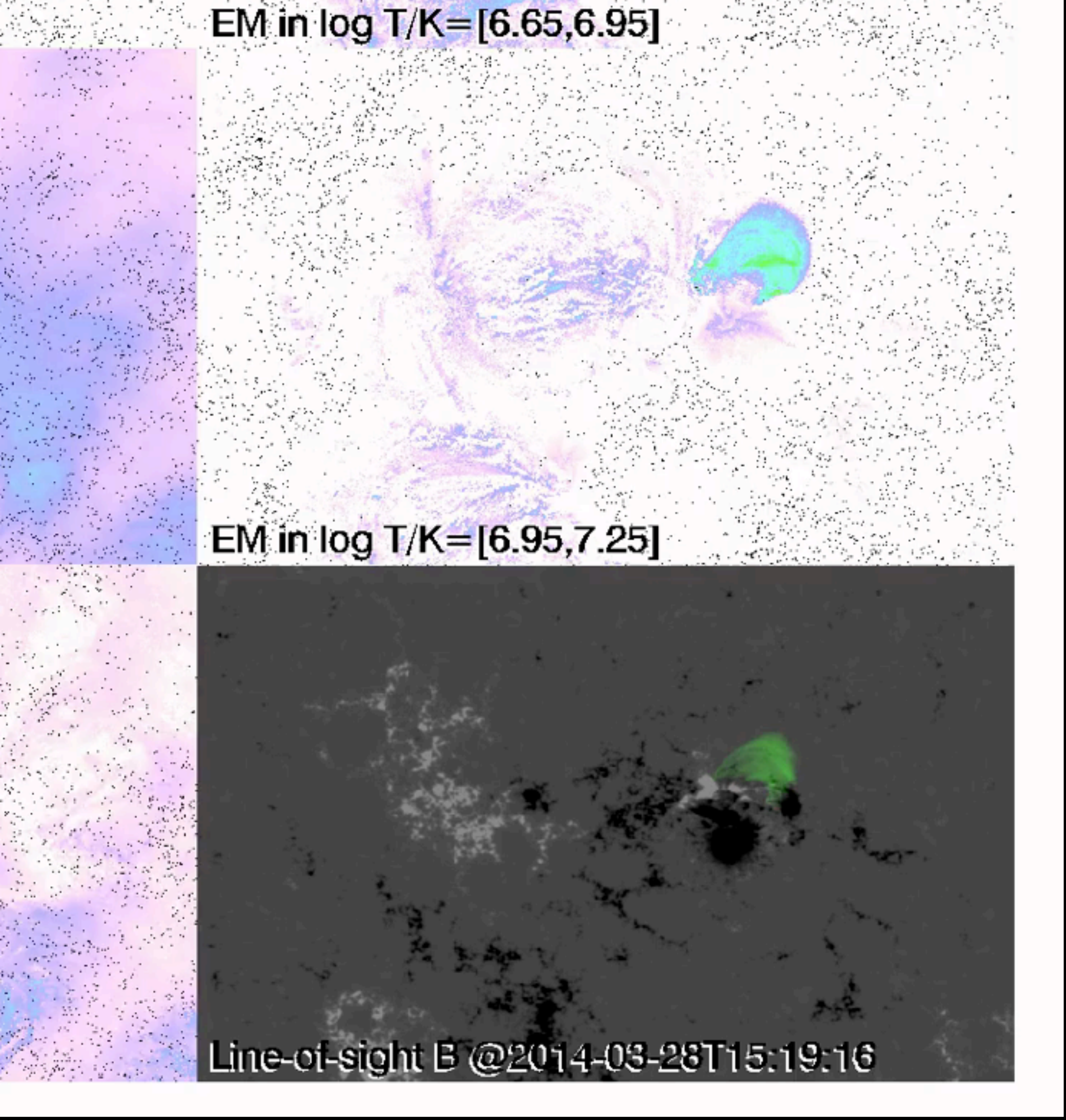

“Best Observed X-Flare”

Sunquake: Judge et al. (2014)

Filament Eruption before X-flare: Kleint et al. (2015)

IRIS Fe XXI spectra: Young et al. (2015)

Chromospheric Evaporation: Li et al. (2015)

Target AR: Level 0 Model

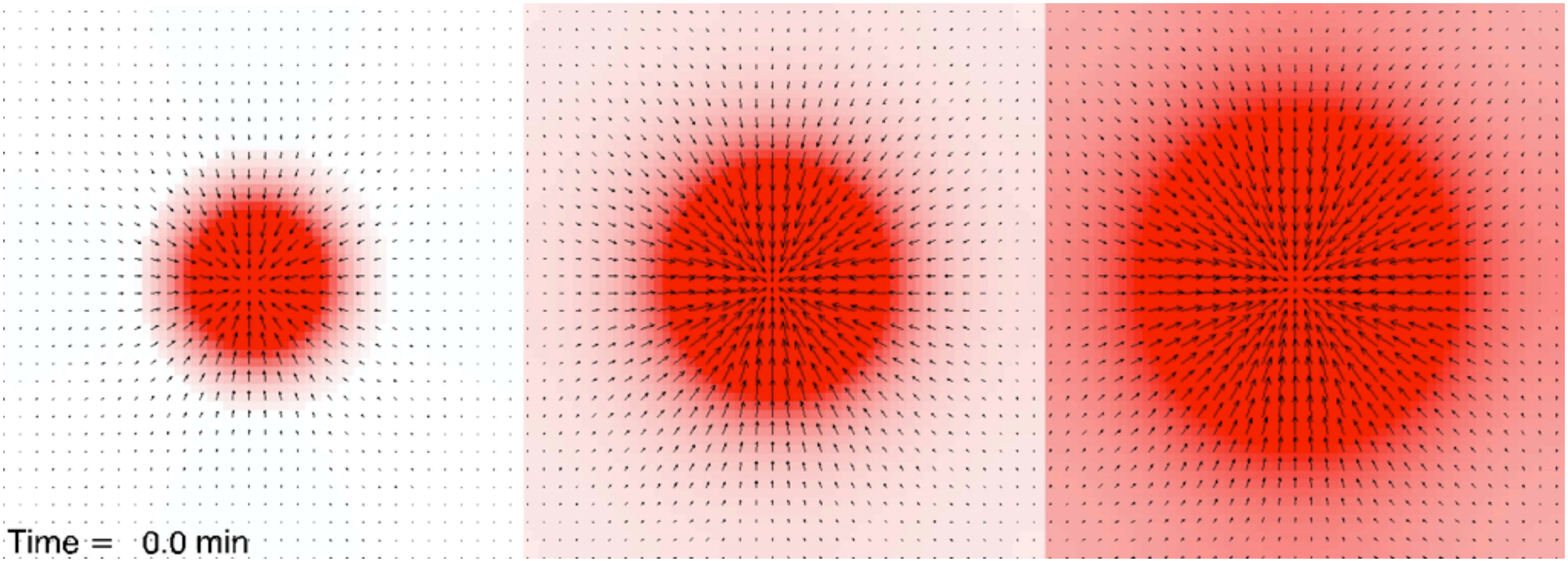

Magnetofrictional model of a twisted flux tube emerging next to a single preexisting sunspot. Red and blue show opposite polarity. Magnetogram at 3 different heights (left most is z=0).

Target AR: Level 1 Model

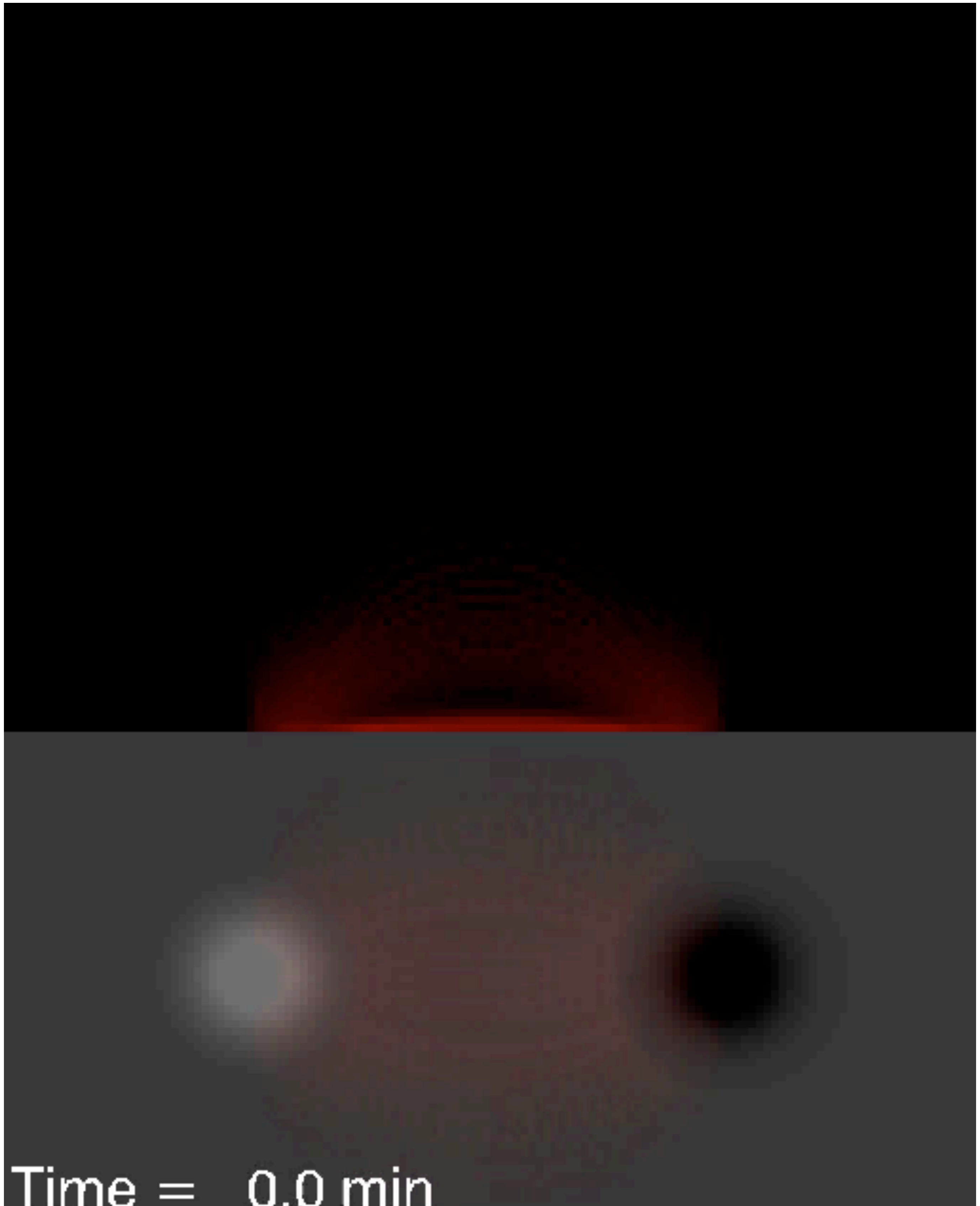

Magnetofrictional model of a twisted flux tube emerging next to the 'preceding' spot of a bipolar active region. Magnetogram at z=0 shown in greyscale. Field lines illuminated by field-line-averaged j^2.

Target AR: Level 2 Model

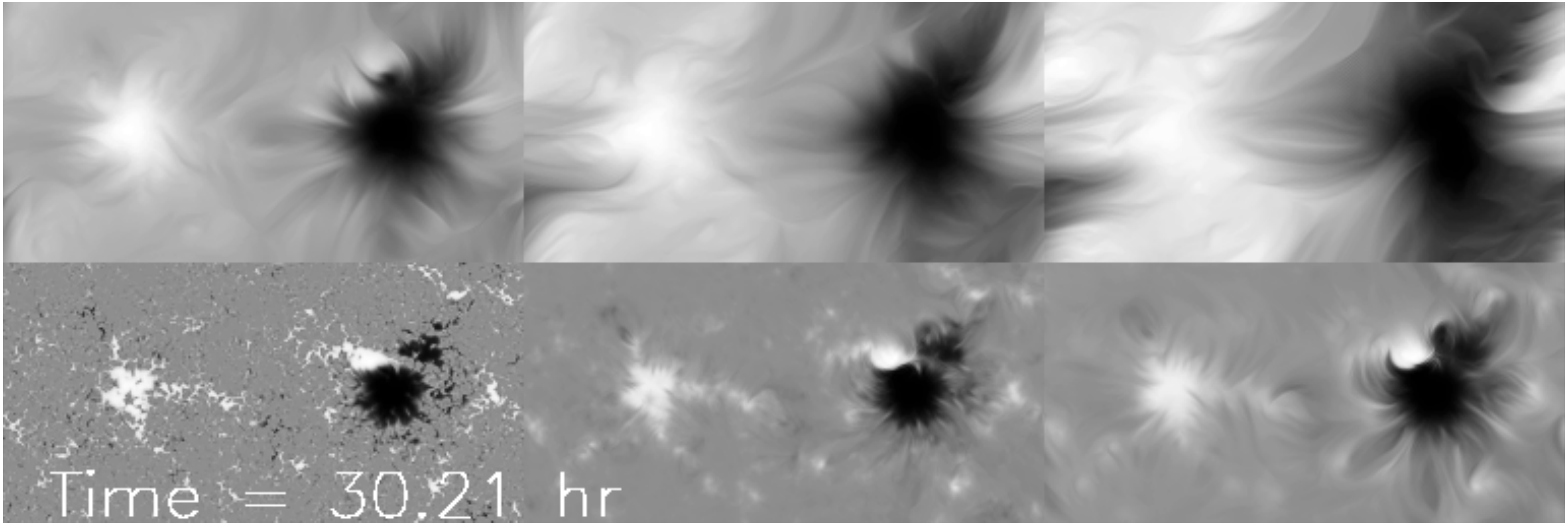

<u>MURaM-driven Magnetofrictional model</u>

Initial condition is a pair of developed spots. Twisted tube emerged north of preceding spot. The MURaM calculation stops at photosphere. Use electric field at z=0 to drive the magnetofriction (MF) model. The MF model indicates there will likely be interesting dynamics.

<u>Level 3: The MURaM run will be repeated to include the corona.</u>

<u>Level 4: Then we will use Bifrost to get realistic thermodynamic structures to compute diagnostics.</u>

Summary

- Magnetic Field Diagnostics: We really learned a lot from photospheric measurements. The prime target now should be the chromosphere (and maybe corona), which is arguably the best place for magnetic imaging of reconnection in the solar and astrophysical domains.

- Thermal Diagnostics: SDO, IRIS and Hinode provide a wealth of information that covers the full range of temperatures in the solar atmosphere. AIA DEMs can be routinely computed with good(fair?) match with XRT observations.

- Data-Driven models tighten the link between theory and observations. We have many idealized models but it's time to test them against real cases. It's also time to back up qualitative interpretations of observations with modeling. I hope more students and postdocs think about the problems that need to be tackled to advance in this direction.

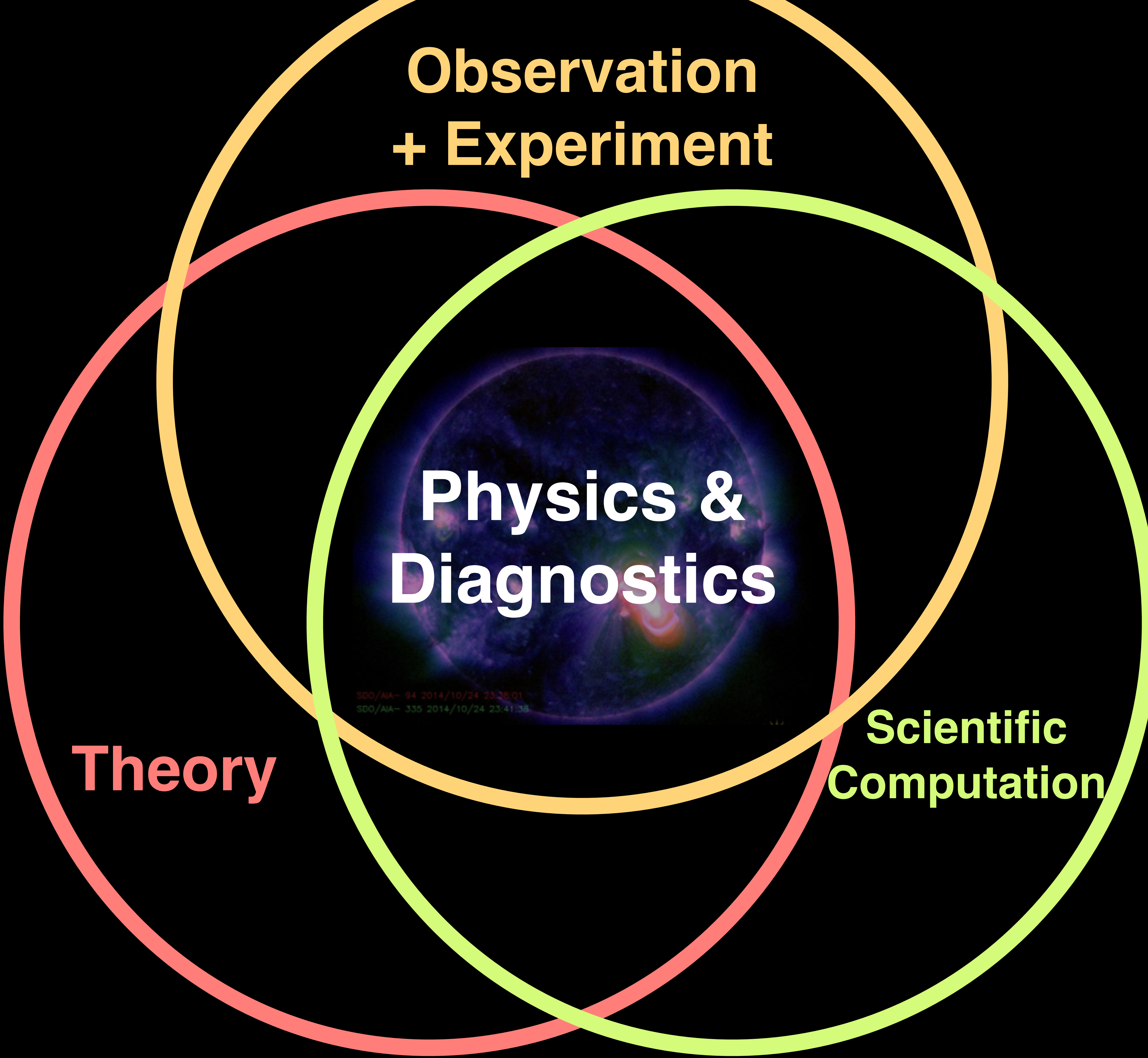
Observation
+ Experiment
Physics &
Diagnostics
Theory
Scientific
Computation

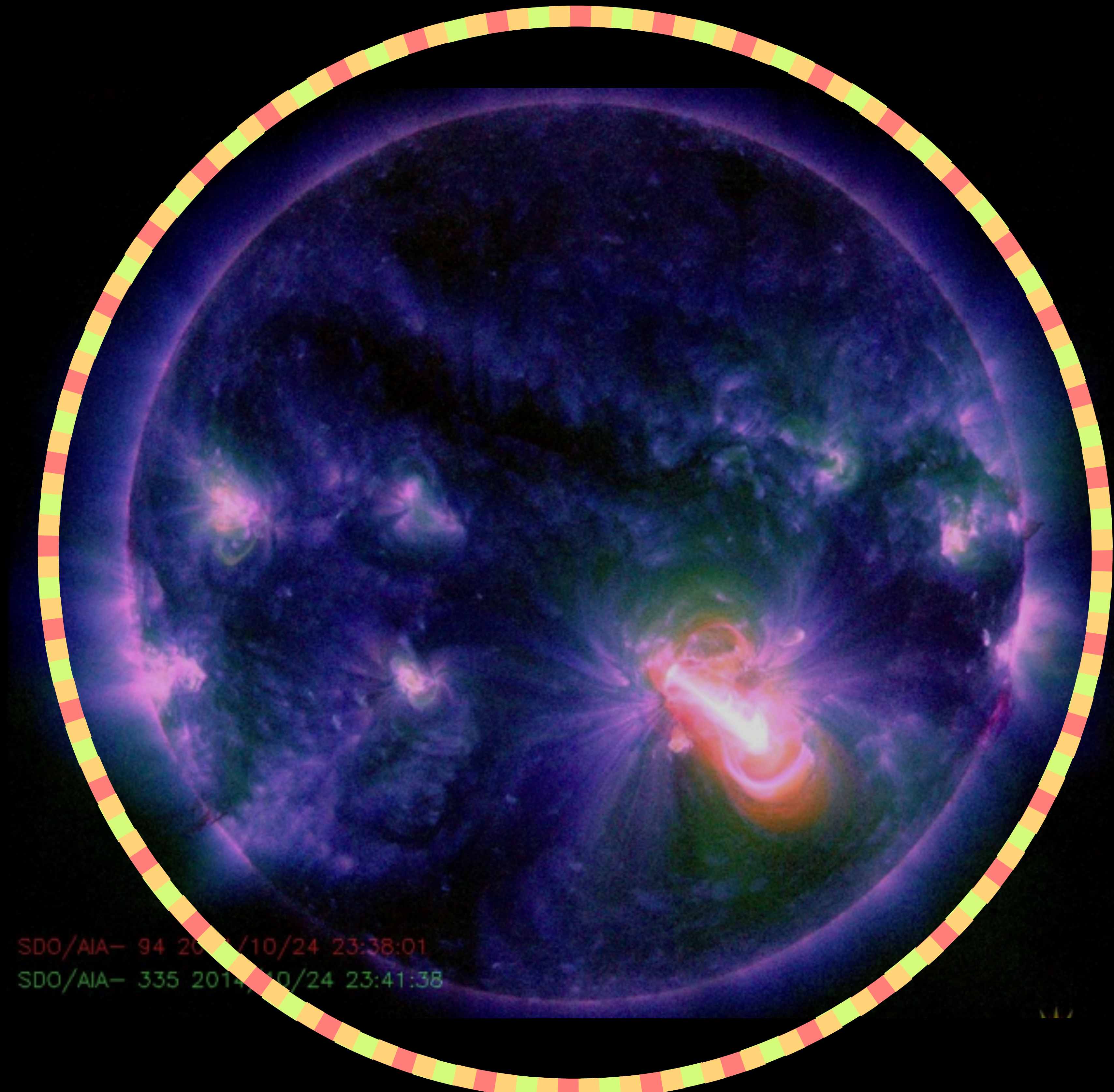

よろしくお願いします